UNIVERSITY OF SOUTHAMPTON

FACULTY OF ENGINEERING, SCIENCE AND MATHEMATICS

School of Physics and Astronomy

A Numerical Study in Spectra and Variability of X-ray Binaries and AGN

Katrine Sharp Rogers

Thesis for the degree of Doctor of Philosophy

April 2008

UNIVERSITY OF SOUTHAMPTON

ABSTRACT

FACULTY OF ENGINEERING, SCIENCE AND MATHEMATICS

SCHOOL OF PHYSICS AND ASTRONOMY

Doctor of Philosophy

A NUMERICAL STUDY IN SPECTRA AND VARIABILITY OF X-RAY BINARIES AND AGN

Katrine Sharp Rogers

A detailed overview of the HEART code is given. This code models radiative transfer of any photon distribution in a plasma of any geometry containing any electron distribution, where the photon and electron distributions evolve simultaneously. All relevant physical processes are included, and applications include modelling the inner regions of X-ray binaries and AGN.

An investigation into the capabilities and accuracy of HEART forms the major part of this thesis. HEART is tested for a simple case of a spherical electron plasma where only Compton scattering is modelled and the evolution of the electron distribution is disabled. Tests are done by comparing the output spectra from HEART to the XSPEC model *compTT*, as well as by using HEART to fit observational data from Cyg X-1. Several additions to the code are also included, some of which are used in the testing process.

A limited range of parameters is found to be modelled accurately, and an investigation is included into extending the valid parameter range by including an anisotropic treatment of Compton scattering. HEART is, however, also found to be computer intensive, making it unsuitable for routine spectral fitting. The focus is therefore moved to the capability of HEART for modelling dynamic situations, which is a potential strength of HEART, and may determine whether improvements to the spectral fitting of HEART are worthwhile.

Although the framework of HEART allows for dynamic modelling, several modifications are required to implement it. These modifications are implemented and tested by modelling two distinct dynamic situations: a state transition in an X-ray binary and an X-ray burst on the surface of a neutron star. HEART is found to be capable of varying the steady-state parameters from one steady-state to another, but it is not capable of modelling electron heating, reprocessing and energy balance, and it is restricted to modelling very short physical timescales.

The limitations discussed above, combined with further technical limitations discussed in this thesis, lead to the conclusion that HEART is not suitable for further use without complete restructuring.

Contents

List of Figures

List of Tables

Acknowledgements

I would like to thank my supervisor, Christian Kaiser, for his guidance throughout, and for providing encouragement and support when nothing seemed to work. My advisor, Tom Maccarone, has also supported me throughout with many useful discussions and much guidance, particularly in the realm of observational astronomy.

I would also like to thank my examiners for the interesting discussion we had during my viva, though I did not particularly enjoy it at the time(!), and for useful advice for the future.

I am also very grateful to Omar Jamil for keeping me company on my journey through the HEART code, and my office mates for keeping me entertained. No-one can ever replace Retha Pretorius' unique way of expressing herself.

I would like to thank Jon Miller and Tiziana Di Salvo for providing me with the observational data used in this thesis.

Finally, I would like to thank my family for their constant support. Specifically, my husband, Edward Rogers, has always listened patiently when a listener was needed and come to my aid whenever my computer developed a mischievous will of its own. My parents, Kari-Anne Jensen Sharp and William Sharp, always listen, encourage me and show an interest in my work — my mother even proof-read this thesis! Annette Sharp, my sister, is always supportive and understanding, as we go through the same stages in life together. My father-in-law, Chris Rogers, has completed a PhD himself and has seen several from the other side since. He has therefore been able to provide guidance, while my mother-in-law, Cathie Rogers, provides equally important non-technical support.

Chapter 1

Introduction

1.1 X-ray Binaries

X-ray binaries are binary systems where one of the objects is a compact object (a neutron star or black hole candidate) and the other is a donor star. These are called the primary and the secondary respectively. As the name suggests, X-ray binaries emit radiation in the X-rays and their X-ray spectra are much studied, but they also emit broadband radiation, including UV, optical and sometimes extending down to radio emission.

The geometry of X-ray binaries and the mechanisms behind their emission are not fully understood. Understanding the physics of X-ray binaries is important as black hole X-ray binaries (BHXBs)[1] provide a laboratory for probing general relativity in strong gravitational fields. Understanding the physics of BHXBs may also improve our understanding of supermassive black holes and active galactic nuclei (AGN). The supermassive black holes in AGN are expected to behave similarly to the galactic stellar mass black holes in X-ray binaries (see section 1.4). X-ray binaries also play a part in both stellar evolution and the evolution of binary systems.

X-ray binaries are classified into two types: low mass and high mass X-ray

[1]BHXBs is used here to refer to X-ray binaries where the compact object is a black hole candidate. This classification is usually made when the mass of the compact object is greater than $3M_{\odot}$ or the behaviour of the binary is similar to that of other BHXBs.

binaries (LMXBs and HMXBs respectively). In LMXBs, for example Aql X-1, the secondary is less massive ($\lesssim 1M_{\odot}$) and provides matter for the accretion on to the compact object by overflowing its Roche lobe. HMXBs, for example Cygnus X-1 (Cyg X-1), include a more massive secondary, usually a massive O/B star ($\gtrsim 10M_{\odot}$), and accretion occurs through the stellar wind of the secondary. The properties of the region near the compact object is similar in both cases, however. An accretion disc forms around the compact object in both LMXBs and HMXBs, which heats due to frictional dissipation of gravitational energy, and releases soft X-rays. Some of these soft X-rays are upscattered to hard X-rays and gamma rays, forming typical spectra which are discussed below.

BHXBs are observed in two main states which are classified according to their X-ray spectra: the low hard state (LHS) and the high soft state (HSS). Typical LHS and HSS X-ray spectra are shown in figure 1.1. Several other states are defined in the literature, sometimes with contradictory definitions, but three other states are generally accepted: the quiescent state, the very high state (VHS) and the intermediate state (IS). Definitions vary somewhat, and those given here are based on the review by McClintock & Remillard (2004).

The LHS X-ray spectrum is dominated by a power-law component with spectral index $1.5 < \Gamma < 2.1$ and a high energy cut-off at $\gtrsim 100 - 200$ keV. Sometimes a weak, soft blackbody component is also observed which is probably blackbody emission from the accretion disc (at $\lesssim 0.1$ keV). Several mechanisms for producing the dominant power-law component have been suggested, but inverse Compton scattering of the disc photons by thermal electrons, referred to here as Comptonisation, is most widely used. This explains the high energy cut-off at $\sim 3kT_e$ where k is the Boltzmann constant and T_e is the electron temperature. An additional reflection component has also been observed in the LHS, especially in systems viewed close to face on (DiSalvo et al., 2001). This component probably consists of Comptonised photons which have been reflected and reprocessed in the accretion disc, and is discussed further in section 3.1. Another distinguishing feature of the LHS is the

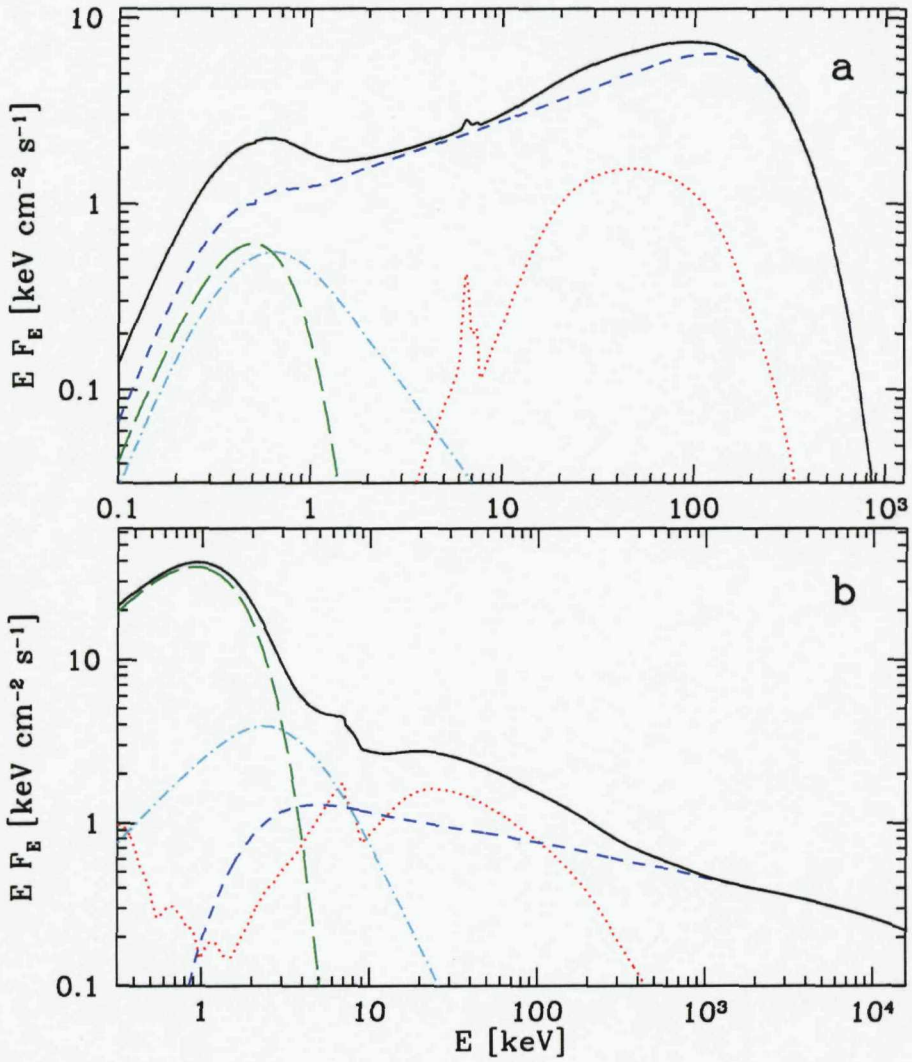

Figure 1.1: Typical spectra of Cyg X-1 in the low hard state (a) and the high soft state (b) (taken from Zdziarski & Gierliński 2004). The solid black line shows the overall spectrum, the green dashed line is the blackbody spectrum from the disc and the blue shorter dashed line is the Comptonised radiation by thermal electrons in (a) and nonthermal electrons of a hybrid distribution in (b). Two additional components are included here. The red dotted line is reflection from the disc, which is discussed further in section 3.1, as well as the Fe Kα fluorescence. The cyan dot-dashed line shows an additional soft excess, probably due to Compton scattering in a region physically distinct to the thermal plasma in (a) and Compton scattered photons by the thermal part of a hybrid electron distribution in (b).

presence of persistent radio jets (Fender, 2001; Fender et al., 2004).

The X-ray spectrum of the HSS is dominated by a soft blackbody at $\sim$ 0.7-1.5 keV, probably from an accretion disc. This is well described by the thin disc model by Shakura & Sunyaev (1973). We also observe a high energy power-law tail with spectral index $\Gamma \gtrsim 2$ and no observed high-energy cut-off, which is probably caused by Comptonised disc photons scattered by a hybrid electron distribution. A reflection component is again observed, and any radio jets are quenched when the HSS is entered (Fender et al., 1999, 2004).

The quiescent state is very similar to the LHS, but at a much lower luminosity. This is the state in which most BHXBs spend most of their time (McClintock & Remillard, 2004).

The VHS is defined similarly to the HSS, but with a very steep power-law $\Gamma > 2.4$ and quasi-periodic oscillations (QPOs) present in the X-rays (0.1-30 Hz). Alternatively, if there are no QPOs, the spectrum is still classified as being in the VHS if the power-law contributes more than 50% of the total flux.

For the purposes of discussing jets in the VHS, following the discussion of Fender et al. (2004), it is useful to further classify the VHS into the 'hard' VHS and the 'soft' VHS. If the VHS occurs between a transition from the LHS to the HSS, then the transition is from the LHS to the 'hard' VHS, to the 'soft' VHS, and finally to the HSS. In the 'hard' VHS the persistent jet of the LHS continues to exist, but as the 'hard' VHS becomes the 'soft' VHS, possibly at the peak luminosity, a relativistic jet is emitted, creating a shock region as it collides with the persistent and slower jet of the LHS. An optically thin radio flare is observed, and if this transition is made multiple times without transition to the quiescent state, such as in GRS 1915+105, multiple radio flares are observed. When the source reaches the 'soft' VHS followed by the HSS the jet is quenched as noted above.

The IS is associated with transitions between the quiescent state, LHS, HSS and VHS and the X-ray spectrum consists of combinations of the characteristic components described above. For example a strong soft blackbody component may

be combined with a significant hard component. Transitions are observed at a range of different luminosities which has given rise to different classifications within the intermediate states. Zdziarski & Gierliński (2004) define the IS spectrum as a high energy tail originating close to the peak of the blackbody component. The IS and VHS are treated as one with respect to their jet properties in Fender et al. (2004).

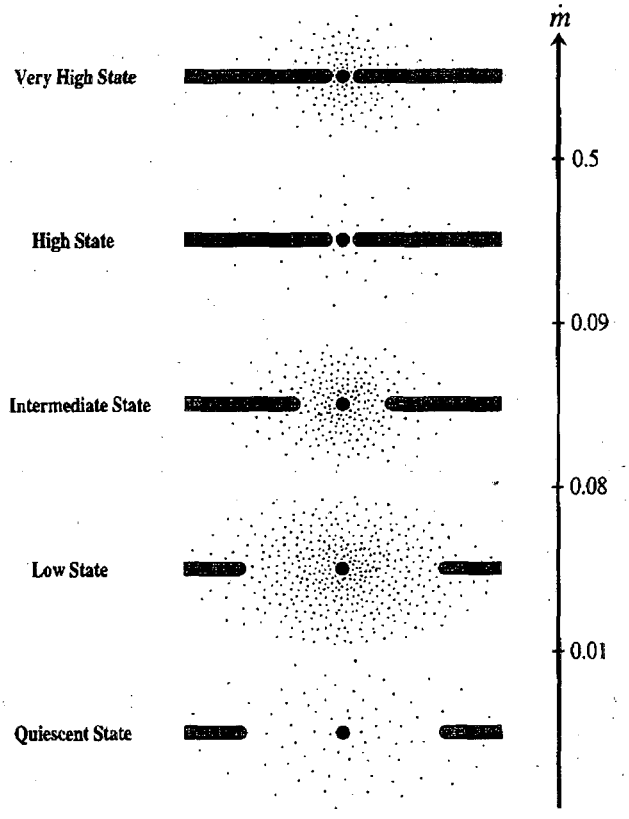

Figure 1.2: Possible geometries of the disc and corona in the 5 different states (figure taken from Esin et al. 1997). The solid lines represent a thin disc and the dots represent an ADAF, with denser dots representing a denser ADAF. As mass accretion rate ($\dot{m}$) increases, the ADAF becomes more radiatively efficient and therefore more luminous (a transition from the quiescent state to the LHS). The thin disc starts to extend further inwards at a critical mass accretion rate (the IS). As the mass accretion rate increases further, the HSS is reached and the disc extends down to the innermost stable orbit and the ADAF becomes a weak corona above it. The VHS is similar to the HSS, but with a stronger corona.

Several geometries of the inner regions of BHXBs have been suggested and mod-

elled to explain the different states. The HSS is modelled well by an optically thick, geometrically thin disc (Shakura & Sunyaev, 1973), but the LHS is more challenging to model. Haardt & Maraschi (1993) model two plane-parallel slabs: one cold, thermal layer emitting blackbody seed photons and one optically thin, hot slab where the seed photons are Comptonised. Alternatively, Poutanen & Svensson (1996) model a thin blackbody disc with a Comptonising plasma of hemispherical, cylindrical or pillbox shape above it. They also discuss the possibility of modelling several smaller plasma regions in the form of active regions. These and other such models are discussed in more detail in section 1.5.

Narayan & Yi (1994, 1995) develop a model of advection-dominated accretion flow (ADAF) which is first applied to the quiescent state only (Narayan et al., 1996), but is later extended and applied to several sources in different states. It is, for example, used to explain all the five states except the VHS in an outburst of the soft X-ray transient Nova Muscae 1991 (Esin et al., 1997), as well as the LHS and IS of Cyg X-1, a transition from the quiescent state to the LHS in GRO J0422+32 and the LHS, HSS and VHS in GRO J1719-24 (Esin et al., 1997).

The geometries suggested for the five different states are shown in figure 1.2 (Esin et al., 1997). The quiescent state occurs at low mass accretion rates and is explained by a thin disc (Shakura & Sunyaev, 1973) with an inner radius far from the compact object, contributing almost negligibly to the spectrum. An ADAF exists between the thin disc and the compact object. The low mass accretion rate causes a low gas density in the ADAF, and hence inefficient cooling by bremsstrahlung. Thus most of the energy in the ADAF is stored as kinetic energy and accreted into the black hole rather than being radiated away, explaining the low luminosities of the quiescent state.

At higher mass accretion rates the ADAF becomes more radiatively efficient and therefore more luminous, while the geometry remains fairly unchanged. This corresponds to the LHS. As the mass accretion rate increases further, beyond a critical rate, the disc starts to extend closer to the compact object and the ADAF

shrinks. This process occurs during the IS. The HSS is associated with a high mass accretion rate, where the thin disc extends to the innermost stable circular orbit (ISCO) and the ADAF turns into a weak corona above the disc. The VHS consists of the same thin disc as the HSS (extending to the ISCO), but with a more dominant corona, though this state is not as well described by the ADAF model.

The main mechanism for upscattering disc photons to higher energies in all the models discussed above is inverse Compton scattering in a hot, thermal electron gas, but other possibilities have been suggested. The synchrotron model by Markoff et al. (2001) uses jet emission to describe the broadband spectrum in the LHS. Synchrotron radiation dominates all wavebands, though inverse Compton scattering may contribute towards the X-ray emission. The radio emission originates in the extended jet, as is the case in Comptonisation models, but the X-ray emission is dominated by optically thin synchrotron emission from the base of the jet. The high-energy cut-off is determined by cooling losses. Other models, in addition to those described here, are discussed in more detail in the review by Done et al. (2007).

1.2 Variability

In addition to spectral information there is a wealth of temporal information available for BHXBs, as they vary both on very short timescales (down to less than a millisecond, see van der Klis (2004) for a review) as well as longer timescales ($\sim$ years). Evolution between the states described above is an example of long term variability, and although we have models which describe each individual state well (as described above, see also section 1.5) the process which initiates these changes is not well understood.

The typical evolution of BHXB outbursts through the different states is illustrated well on a hardness-intensity diagram, for example in Fender et al. (2004) where the simultaneous jet evolution is also indicated. A schematic of the typical shape of such a plot is shown in figure 1.3 (Körding et al., 2006). The y-axis repre-

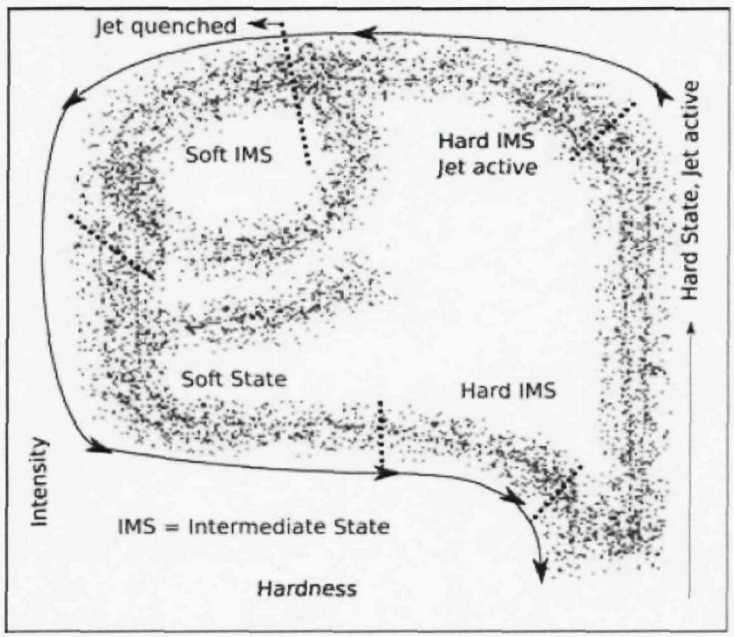

Figure 1.3: A schematic of the evolution of X-ray binaries during a typical outburst in a hardness-intensity diagram. This figure is taken from Körding et al. (2006). A BHXB usually follows the arrows on the diagram during an outburst, but sometimes diverges on the additional paths shown. For example GRS 1915+105 often circles the top left hand corner.

State	General features	Special features
LHS	flat-topped BLN	low characteristic ν_b
HSS	weak power-law noise	n/a
VHS/IS	components from the LHS and HSS	strong 3-12 Hz QPOs
quiescent state	similar to LHS	smaller characteristic ν_b

Table 1.1: An overview of the alternate definitions of X-ray binary states based on timing properties rather than spectral properties. Here ν_b refers to the break frequency, see the text for more details.

sents the bolometric X-ray luminosity, for example the count rate, while the x-axis represents the hardness ratio, a measure of how dominant the power-law component is over the blackbody bump, for example (6.3-10.5 keV count rate)/(3.8-6.3 keV count rate). The radio luminosity is also indicated in figure 1.3 in terms of when a jet is usually observed. All BHXBs seem to follow similar patterns on the hardness-intensity diagram as they evolve between states, so any consistent model of BHXBs must explain the evolution along this path on the hardness-intensity diagram as well as the presence or not, as appropriate, of a jet. In other words, it is insufficient to model the spectra of BHXBs, their spectral evolution in time must also be modelled.

Short term variability in BHXBs is characteristic of the different states described in section 1.1 and can be used to make alternative definitions of these states, as was partially done in the definition of the VHS above by using QPOs. An overview is given in table 1.1. Following the definitions given in van der Klis (2004) we observe strong (up to $\sim 50\%$) flat-topped band-limited noise (BLN) with a low characteristic break frequency (typically $\nu_b \sim 0.01$ Hz) in the LHS (i.e. the power density, P_ν, is approximately constant below ν_b and then becomes a power-law), whereas the HSS shows weak ($\lesssim 3\%$) power-law noise (the power density is a power-law, $P_\nu \propto \nu^{-\alpha}$, where $0 < \alpha \lesssim 2$). As mentioned above we observe strong 3-12 Hz QPOs in the VHS, but there are also similar components to those in the LHS and HSS. Weaker BLN than in the LHS which also extends to higher frequencies (up to ~ 10 Hz) is observed, and there is stronger power-law noise than in the HSS with rapid transitions between these components. The quiescent state is similar to the LHS but with a smaller ν_b,

sometimes as low as $\sim$ 0.0001Hz, and the IS is similar to the VHS. (This is a very brief and by no means complete listing of short term X-ray variability in X-ray binaries. See van der Klis (2004) for a review.)

As with spectral observations, several models have been developed to explain the variability in the different states. Spectral and temporal information should be combined in future models to increase our overall understanding of X-ray binaries by combining all the available information. A complete model must, as noted above, describe both the spectral and temporal aspects of X-ray binaries. This is carried out in the review by Done et al. (2007), where an extended ADAF model is used to explain the spectra, state changes and variability in both black hole and neutron star X-ray binaries.

1.3 Neutron star X-ray binaries

I have mostly discussed BHXBs above, but extensive spectral and temporal studies have also been carried out on X-ray binaries where the compact object is a neutron star, and different types and states are classified. I do not go into detail here, see van der Klis (2004) for a review. The main difference between neutron stars and black holes is that neutron stars have a surface whereas black holes have an event horizon. Because of this, the occurrence of X-ray bursts is one way of classifying a compact object as a neutron star, though the lack of X-ray bursts is not a sufficient indicator of a black hole. X-ray bursts occur when accretion of matter from the donor star builds up enough pressure on the neutron star surface for nuclear fusion of hydrogen and helium into heavier nuclei. This is an explosive event, and its energy is finally emitted as X-rays from the neutron star surface (Lewin et al., 1993), usually lasting of the order of seconds to minutes.

Overall, however, the behaviour of neutron star X-ray binaries is very similar to that of BHXBs, so much so that it can be difficult to distinguish between them. Some types and states of neutron star X-ray binaries have been associated with different states of BHXBs with mass accretion rate being the determining factor of

the state, though possibly scaled by mass in some way (van der Klis, 1994).

Both the neutron star surface and the black hole event horizon are at a distance of the same order from the compact object, thus the regions I have described here, i.e. the accretion disc and corona, are probably the same for all X-ray binaries. Models describing accretion in BHXBs are also applied to neutron star X-ray binaries. The ADAF model (Narayan & Yi, 1995), for example, considers accretion near neutron stars as well as black holes, though the lack of an event horizon in neutron stars through which kinetic energy can be 'lost' poses somewhat of a problem. This energy must be released at some point, possibly after accreting onto the surface of the neutron star.

Done & Gierliński (2003) compare state transitions in both BHXBs and neutron star X-ray binaries and find that the same physical processes describe both, but with the difference in geometry taken into account. Seed photons are provided by the surface of the neutron star as well as the accretion disc, and the boundary layer is included. A boundary layer exists between the accretion disc and the surface of neutron stars where the difference between the angular momentum of the inner disc and that of the surface of the neutron star is radiated away to allow accretion onto the neutron star. In black holes this angular momentum disappears through the event horizon. In general, with a possible modification of the geometry, accretion disc/corona models can be applied both to BHXBs and neutron star X-ray binaries.

1.4 Supermassive black holes

I have only discussed stellar mass black holes above, but supermassive black holes also exist at the centres of galaxies. If a significant amount of matter accretes onto the central black hole, radiating as it does so, then we call these systems active galactic nuclei (AGN). The dissipation of gravitational energy near supermassive black holes is in some cases so great that the optical radiation from the nucleus outshines the stars in the parent galaxy by more than a factor of 1000 (Longair, 2004).

The same physical processes and geometries that describe black hole X-ray binaries (BHXBs) are thought to apply to AGN, with a mass scaling factor. Black holes are, after all, fairly simple objects, in that they are fully described by only two parameters: mass and spin. Black holes can also have charge, but this is quickly neutralised by accretion of oppositely charged material. This is due to the electromagnetic force being much stronger than the gravitational force. Several models have been successfully applied both to X-ray binaries and AGN, for example the ADAF model described above has been applied to several X-ray binaries as well as Sgr A* (Narayan et al., 1995) and the nucleus of NGC 4649 (an elliptical galaxy) (Quataert & Narayan, 1999). Also Haardt & Matt (1993) (an extension of Haardt (1993), see section 1.5) discuss the implications of their model on the X-ray polarisation of both X-ray binaries and AGN. Due to the longer evolution time-scales and greater distances to AGN they are more difficult to observe, but if they behave as stellar mass black holes, then BHXBs provide a convenient testing ground for theories relating to AGN.

Several comparisons have been made between BHXBs and AGN to justify that AGN are scaled-up versions of BHXBs. State transitions have not been observed in AGN, but if time-scales scale linearly with mass, then state transitions in AGN would take $\sim$ millions of years and so cannot be observed on human-accessible timescales. It is possible, however, that different classifications of AGN correspond to AGN in different states similar to those described above for BHXBs. For example Ho (2005) compares the ADAF model for LHS BHXBs to low-luminosity AGN in nearby galaxies, Pounds et al. (1995) discuss the similarity between the narrow-line Seyfert galaxy RE 1034+39 and the HSS of galactic BHXBs and Maccarone et al. (2003) further compare radio-quiet AGN to HSS X-ray binaries, to name but a few.

The hardness-intensity diagrams described in section 1.2 can also be generalised to include AGN by plotting $L_D + L_{PL}$ against $L_{PL}/(L_D + L_{PL})$, a disc fraction/luminosity diagram (DFLD) (Körding et al., 2006). Such a diagram is shown in figure 1.4. Here L_D is the disc luminosity (soft X-ray luminosity for BHXBs and

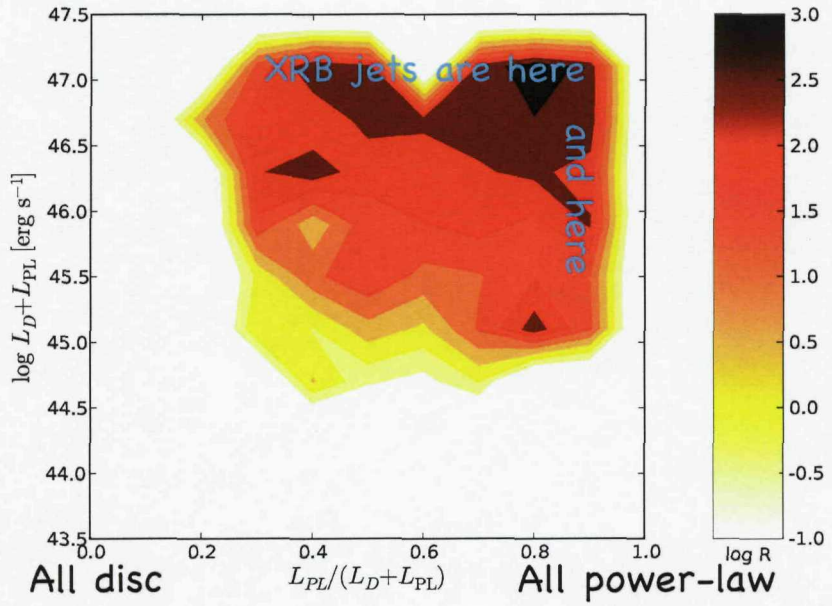

Figure 1.4: A disc fraction/luminosity diagram taken from Jester et al. (2006). The contours represent the average radio loudness of the quasars in this sample, see Jester et al. (2006) for more details.

UV luminosity for AGN) and L_{PL} is the luminosity of the power-law component (hard X-ray luminosity for BHXBs and X-ray luminosity for AGN). If the luminosity of both these components scales similarly with mass then there is no dependence on mass in a DFLD. Thus instead of plotting the evolution in time of individual sources, as in the hardness-intensity diagrams, a large sample of sources in different states is plotted. The authors find good agreement between the DFLD of a large sample of AGN and of a simulation of BHXBs, strengthening the theory that AGN are upscaled versions of the black holes in galactic BHXBs.

Yet another indicator of the similarities between BHXBs and AGN is the fundamental plane of black hole activity (Merloni et al., 2003; Falcke et al., 2004; Körding et al., 2006). The X-ray luminosity, L_X, radio luminosity, L_R, and black hole mass are correlated and create a fundamental plane when plotted. This correlation extends from supermassive black holes in AGN to stellar mass black holes.

Also the variability of BHXBs and AGN show similar characteristics. The break

frequency discussed in section 1.2 is also observed in AGN, and McHardy et al. (2006) find a relationship between the break frequency, the mass of the black hole and the mass accretion rate which is valid both for AGN and BHXBs.

Models developed to describe X-ray binaries can therefore also be applied to AGN and vice versa. Similarly to neutron stars, however, an adjustment in geometry may be necessary. An accretion disc wind, expected from the colder discs in AGN, may make a significant difference to AGN spectra (Done & Gierliński, 2005).

1.5 Other codes

I have given a qualitative introduction to the current models describing the geometries and processes of X-ray binaries and AGN above, but much quantitative work has led to the development of these ideas. For example, the spectral shape created by multiple Compton scattering events of soft photons in a thermal electron plasma is used frequently above, but is not trivial to calculate. More such modelling is required to develop the current models further and find observable signatures to distinguish between them. I present such a model in this thesis, and here I give a short introduction to existing models, using both analytic approaches and Monte Carlo simulations, which are devoted to modelling the physical processes which dominate the spectra from X-ray binaries and AGN. A summary is given in table 1.2.

An early analytic approach to predicting the Comptonised spectrum of soft seed photons propagating through a hot plasma is presented in Sunyaev & Titarchuk (1980), where they split the problem into two. First they consider an instantaneous flash of photons occurring at the centre of a source at time $t = 0$. The luminosity of the flare is described by the delta function $\delta(t)$. By solving the photon diffusion problem in the source they obtain P(t), the distribution of photons over their escape times. Secondly they solve the stationary Kompaneets equation in an infinite, homogeneous medium of non-relativistic, thermal electrons to obtain the Compton scattered spectrum, $I(\nu, t)$, at time t, given an initial spectrum $I_0(\nu, t = 0)$, where ν is frequency. By combining these two results, $\Psi = I(\nu, t)P(t)$, they obtain the

Model	Method	Processes	Validity
Sunyaev & Titarchuk (1980)	A	c	$\tau \gg 1, \Theta \lesssim 0.2$
Pozdnyakov et al. (1983)	A/MC	c	$\tau \gtrsim 2$
Titarchuk (1994); Hua & Titarchuk (1995)	A	c	$\tau \gtrsim 0.2, \Theta \lesssim 0.3$
Zdziarski (1985)	A	c,b,s,p	$1.4 \lesssim \Gamma \lesssim 2.5$
Skibo & Dermer (1995)	MC	c,b,p	
Haardt & Maraschi (1991); Haardt (1993); Haardt & Maraschi (1993)	A/MC	c,p,r	$\tau \lesssim 1$
Poutanen & Svensson (1996)	A	c,b,p,r	$\tau \lesssim 0.7$
Coppi (1992)	A	c,b,s,p,r,t	
Stern et al. (1995a)	LPMC	c,b,s,p,r,t	

Table 1.2: A summary of the radiative transfer models discussed here. The symbols used are as follows: A = analytic, MC = Monte-Carlo, LPMC = large particle Monte Carlo, c = Compton scattering, b = bremsstrahlung, s = synchrotron radiation, p = treatment of pairs, r = reprocessing, t = treatment of evolution in time. Validity ranges are given where they are available in the literature, either through comparisons to other models or by specific approximations used in a model. More general limitations apply to other models, for example Coppi (1992) uses escape probabilities, and Stern et al. (1995a) is limited by run-times. More details are given in the text.

emitted spectrum at time t if an instantaneous flare occurred at the centre of the source at time t = 0. This result is useful for modelling X-ray bursts, for example. In order to calculate the emitted spectrum of a source with constant photon input at the centre, rather than a delta function, such as an accretion disc in X-ray binaries provides, the authors integrate Ψ over time, $F(\nu) = \int_0^\infty I(\nu, t)P(t)\mathrm{d}t$. If the 'flare' has been on constantly, then the emitted spectrum is the sum of the spectra emitted due to a flare at all times from 0 to ∞. Hence we have an analytic expression for the Comptonised spectrum of a non-relativistic ($kT_e \ll mc^2$ where m is the electron mass and c is the speed of light in a vacuum), thermal electron plasma where seed photons originate at the centre of a source. Due to the use of the diffusion approximation, this treatment is only valid for high Thomson optical depth ($\tau \gg 1$) and combined with the lack of a relativistic treatment, its uses in interpreting data are, however, limited (Skibo & Dermer 1995, Titarchuk 1994).

Pozdnyakov et al. (1983) extend the range of the Sunyaev & Titarchuk (1980)

approach to be valid at lower optical depths ($\tau \sim 2$). Sunyaev & Titarchuk (1980) solve the following Kompaneets equation:

$$\frac{1}{x^2}\frac{\mathrm{d}}{\mathrm{d}x}x^4\left(\frac{\mathrm{d}N}{\mathrm{d}x}+N\right)=\gamma N-\frac{\gamma f(x)}{x^3}. \tag{1.1}$$

On the left is the differential Kompaneets operator with the first term in the brackets representing the Doppler effect and the second the recoil effect of Compton scattering. Induced processes are not included. The first term on the right represents photon diffusion out of the source and the second describes a source of seed photons, f(x). Also,

$$\gamma=\frac{\pi^2}{3}\frac{mc^2}{(\tau+\frac{2}{3})^2kT_e} \tag{1.2}$$

for a spherical plasma source. Using Monte Carlo simulations, Pozdnyakov et al. (1983) obtain a correction to equation 1.2 and the equivalent equation for a disc geometry, with the spherical case being corrected to

$$\gamma=\frac{\pi^2}{4}\frac{mc^2}{(\tau+0.5)kT_e}. \tag{1.3}$$

This is related to the spectral index α by

$$\alpha=-\frac{2}{3}+\sqrt{\frac{9}{4}+\gamma}. \tag{1.4}$$

More recently Titarchuk (1994) includes relativistic corrections to the model by Sunyaev & Titarchuk (1980) as well as extending the model's validity to low optical depths ($\tau < 1$). While maintaining the same approach, i.e. solving the diffusion equation and the Kompaneets equation for an infinite, homogeneous medium and combining the two, Titarchuk (1994) includes Klein-Nishina effects. Compton scattering becomes decreasingly efficient as the electron temperature increases, causing the high energy tail of the spectrum to steepen with the inclusion of this effect. Titarchuk (1994) also argues that the diffusion approximation is valid at low as well

as high optical depths, as the X-ray spectrum at high photon energies is created by photons undergoing many more scatterings than average. These photons must be travelling along the longest escape route, i.e. along a diameter in a sphere or parallel to the disc in a disc geometry, though they are no longer isotropic, but collimated instead. He modifies the diffusion coefficients for the collimated case and proceeds as before, creating a model more applicable to the situations in X-ray binaries, which are thought to contain plasmas of lower optical depths.

Hua & Titarchuk (1995) further extend these modifications and compare their results to Monte Carlo simulations (see also Skibo & Dermer 1995 for comparisons to Monte Carlo simulations). Although the agreement is good, improvements could still be made. Important physical processes such as bremsstrahlung, synchrotron radiation, pair production and annihilation, Coulomb interactions and reprocessing and reflection are neglected in all the models discussed above.

Various models have been developed which take into account some of these additional processes. Skibo & Dermer (1995) include mildly relativistic ($\Theta = \frac{kT_e}{mc^2} \lesssim 2$) thermal plasmas in pair balance, where the particles are distributed uniformly in a spherical geometry, in their Monte Carlo simulations. Their model includes an external source of seed photons (assumed to be either monoenergetic or blackbody) in addition to seed photons created by electron-ion, electron-electron and electron-positron bremsstrahlung, and the distribution of directions of the photons is modelled. They find that bremsstrahlung becomes important when $\tau \gtrsim 1$ and $\Theta \gtrsim 1$. Skibo & Dermer (1995) also compare their model to the models by Sunyaev & Titarchuk (1980), Hua & Titarchuk (1995) and Zdziarski (1985), and recommend using the models of Sunyaev & Titarchuk (1980) only for $\tau \gtrsim 2, \Theta \lesssim 0.2$, Hua & Titarchuk (1995) for $\tau \gtrsim 0.2, \Theta \lesssim 0.3$ and Zdziarski (1985) for $1.4 \lesssim \Gamma \lesssim 2.5$, where Γ is the spectral index.

Zdziarski (1985) includes a detailed study of pair balance, modelling pair production, annihilation and escape for a relativistic thermal plasma of electrons, positrons and protons in a spherical geometry. Synchrotron radiation is considered as a pos-

sible source of photons in addition to a standard blackbody, and bremsstrahlung is calculated separately and dominates the spectrum if relevant. The radiative transfer is treated less accurately, however. He uses the fact that multiple Compton scattering events of photons by thermal electrons produce a power-law up to $h\nu \sim kT_e$, with the spectral index given in Sunyaev & Titarchuk (1980), and corrected to be valid for mildly relativistic electrons. This is true when the emitted spectrum is independent of the seed photons, which occurs when the average number of scattering events, which is approximately τ^2, is much greater than one (Sunyaev & Titarchuk, 1985). The seed photons 'forget' their origin after a sufficient number of scattering events. A somewhat ad hoc exponential cut-off is modelled at $h\nu \sim kT_e$ and a Wien spectrum is used to model energies $h\nu \gtrsim kT_e$ where the photons are in thermodynamic equilibrium with the electrons. This model is compared to Monte Carlo simulations in Zdziarski (1986).

Haardt & Maraschi (1991) use the analytic treatment of Zdziarski (1985) in addition to Monte Carlo simulations to model reprocessing and reflection in the disc, introducing a two-phase geometry of coupled plane-parallel slabs: the hot, Comptonising phase and the cool disc. Some Comptonised photons from the hot phase hit the disc and are either reprocessed in the disc to contribute to its thermal radiation or downscattered in the upper layers of the disc and reflected, creating a characteristic reflection bump at approximately 10-300 keV. The model includes pair production, annihilation and pair balance, and the authors also note the importance of including the anisotropy of Compton scattering.

The analytic treatment of the anisotropy of Compton scattering from Haardt & Maraschi (1991) is extended in Haardt (1993). The spectrum is written as

$$\sum_k p_k S_k \tag{1.5}$$

where p_k is the escape probability and S_k is the photon spectrum in an infinite, homogeneous medium after k scattering events. The author then computes p_k for all k and the evolution from S_k to S_{k+1}. Isotropic conditions are assumed, but

dimensionless coefficients taking into account the degree of anisotropy give 'effective' values for the temperature and angular patterns of scattering events, allowing the angle between the photon and electron trajectories to be taken into account for individual scattering events.

The geometry of the system is modelled by weighting the escape probability depending on which direction the photon is travelling in. For example, in the slab geometry considered here a photon travelling parallel to the disc has a smaller escape probability than one travelling perpendicularly to the disc. This treatment requires that the energy and angular distributions of the input photon distribution are separable, i.e. $S_0(x,\mu) = S_0(x)U_0(\mu)$ where S_0 is the input photon spectrum, x is the photon energy and μ is the cosine of the angle between the photon direction before scattering and the normal to the slab.

Only the anisotropy of the first scattering event is considered, and only relativistic Maxwellian or monoenergetic electron distributions are treated, but the method can, in principle, be extended to include the anisotropy in higher order scattering as well as other electron distributions. Using this procedure, the authors compute different spectra for different viewing angles, emphasising the importance of this feature in a model. The model of Haardt & Maraschi (1991) is then improved on in Haardt & Maraschi (1993) using this improved analytic treatment from Haardt (1993).

The models described so far are limited by the plasma geometries (slab and spherical) and the electron energy distributions (relativistic Maxwellian and monoenergetic) they model. Poutanen & Svensson (1996) include the capability of modelling active regions of cylindrical and spherical geometries, i.e. several small, spatially separated plasma regions located above the disc as opposed to one large one, as well as the single corona geometries described above. They model bremsstrahlung, pair production, annihilation and pair balance as well as reprocessing and reflection in the disc and the polarisation and angular dependence of inverse Compton scattering and reflection. The model is, however, limited to modelling rel-

ativistic Maxwellian electron distributions and coronae of uniform temperature and density distributions. It is a one-dimensional code, so any corona must be collapsible to one dimension. It is also only valid for fairly small optical depths (τ up to ~ 3 depending on geometry and plasma temperature).

All the above models simulate steady-state situations, but there is a considerable amount of variability data available in addition to spectral data (see section 1.2). It is therefore desirable to construct models that can combine predictions for the spectra of Comptonising plasmas with a treatment of their temporal variability. As noted earlier, it is important to combine all the available information, both spectral and temporal, to develop consistent models describing X-ray binaries.

Coppi (1992) models time-dependent situations by changing the particle injection rate and considering the relaxation time-scales of the various particles. He models pair plasmas with hybrid electron-positron distributions and includes a treatment of bremsstrahlung and synchrotron radiation. This is done analytically using the kinetic equation, so changes in the particle injection rate occur instantaneously throughout the plasma, and homogeneous and isotropic conditions are assumed.

Stern et al. (1995a) also present a model which is capable of simulating dynamic situations. They use a Large Particle Monte Carlo code, a Monte Carlo code operating on large particles (LPs). Each LP represents a number of particles of the same type and properties, for example one LP may represent electrons all with the same position, momentum, direction of motion and energy. These LPs can be used to create flexible coronal geometries, including inhomogeneous plasmas and hybrid electron distributions. Photons, electrons, positrons, protons, neutrons and He nuclei are modelled and their interactions include Coulomb interactions, synchrotron radiation and self-absorption, Compton scattering, pair production, annihilation, reflection and reprocessing (and more). Interactions between the LPs are determined by their mean free paths and interaction probabilities, and are created/removed/moved accordingly. Transfer of particles within the corona is thereby treated naturally and so there is no need to use escape probabilities. Particles can

also interact with particles they created earlier in the simulation, thus the model is non-linear. Angular treatments are included and different spectra for different viewing angles can be produced. This model is compared to the model by Poutanen & Svensson (1996) in Stern et al. (1995b) and used to model active regions. These two models are also used to compare the active regions geometry to the slab geometry of Haardt & Maraschi (1991) in relation to observed characteristics of Seyfert 1 galaxies. The code is developed further and used for dynamic modelling in Malzac & Jourdain (2005), modelling of bulk motion of the plasma in Malzac et al. (2001) and modelling an inhomogeneous plasma in Merloni et al. (2006).

1.6 The High Energy Astrophysical Radiative Transfer Code

I present a new code in this thesis, the High Energy Astrophysical Radiative Transfer code, hereafter the HEART code. As developed by Collins (2004), it models any electron energy distribution within the plasma, with the full range of subrelativistic to ultrarelativistic electrons. The electron distribution can be spatially inhomogeneous and there is little restriction on the geometry of the plasma. Bremsstrahlung and synchrotron radiation are included, as well as inverse Compton scattering, both as sources of soft seed photons and as cooling mechanisms for the electrons. Coulomb interactions are also modelled, and external seed photons of any distribution may be injected. Any electron temperature can be modelled as relativistic and Klein-Nishina effects are included, and in principle the model allows for any optical depth. HEART also has potential for timing analysis, as the evolution of the electron and photon distributions are modelled with time as well as in a steady state.

In its current form the HEART code does not treat anisotropic Compton scattering, the creation and annihilation of electron-positron pairs, electron transport, energy balance or reprocessing. On testing the HEART code in a simple case, these limitations, amongst others, are found to significantly restrict its applicability.

As several codes exist which model radiative transfer successfully with significantly fewer limitations, as well as faster than HEART, a complete restructuring of the code is required if it is to be used.

Chapter 2 is devoted to an introduction to the HEART code as developed by Collins (2004). The further developments I have introduced are described in chapter 3. Using these additions, the code is tested and compared to the analytic work of Titarchuk (1994) in chapter 4, as well as being used to fit observational data from Cyg X-1 in the LHS and the HSS. Throughout chapter 4 the code is limited to basic spectral fitting to allow for simple testing and comparison to previous work, and I discuss the applicability of HEART in this context. Modelling of dynamic systems is a potential strength of HEART and is developed and tested in chapter 5, as a state transition from the HSS to the LHS and an X-ray burst in Aql X-1 are modelled. Several limitations in the structure of HEART become apparent throughout this work, and these are discussed in chapter 6. I conclude in chapter 7 by highlighting the key issues and limitations of the code.

Chapter 2

Introduction to the HEART code

The HEART code models radiative transfer of soft photons in a region of arbitrary geometry containing hot electrons, hereafter referred to as the corona. The corona is divided into independent cells, between which photons, but not electrons, are exchanged, and additional seed photons originating outside the modelled region may be added. HEART can, in principle, be applied to X-ray binaries and AGN to explain their spectra and evolution over time. In this case soft photons are emitted from the accretion disc, before traversing a corona of some given geometry and electron composition.

Several physical processes are modelled in the corona, including inverse Compton scattering, bremsstrahlung, synchrotron radiation and Coulomb interactions. This chapter is dedicated to giving an overview of the HEART code as created by Collins (2004). The current form of the code is developed further and then tested. A discussion of the results of this testing and the limitations of HEART are given in chapter 6.

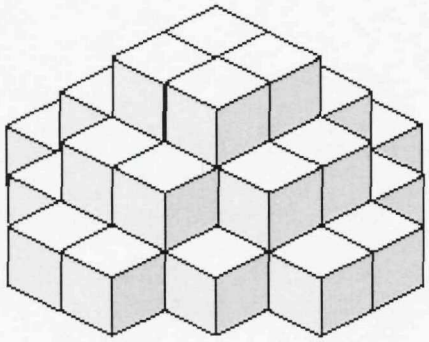

Figure 2.1: The cell structure of a spherical corona with a diameter of 6 cells. Only one hemisphere is shown and modelled. This figure is taken from Collins (2004).

2.1 Overview of the code

The first part of the model involves constructing the corona. Cubic cells are used to construct the required geometry with which practically any 3D shape can be approximated. To reduce computation time, only geometries which have at least one plane of symmetry, for example a circular accretion disc in a spherical corona, can be modelled, so that it is only necessary to model half the corona. Figure 2.1 shows how HEART approximates a spherical corona with a diameter of 6 cells. If an accretion disc below the hemisphere is modelled, then 24 cells are adjacent to the disc into which multicolour blackbody radiation can be injected (see section 2.2.4). These are called injection cells.

When the cells are created at the start of a simulation they are each linked to their neighbouring cells so that photon distributions can be transferred from one cell to the next. Cells are initially created upwards from the centre to the desired height, and then outwards perpendicularly to the required width at the top. The rest of the highest level is then filled. The next level down is created in a similar way using existing links to link the new cells to the cells above them. This process, illustrated in figure 2.2, introduces some constraints on the geometry of the modelled plasma, for example geometries with hollows cannot be constructed. However, hollows can,

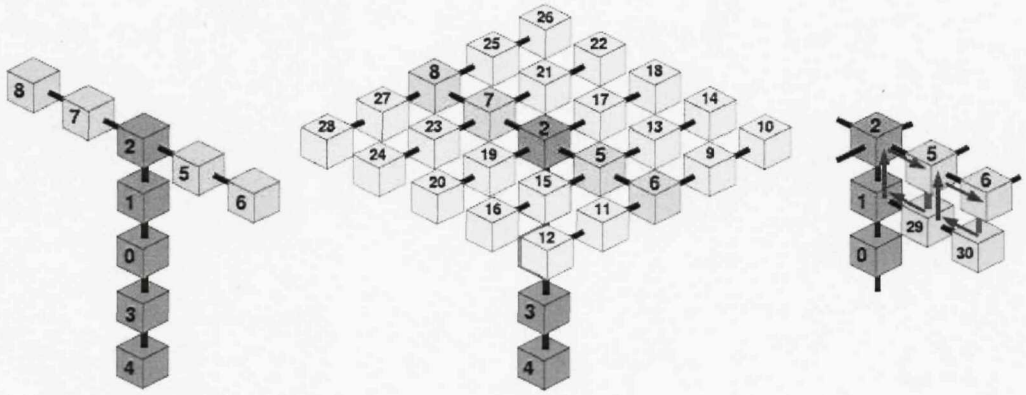

Figure 2.2: A depiction of the algorithm used for constructing the corona. Cells are initially created upwards from the centre to the desired height, and then outwards in two perpendicular directions to the required width at the top. The rest of the highest level can then be filled in. The next level down is created in a similar way using existing links to link the new cells to the cells above them. This figure is taken from Collins (2004).

in principle, be created by introducing empty cells[1].

After the corona has been constructed in the desired geometry, electron distributions are injected into each cell. These distributions are discretised into (usually logarithmically spaced) energy bins and are given by the number of electrons in each energy bin. These usually represent a thermal and/or power-law distribution (see section 2.2.1), though any distribution can be modelled using this discretised representation.

Seed photon distributions, for example a multi-colour blackbody from an accretion disc, though any distribution is possible, are then transferred into each injection cell, for example into those cells neighbouring the accretion disc in a disc geometry (see section 2.2.4). Initially all photons in a disc geometry travel upwards, but after scattering within cells, six directions are modelled, and each cell contains six corresponding photon distributions travelling in six directions through the cell[2]. Each distribution travels in one of the directions parallel to the sides of the cell and

[1] I implement this later. See section 3.3

[2] This significantly limits the geometries HEART can model in a physical way, see section 6.2 for more details.

scattered photons are distributed equally in each of these directions[3]. The photon distributions are discretised similarly to the electron distributions with an intensity representing the number of photons in each energy bin. The energy bins for the photons are also usually logarithmically spaced, but this is independent of the spacing of the electron bins.

By design only one scattering event per photon is possible in any given cell, and therefore the optical depth of each cell must be considerably less than unity. An optically thick corona must be modelled by several cells.

The radiative processes are calculated in every cell (as described in section 2.2) for every timestep. A timestep is defined as the time taken for light to cross a single cell, i.e.

$$\text{timestep} = \frac{\text{width of cell}}{c}, \tag{2.1}$$

and so a photon travelling through a cell without interaction with an electron travels from one cell to the next in each timestep without changing its properties. As photons can only travel in any of the six directions parallel to the sides of a cell, a photon crosses a cell in exactly one timestep.

The kinetic equation and Coulomb interactions determine the electron distributions in each cell for every timestep, and electrons may be injected as well as escape. In this way, the electron and photon distributions evolve simultaneously in every cell in each timestep. This functionality allows the calculation of self-consistent and time-dependent[4] situations.

Finally, photons leaving the corona through cells with surfaces not occupied by neighbouring cells or the disc are added to the output flux. Note that it takes photons a few timesteps to reach the outermost cells, at least 3 timesteps in figure

[3]For relativistic electrons, scattering in the direction of motion of the electron is significantly more likely than any other direction. An isotropic electron and photon distribution is assumed in each cell, and a resulting isotropic scattered photon distribution is also assumed. This restricts the validity of the modelled inverse Compton scattering, especially in situations where there is bulk motion of the electrons through the corona.

[4]I have made some necessary modifications to model time-dependent situations. See chapter 5.

2.1. Hence the observable flux from the corona needs a few timesteps to establish itself in a steady state. Further constraints arise in the simulation of an optically thick corona where photons may be scattered many times before escaping from a surface cell (see section 4.1).

2.2 Physical Processes

The physical processes modelled in the corona are bremsstrahlung, synchrotron radiation, Compton and inverse Compton scattering and Coulomb interactions, and the electron distribution in individual cells evolves in time as determined by the kinetic equation. This includes all physical processes likely to be occurring in the corona enveloping the accretion disc of X-ray binaries as well as AGN up to a photon or electron energy of 511 keV when pair production and annihilation also become important.

I describe the processes within a single cell first. In particular, I start with the electron distribution, as electrons are confined to a single cell. The radiative processes are then described.

2.2.1 The Kinetic Equation

An electron distribution is modelled in each cell, with the combined electron distributions of all the cells making up the electron distribution of the corona. The evolution of the electron distribution under the influence of the local radiation field (see section 2.2.3) in each cell is given by the kinetic equation (e.g. Ghisellini et al. 1988) in the form of a Fokker-Planck equation,

$$\frac{\partial n_\gamma}{\partial t} = \frac{\partial}{\partial \gamma}\left[B(\gamma) n_\gamma + H(\gamma)\frac{\partial n_\gamma}{\partial \gamma}\right] + Q(\gamma) - \frac{n_\gamma}{T(\gamma)}, \tag{2.2}$$

where n_γ is the number of electrons with energy $\gamma m_e c^2$ (m_e is the rest mass energy of an electron), $\gamma = 1/\sqrt{1-\beta^2}$ and β is the particle velocity divided by c. $B(\gamma) = \Lambda(\gamma) - H(\gamma)\left(\frac{\gamma^2+p^2}{\gamma p^2}\right)$ where $p = \sqrt{\gamma - 1}$, the electron momentum. $T(\gamma)$,

$H(\gamma)$ and $\Lambda(\gamma)$ are discussed below, but in short they are the sink function, the induced energy gains and losses (see equation 2.5) and the cooling rate due to free energy losses (see equation 2.6) of the electron distribution respectively. $Q(\gamma)$ is an optional source function, and is modelled by injecting a given electron distribution.

The thermal component of the injected electron distribution is described by the relativistic form of the Maxwell-Boltzmann equation (Synge, 1957), where n_γ is the number density per unit time of injected electrons with energy $\gamma m_e c^2$,

$$n_\gamma = \frac{n_e}{\Theta_e K_2(1/\Theta_e)} \gamma p e^{-\gamma/\Theta_e}, \tag{2.3}$$

where $\Theta_e = kT_e/m_e c^2$, k is the Boltzmann constant and K_2 is the modified Bessel function of order 2. n_e is the total electron number density injected per unit time, independent of electron energy, and is set by the user (see section 2.3).

The power-law component is modelled by

$$n_\gamma = n_0 \gamma^{-q}, \tag{2.4}$$

where $n_0 = n_e(q-1)$ and q is the power-law index. n_e is defined as above and is also set by the user (see section 2.3). The calculation of the kinetic equation, equation 2.2, may be disabled and the electron evolution not modelled. In this case n_γ is the number density of the electrons with energy $\gamma m_e c^2$ without the time dependence.

HEART models the electron distribution in each cell by creating a number of energy bins and determining the number density of electrons per energy bin. This allows any electron distribution to be modelled, not only a hybrid thermal and power-law distribution.

$T(\gamma)$ in equation 2.2 is the sink function and is determined by an optional escape timescale. If $T(\gamma) = 2\Delta t$, where Δt is the length of one timestep, for example, then the number density of each electron energy bin from the previous timestep is halved and subtracted from the current electron distribution in each cell, equivalent to an

electron escape timescale of two timesteps. The escape time[5] is set by the user, see section 2.3.

Apart from $Q(\gamma)$ and $T(\gamma)$, the rest of equation 2.2 describes the evolution of the electron energy due to radiative processes. $H(\gamma)$ accounts for photon absorption and $\Lambda(\gamma)$ accounts for the electron energy losses due to the radiative processes modelled. These are given by

$$H(\gamma) = \frac{1}{2m_e{}^2c^2} \int \frac{I_\nu}{\nu^2} [j_{\nu_S}(\gamma) + j_{\nu_B}(\gamma)] \mathrm{d}\nu \tag{2.5}$$

and

$$\Lambda(\gamma) = -\dot{\gamma}_S - \dot{\gamma}_C - \dot{\gamma}_B \, . \tag{2.6}$$

Here j_{ν_S} and j_{ν_B} are the synchrotron and bremsstrahlung emissivity, defined in sections 2.2.3.1 and 2.2.3.2 respectively. $\dot{\gamma}_S$, $\dot{\gamma}_B$ and $\dot{\gamma}_C$ are the synchrotron, bremsstrahlung and Compton cooling rates defined in sections 2.2.3.1, 2.2.3.2 and 2.2.3.3 respectively.

The kinetic equation (equation 2.2), is solved numerically in every timestep for each cell using the Chang-Cooper method (Chang & Cooper, 1970). Park & Petrosian (1996) found this scheme to be the most accurate and efficient algorithm for this purpose. The solution method requires the discretisation of the energy distributions of both the photons and the electrons. The bin size and number can be chosen freely in HEART, but logarithmically spaced bins are most convenient for power-law distributions.

2.2.2 Coulomb interactions

As well as evolving due to radiative processes, electron injection and escape, the electron distribution evolves due to Coulomb interactions. This is similar to bremsstrahlung, but operates between individual electrons and the net electric field of

[5]The escape time may depend on the individual electron energy, a feature I added. See section 3.4.

the electron distribution as a whole. It is a non-radiative energy exchange with the overall effect of thermalising the electron distribution. The treatment of Nayakshin & Melia (1998) is used, defining a kinetic equation of the form

$$\frac{\partial n_\gamma}{\partial t} = \frac{\partial}{\partial \gamma}\left[a(\gamma, n_\gamma) n_\gamma\right] + \frac{\partial^2}{\partial \gamma^2}\left[D(\gamma) n_\gamma\right], \tag{2.7}$$

where $a(\gamma) =< \dot{\gamma} >$ is the mean energy exchange and $D(\gamma) = \frac{\mathrm{d}}{\mathrm{d}t} < (\Delta\gamma)^2 >$ is the dispersion of the energy exchange. The corrected version given in Blasi (2000) is used (see appendix A.1).

Coulomb interactions often operate on faster timescales than the other physical processes modelled, and hence they can thermalise electron distributions on a timescale t_c shorter than a typical timestep in HEART, Δt. In order to model the thermalisation process accurately with sufficient time resolution, the Coulomb coefficients are calculated and the Fokker-Planck equation solved (equation 2.7) as many times as required within Δt to ensure $t_c \leq (\Delta t/20)$. This sub-division of the timestep is only calculated if necessary, i.e. in cases of high electron density when Coulomb interactions become very efficient. The other radiative transfer coefficients in equation 2.2 are not re-calculated for each sub-time-step, t_c.

2.2.3 Radiative Processes

I now describe the radiative processes arising from interactions between the electrons and the photon field. As for the processes described above, these are calculated in each cell for every timestep. Photons travel in one of the six directions parallel to the sides of a cell (see section 2.1), and each of these six photon distributions is modelled individually in each cell. Isotropic conditions are assumed for the electron population in each cell, and so the radiative emission from each process is locally emitted equally in each of these six directions. This assumption does not force the corona as a whole to be homogeneous as different cells can contain different electron and photon distributions.

Similarly to the electron distribution (see section 2.2.1), the photon distributions

are modelled by assigning an intensity of photons to discrete energy bins covering the total modelled photon energy range. This allows us to model any spectrum that may arise. As each process is calculated, the emitted (or absorbed or scattered) intensity is added to (or subtracted from) the total intensity of each energy bin for each of the six photon distributions.

Synchrotron radiation, bremsstrahlung, Compton and inverse Compton scattering are modelled similarly[6]. From the principle of detailed balance the radiative transfer equation for each process can be derived (Rybicki & Lightman, 1979) and applied to each photon distribution,

$$I_\nu(\tau_\nu) = S_\nu(1 - e^{-\tau_\nu}), \tag{2.8}$$

where I_ν is the intensity at frequency ν. In HEART this is the intensity of photons in a particular energy bin determined by ν. τ_ν is the optical depth and $S_\nu = \epsilon_\nu/\kappa_\nu$ is the source function, where ϵ_ν and κ_ν are the emission and absorption coefficient for a given radiative process respectively. In general the single particle emissivity, j_ν, is

$$j_\nu = \frac{\mathrm{d}E}{\mathrm{d}t\mathrm{d}\nu} = h\nu n_{ip} v \sigma_\nu, \tag{2.9}$$

where n_{ip} is the number density of particles available for interaction, v is their speed and σ_ν is the interaction cross-section. E is energy and h is the Planck constant. The emission coefficient can then be found,

$$\epsilon_\nu = \frac{\mathrm{d}E}{\mathrm{d}t\mathrm{d}V\mathrm{d}\Omega\mathrm{d}\nu} = \frac{1}{4\pi}\int j_\nu n_\gamma \mathrm{d}\gamma, \tag{2.10}$$

where n_γ is the number density of particles with energy $\gamma m_e c^2$. V is volume and Ω is solid angle. The absorption coefficient is

$$\kappa_\nu = \int n_\gamma \sigma_\nu \mathrm{d}\gamma. \tag{2.11}$$

[6]Annihilation is not modelled as positrons are not modelled.

By specifying the interaction cross-section and emissivity for synchrotron radiation, bremsstrahlung and Compton scattering separately, these equations can be used in each case.

2.2.3.1 Synchrotron Radiation

Equation 2.8 is used to model synchrotron radiation, where j_ν, as defined by equation 2.9, can be expressed as (Rybicki & Lightman, 1979)

$$j_\nu = \frac{\sqrt{3}e^3 B \sin(\alpha)}{4\pi\epsilon_0 m_e c} F_S(x), \tag{2.12}$$

where B is the magnetic field strength, α is the pitch angle between the velocity of the electron and the magnetic field line and ϵ_0 is the electric permeability of free space. The spectral shape of the single electron emissivity is described by $F_S(x)$, with $x = \nu/\nu_c$. The critical frequency of synchrotron radiation, ν_c, is defined below. κ_ν, as given by equation 2.11, can be found by using the absorption cross-section in the Thomson limit ($h\nu \ll m_e c^2$),

$$\sigma_S(\nu, \gamma) = \frac{1}{8\pi m_e \nu^2} \frac{1}{\gamma p} \frac{\partial}{\partial \gamma}[\gamma p j_\nu(\gamma)]. \tag{2.13}$$

$F_S(x)$ is implemented in the HEART code as

$$F_S(x) = x \int_x^\infty K_{\frac{5}{3}}(z) \mathrm{d}z, \tag{2.14}$$

where $\nu_c = (3\gamma^2)/(2\beta)\nu_g \sin(\alpha)$ is the critical frequency at which most of the radiation is emitted, $\nu_g = (eB)/(2\pi m_e)$ is the gyro frequency and $K_{5/3}(z)$ is the modified Bessel function of the second kind of order 5/3. The solution of equation 2.14 is split into 5 different regimes:

1. relativistic electrons ($\gamma \geq 2$)[7] in the limit $x \ll 1$,
2. relativistic electrons ($\gamma \geq 2$) in the limit $x \gg 1$,

[7] $\gamma = 2$ corresponds to an electron of 2 times the electron rest mass energy, i.e. a kinetic energy of 511 keV.

3. relativistic electrons ($\gamma \geq 2$) for all other values of x,
4. non-relativistic electrons ($\gamma < 2$) where $\nu > \nu_g$,
5. non-relativistic electrons ($\gamma < 2$) where $\nu \leq \nu_g$.

In all cases we average over a uniform pitch angle distribution.

In the limiting cases 1 and 2, $F_S(x)$ can be expressed quite simply as

$$F_S(x) = \frac{4\pi}{\sqrt{3}\Gamma(\frac{1}{3})}(\frac{x}{2})^{\frac{1}{3}} \quad ; \quad x \ll 1, \tag{2.15}$$

$$F_S(x) = \sqrt{\frac{\pi}{2}}xe^{-x} \quad ; \quad x \gg 1, \tag{2.16}$$

respectively, where Γ is the gamma function. These are used to calculate j_ν in the code as long as they are at least 99% accurate. In case 3, equation 2.12 can be solved exactly to give (Ghisellini et al., 1988)

$$j_\nu(\gamma) = \frac{\sqrt{3}e^2}{\epsilon_0 c}\nu_g x_1^2 \left\{ K_{\frac{4}{3}}(x_1)K_{\frac{1}{3}}(x_1) - \frac{3}{5}x_1 \left[K_{\frac{4}{3}}(x_1)^2 - K_{\frac{1}{3}}(x_1)^2 \right] \right\}, \tag{2.17}$$

where $x_1 = \nu/(3\gamma^2\nu_g)$.

Case 4 is used for mildly relativistic electrons ($\gamma < 2$). Here equation 2.12 can be written (Ghisellini et al., 1988)

$$j_\nu(\gamma) = \frac{\pi e^2 \nu_g}{12\epsilon_0 c}\left\{1 + 2(\gamma^2 - 1)x_2\right\}^{-\frac{1}{2}} \exp\left\{\frac{2\nu}{\nu_g}x_2\right\}, \tag{2.18}$$

where

$$x_2 = 1 + \gamma \ln\left(\frac{\sqrt{\gamma_2 - 1}}{1 + \gamma}\right). \tag{2.19}$$

Finally in case 5 the emission coefficient is assumed to be zero. This is a reasonable assumption as the power emitted varies as γ^2 (Rybicki & Lightman, 1979), and so electrons at low energies emit negligible amounts of radiation in comparison to

higher energy electrons. Because $\nu < \nu_g$, the radiation is also emitted at frequencies much lower than normally observable.

The synchrotron cooling rate, $\dot{\gamma}_S$, used in equation 2.6, is determined by noting that, for a single electron (Rybicki & Lightman, 1979),

$$\frac{\mathrm{d}\gamma}{\mathrm{d}t} = \frac{4\sigma_T}{3m_e c} U_B \gamma^2, \tag{2.20}$$

where $U_B = B^2/(2\mu_0)$ is the magnetic field energy density and σ_T is the Thomson cross-section for an electron. This is integrated over an isotropic pitch-angle distribution of the electrons to give (Rybicki & Lightman, 1979),

$$\dot{\gamma}_S = \frac{1}{m_e c^2} \int_0^\infty j_\nu(\gamma) \mathrm{d}\nu. \tag{2.21}$$

2.2.3.2 Bremsstrahlung

As for synchrotron radiation, bremsstrahlung emission is calculated using equation 2.8 in each cell, for every timestep. Only electron-electron bremsstrahlung is modelled as HEART only follows the evolution of electrons. Using equation 2.9, the emissivity of a mildly relativistic electron ($1 + \frac{h\nu}{m_e c^2} < \gamma < 2$) interacting with other mildly relativistic electrons is

$$j_{\nu,mr}(\gamma) = h\nu c n_{e,mr} \sigma_{\nu,mr}(\gamma), \tag{2.22}$$

and the emissivity of an ultra relativistic electron ($\gamma \geq 2$) interacting with either a mildly relativistic electron or another ultra relativistic electron is

$$j_{\nu,ur}(\gamma) = h\nu c(n_{e,mr} + 2n_{e,ur}) \sigma_{\nu,ur}(\gamma). \tag{2.23}$$

Note that the emission from ultra relativistic electrons interacting with each other is twice as large as that of ultra relativistic electrons interacting with mildly relativistic electrons (Zdziarski et al., 1990). The emissivity and absorption coefficients are then

$$\epsilon_\nu = \frac{h\nu c}{4\pi\sigma_T l}\left[\tau_{T,mr}\int_1^{\gamma_{ur}} n_\gamma \sigma_{\nu,mr} d\gamma + (\tau_{T,mr}+2\tau_{T,ur})\int_{\gamma_{ur}}^{\gamma_{max}} n_\gamma \sigma_{\nu,ur} d\gamma\right] \quad (2.24)$$

and

$$\kappa_\nu = \frac{hc}{8\pi m_e \sigma_T l \nu}\left[\tau_{T,mr}\int_1^{\gamma_{ur}} \frac{n_\gamma}{\gamma p}\frac{d}{d\gamma}(\gamma p \sigma_{\nu,mr}) d\gamma + (\tau_{T,mr}+2\tau_{T,ur})\int_{\gamma_{ur}}^{\gamma_{max}} \frac{n_\gamma}{\gamma p}\frac{d}{d\gamma}(\gamma p \sigma_{\nu,ur}) d\gamma\right] \quad (2.25)$$

using equations 2.10 and 2.11 respectively. $\sigma_{\nu,ur}$ and $\sigma_{\nu,mr}$ are the interaction cross-sections and are given below in the mildly relativistic (Gould, 1980) and ultra relativistic (Zdziarski et al., 1990) cases respectively,

$$\sigma_{\nu,ur}(\gamma) = \frac{3\alpha_f \sigma_T}{2\pi\nu}\zeta\left(\zeta + \frac{1}{\zeta} - \frac{2}{3}\right)\left(ln\left(\frac{2\gamma^2\zeta}{1-\zeta}\right) - \frac{1}{2}\right), \quad (2.26)$$

$$\sigma_{\nu,mr}(\gamma) = \frac{\alpha_f \sigma_T}{10\pi\nu}\left\{\zeta\left[20 - 6\frac{1+\zeta^4}{(1+\zeta^2)^2}\right] + ln\left(\frac{1+\zeta}{1-\zeta}\right)\times \left[6(1+\zeta^2) - \frac{7(1-\zeta^4)^2 + 3(1-\zeta^2)^4}{2(1+\zeta^2)^3}\right]\right\}, \quad (2.27)$$

where α_f is the fine-structure constant and $\zeta = 1 - (h\nu)/(\gamma m_e c^2)$.

The interaction cross-section is assumed to be zero for non-relativistic electrons because the contribution from such low-energy interactions is negligible in the frequency ranges modelled.

The bremsstrahlung cooling rate, $\dot{\gamma}_B$, used in equation 2.6, is given by

$$-\dot{\gamma}_B = \frac{h}{\sigma_T l m_e c}[\tau_{T,mr}\int \nu\sigma_{\nu,mr} d\nu] \quad ;\text{if} \quad \gamma < 2, \quad (2.28)$$

$$-\dot{\gamma}_B = \frac{h}{\sigma_T l m_e c}[(\tau_{T,mr} + 2\tau_{T,ur}) \int \nu \sigma_{\nu,ur} \mathrm{d}\nu] \quad ;\text{if} \quad \gamma \geq 2. \tag{2.29}$$

2.2.3.3 Compton Scattering

Each of the six photon distributions in each cell may undergo Compton and inverse Compton scattering in each timestep. Equation 2.8 is not used directly in this case, however, as there is no equivalent absorption process. We assume instead that the Comptonising region is optically thin ($\tau_\nu \ll 1$) and so equation 2.8 can be simplified to

$$I_\nu = l\epsilon_\nu, \tag{2.30}$$

where l is the distance travelled by the photon. This assumption sets a limit on the size of an individual cell in HEART (see also section 2.1) as each cell must be small enough to contain only an optically thin part of the corona[8]. In the case of Compton scattering κ_ν is not needed, and

$$I_{\nu_1} = w \int_{\nu_{0,min}}^{\nu_{0,max}} \int_{\gamma_{min}}^{\gamma_{max}} n_\gamma x F_C(x) \mathrm{d}\gamma I_{\nu_0} \frac{\mathrm{d}\nu_0}{\nu_0}, \tag{2.31}$$

$$I'_{\nu_0} = I_{\nu_0} - w \int_{\nu_{1,min}}^{\nu_{1,max}} \int_{\gamma_{min}}^{\gamma_{max}} n_\gamma x F_C(x) \mathrm{d}\gamma I_{\nu_0} \frac{\mathrm{d}\nu_1}{\nu_1} \tag{2.32}$$

where the emission coefficient is

$$\epsilon_{\nu_1} = \int_{\nu_{0,min}}^{\nu_{0,max}} \int_{\gamma_{min}}^{\gamma_{max}} n_\gamma x F_C(x) \mathrm{d}\gamma I_{\nu_0} \frac{\mathrm{d}\nu_0}{\nu_0}. \tag{2.33}$$

Equation 2.31 is the distribution of scattered photons which is added to the photon distributions, and equation 2.32 describes the removal of photons which have undergone scattering. Here $x = \nu_1/(4\gamma^2\nu_0)$, w is the width of a cell, ν_0 is the frequency of the photon before the scattering event and ν_1 is the frequency

[8]It thereby also limits the total optical depth HEART can model as increasing the number of cells modelled increases the run-time of the code. This is discussed further in section 4.4

afterwards. The photon redistribution function, $xF_C(x)$, is calculated for three different cases

1. mildly relativistic electrons ($\gamma < 10$) interacting with high-energy photons ($k > 10^{-2}$),
2. mildly relativistic electrons ($\gamma < 10$) interacting with low energy photons ($k \leq 10^{-2}$) and
3. relativistic electrons ($\gamma \geq 10$),

where $k = \gamma h\nu_0/(m_e c^2)$. The equations for the photon redistribution function in each case can be found in Appendix A.2. Note here that the anisotropy of Compton scattering is not taken into account. This is discussed further in section 3.5.

The Compton cooling rate, $\dot{\gamma}_C$, used in equation 2.6, is given by (Blumenthal & Gould, 1970)

$$-\dot{\gamma}_C = \frac{4\pi}{m_e c^2} \int\int \frac{\nu_1 - \nu_0}{\nu_1} I_{\nu_0} x F_C(x) \frac{\mathrm{d}\nu_0}{\nu_0} \mathrm{d}\nu_1. \tag{2.34}$$

2.2.3.4 Cooling electrons

These radiative processes contribute to cooling the electrons, so in the absence of heating effects for the electrons, the kinetic equation eventually causes a pile-up of electrons in the bin with the lowest energy. To avoid the numerical problems with this effect, electrons are artificially removed from the lowest energy bin. Whenever the number of electrons in the lowest energy bin exceeds the number in the adjacent energy bin, it is set equal to that in the adjacent energy bin. This is relevant only for evolving electron distributions, which are not generally described by a purely thermal or power-law distribution.

2.2.4 Seed photons

I have described the emission and scattering processes occurring in each cell of the corona, irrespective of geometry and surroundings. In the case of a corona in the

vicinity of an accretion disc, however, there is an external source of seed photons, and this is also modelled in HEART. Possible situations include a single or multi-colour blackbody spectrum at a given maximum temperature injected upwards/downwards from an accretion disc surrounded by a corona or injected sideways into a geometrically thick corona surrounded by a thin disc, similar to the ADAF described in section 1.1.

The Planck formula is used to model the blackbody spectrum,

$$I_\nu = \frac{2h\nu^3}{c^2} \frac{1}{\exp(\frac{h\nu}{kT_{BB}}) - 1}, \tag{2.35}$$

where T_{BB} is the blackbody temperature. In order to simulate a multicolour blackbody spectrum from the disc, a superposition of blackbody spectra of temperatures $T_{BB,r}$ is modelled, where T_{BB} varies with disc radius, r, according to (Frank et al., 1992)

$$T_{BB,r} = \frac{t_{max}}{0.488} \times \left[\frac{r_{in}}{r}\right]^{\frac{3}{4}} \times \left[1 - \sqrt{\frac{r_{in}}{r}}\right]^{\frac{1}{4}}, \tag{2.36}$$

where t_{max} is the temperature of the disc at radius r_{in}, which is the inner disc radius closest to the accreting compact object. The disc is hottest at r_{in} and the temperature decreases with increasing radius. This is modelled in HEART by injecting different blackbody distributions into the injection cells depending on their location relative to the centre of the disc. In cases where the disc temperature varies significantly over the width of a cell, the temperature is discretised further.

Emission from any part of the disc not covered by the corona contributes directly to the total flux emitted by the system. In this case, the flux emitted by the uncovered part of the disc is adjusted according to the system's inclination angle. In real systems, some of the uncovered disc radiation will enter the corona, but as only the six directions parallel to the sides of a cell are modelled here, uncovered disc photons cannot enter the corona. This limits the geometries HEART can model in a physical way, see section 6.2 for a discussion of this.

2.3 Running the code

I have given a detailed description of the physical processes modelled in HEART as created by Collins (2004), including the equations used to model the radiative transfer and the expressions for the terms in the kinetic equation (equation 2.2) governing the electron evolution. I now outline the parameters and settings files which are the user input to HEART, and which determine some of the parameters in the equations in this chapter as well as more technical details like the runtime of the code.

The parameters file is where the physical input parameters are given, for example the parameters of the thermal and power-law electron distributions to be injected into cells and the temperature of the disc. Table 2.1 lists these parameters and gives some typical example values. The parameter 'model' refers to the geometry of the system. Here the external corona model is used, which is a hemisphere over a circular multi-colour disc (as described in equations 2.35 and 2.36). Other models include ECorona_SCD, which is the same as ECorona but with a blackbody disc (a single colour disc), ICorona, which is the internal corona model where the corona is a hemisphere at the centre and the accretion disc surrounds it, Cube where the corona is a cube and other similar geometries. Any geometry can be modelled, but these geometries, which are described in more detail in Collins (2004), have been implemented as parameters for ease of use.

nu_min and nu_max are the minimum and maximum photon frequencies modelled respectively, and similarly gamma_min and gamma_max are the minimum and maximum Lorentz factors of the modelled electrons (see equation 2.2). w is the width of the corona, D is the distance of the observer to the accreting object and M_bh is the mass of the accreting compact object. N_H is the galactic absorption due to neutral hydrogen and B the magnetic field strength, neither of which are used in the remainder of this thesis.

n_e and kT_e are the thermal electron parameters n_e and kT_e as defined in equation 2.3 and Q_e and q are the power-law electron parameters n_e and q as defined

HEART parameters	example
model	ECorona
nu_min (Hz)	1×10^{16}
nu_max (Hz)	1×10^{22}
gamma_min	1
gamma_max	1000.0
w (m)	3×10^{6}
D (pc)	2000
M_bh ($M_\odot$)	5.0
N_H (cm^{-2})	0
B (T)	0
n_e (m^{-3})	2×10^{22}
equivalent τ_{th}	2
kT_e (keV)	50.0
Q_e (m^{-3})	0.12×10^{22}
equivalent τ_p	0.12
q	3.0
t_inj	0.0
t_esc t_cross^{-1}	0.0
kT_max (keV)	0.1
r_min (Schwarzschild radii)	3
r_max (Schwarzschild radii)	100
i (°)	65.0

Table 2.1: The input parameters to HEART.

in equation 2.4. The optical depth of the thermal and power-law distributions are also given, τ_{th} and τ_p respectively, though they are not input parameters to HEART. The time dependence of n_e and Q_e is taken care of by converting to m^{-3} t_cross^{-1} when electron evolution is modelled according to the kinetic equation (2.2). t_inj and t_esc set the injection rate and escape time of the electrons, respectively. Setting these to 0 gives continuous injection throughout the run and no escape. kT_max converted to Kelvin and r_min are t_{max} and r_{in} in equation 2.36 respectively, i.e. kT_max is the maximum temperature at the inner disc radius closest to the accreting object, r_min, and r_max is the radius of the outermost part of the disc. The inclination angle i is only relevant if part of the disc is exposed in which case the effective area is calculated for directly observed disc emission.

More technical values like the run-time, number of cells and number of bins to

discretise the electron and photon distributions into are given by the settings. A full list of settings with examples is given in table 2.2. sim determines whether to run a simulation for a given number of timesteps, sim = Normal, or whether to terminate after reaching equilibrium, sim = Eq (see section 4.1). If sim = Normal, the number of timesteps is set by t_max given in units t_units. Here t_units is t_cross, the time taken for light to cross the diameter of the corona, and the number of cells along the diameter of the corona is R_cells = 24. This simulation will run for the number of timesteps taken for light to cross the width of the corona 10 times, i.e. 240 timesteps in this example. If sim = Eq, HEART will terminate after equilibrium is reached or after 240 timesteps, whichever is shorter. Equilibrium is reached when the spectrum changes by less than a specified percentage, usually around 1%, in each energy bin between two timesteps. See section 4.1 for a more detailed discussion of equilibrium conditions.

R_cells = 24 creates a 3604 cell corona in the ECorona model. It is important to ensure that R_cells is sufficiently large for the seed photons to be binned finely enough to approximate a disc where temperature changes continuously with radius, as well as the optical depth in each cell being $\ll 1$ (see section 2.2.3.3). R_electrons and R_photons sets the number of energy bins for the discretised electron and photon distributions respectively, and if no_bremsstrahlung, no_kinetic_equation and/or no_compton are included the relevant process is disabled. Bremsstrahlung and the calculation of the kinetic equation are disabled throughout unless otherwise stated. It is possible to disable any physical process[9].

The form of the output is also set by the user, but I do not go into detail here. Throughout the following work output is usually obtained by writing the numerical data to a file[10] rather than using the plots produced by HEART as described in Collins (2004). This is a more flexible form of the output, as the data can then be exported to plotting programs such as Matlab and manipulated as necessary.

[9]This also applies to processes added later in this work.

[10]Output to a file rather than directly to plots is a feature I added. Any changes mentioned in this chapter that I have made are noted in footnotes (there are four), the entirety of the rest of the chapter is a description of HEART as discussed in Collins (2004).

HEART settings	example
sim	Normal
t_max	10
t_units	t_cross
R_cells	24
R_electrons	96
R_photons	96
physical processes	no_bremsstrahlung
	no_kinetic_equation
	no_compton

Table 2.2: The HEART settings.

I refer to the parameters described above in later chapters as I add to them with additional features in chapter 3, compare HEART to the analytic model of Titarchuk (1994) and fit data in chapter 4 and use HEART for variability studies in chapter 5. Unless otherwise stated, the example values for the parameters and settings given in tables 2.1 and 2.2 are used throughout, except for the run-time which is determined as discussed in section 4.1. Bremsstrahlung and synchrotron radiation are disabled throughout, and electron evolution, i.e. the calculation of the kinetic equation, is only modelled in section 3.4 and chapter 5.

Chapter 3

Further developments to HEART

Although the HEART code described in section 2 aims at modelling fairly complete physical situations self-consistently in a flexible setting, a few important processes are lacking[1]. One process observed in X-ray binary and AGN data, and not previously modelled by HEART, is reflection and reprocessing of scattered photons in the disc. Including this process can change the spectral index of the Comptonised component of the spectrum, as for example in Seyfert galaxies, where the accepted typical spectral index changed from 0.7 to 0.9 when reflection was added (Pounds et al., 1990).

Another feature which allows for more physical simulations is the capability of injecting inhomogeneous electron distributions in the corona. Previously electron distributions in each cell evolved independently and could therefore evolve into an overall inhomogeneous corona, but it was not possible to model an inhomogeneous corona initially, or to inject an inhomogeneous corona in each timestep. This allows, for example, coronae with hollows or coronae which gradually thin rather than reach a sudden outer boundary to be modelled.

One of the major weaknesses of HEART in its current form is the lack of treat-

[1]On testing, it is found that HEART does not achieve this aim. See chapter 6 for a discussion.

ment of anisotropic Compton scattering. The probability of undergoing scatter, the energy transfer and the direction of the scattered photon all depend on the initial photon and electron trajectory. Including a fully anisotropic treatment of inverse Compton scattering would require too significant a reworking of HEART to be immediately feasible. However, here I describe the implementation of an approximation to an anisotropic treatment of Compton scattering. I discuss these developments in this chapter.

3.1 Reflection and Reprocessing

The contribution from reflection of Comptonised photons on cold matter (usually assumed to be the disc) to the X-ray spectrum from AGN is suggested in Lightman & White (1988) and Guilbert & Rees (1988). This is investigated further in George & Fabian (1991), where a Monte Carlo code is developed to compare the effects of reflection to observed spectra from AGN and X-ray binaries. Reflection from the disc has subsequently been much discussed in the literature, for example Done & Nayakshin (2001) discuss the reflected component in the context of luminous magnetic flares illuminating the disc, and fit their model to data from Cyg X-1 and Nova Muscae in the LHS. Including the reflected component changes the underlying physical model, as in the example of Seyfert galaxies given above, and the reflected component is now often included when fitting observational data, so it is an important inclusion in any spectral model for AGN and X-ray binaries.

It is not known exactly where the reflection occurs, but one possibility is that scattered photons are being reflected at the surface of the accretion disc. For example Haardt & Maraschi (1991, 1993) model a two-phase geometry (a disc and corona, each of slab geometry) where the two phases are coupled and reflection and reprocessing in the disc are modelled (see section 1.5). Certainly if such a disc is present then reflection and reprocessing in the disc will occur, so this process should be included in HEART for completeness. We can then learn more about the geometry of these systems and, for example, whether there is additional reflection occurring

elsewhere, external to the system, which cannot be explained by reflection in the accretion disc.

Reflection and reprocessing in the disc are caused by the fraction of scattered photons travelling towards the disc where they are either reflected or absorbed depending on the photon energy. High energy photons, where Klein-Nishina effects are important ($h\nu \gg m_e c^2$), have a low interaction probability with the disc matter and therefore travel far into the disc before being absorbed and contributing to the heating of the disc, i.e. they are reprocessed into thermal disc emission. Low energy photons also contribute to heating the disc as they are absorbed effectively by the matter in the disc. The rest of the photons, where the scattering opacity is greater than the absorption opacity, create the characteristic reflected component at $\sim 10 - 300$ keV, as they undergo Compton scattering near the surface of the disc and escape with a lower energy than they entered with (Lightman & White, 1988).

An iron line at 6.4 keV is usually observed in addition to the reflection component, and information about the geometry of the system can be deduced from the width and strength of this line. Firstly, the Fe Kα line implies the presence of cold matter, where neutral iron can exist. Secondly, its strength gives an indication of the abundance of neutral iron in the system, which is usually compared to the solar abundance. The width of the Fe Kα line is also important, as relativistic smearing occurs near the black hole, widening the line. Thus it is an indicator of how close to the black hole the cold matter, usually the accretion disc, extends. In an ADAF model, a narrower Fe Kα line is expected, as the disc truncates far from the disc, but in the geometry modelled here the disc extends into its innermost stable orbit, and so a wider Fe Kα line is expected. The normalisation of the reflection component should also decrease with the smaller disc of the ADAF model. The iron line, as well as the reflected component may, however, be distorted by Comptonisation of the photons as they traverse the corona (see section 3.3.1). A treatment of the iron line is, however, too complex to include in HEART at this stage as the composition of the disc is not modelled.

In HEART the reflected spectrum is calculated in every timestep in every cell neighbouring the disc (in every injection cell). The reflected photons are then added to the disc emission in the following timestep and the temperature of the disc can be modified locally to account for any absorbed and reprocessed photons. The disc temperature is not adjusted due to absorbed photons in the work presented here, however, as the structure of HEART is unsuitable for modelling the coupling of the disc and corona. This is discussed further in chapter 6.

3.1.1 Reflection in HEART

In HEART, only photons travelling downwards in the injection cells need be considered for reflection as only 6 directions are modelled, and any reflected photons are added in the upwards direction with the disc emission. This is a massive approximation as reflected spectra have a distribution of directions depending on the photon energy and angle of incidence (Magdziarz & Zdziarski, 1995). Reflection is, for example, more efficient at grazing angles as these photons penetrate less deeply into the disc (Matt et al., 1991). The current form of HEART is, however, unsuitable for including these directional effects as only six photon directions are modelled. It is also unnecessary to model the directional dependence of the reflected distribution while the anisotropy of Compton scattering is not treated. HEART cannot produce different spectra for different viewing angles anyway, and reflected photons may undergo scattering in the corona and may consequently change direction again. Hence reflection is only calculated in injection cells for the downward photon distributions.

I use the analytic treatment of Lightman & White (1988) (which agrees well with Monte Carlo simulations) to determine the reflected spectrum in each injection cell. They model the reflection of monoenergetic photons incident on a semi-infinite, plane-parallel medium of cold electrons ($\approx$ 10 eV). As the disc is not modelled directly in HEART, the assumptions relating to the disc simply add to the assumptions of HEART. These are reasonable assumptions for a cold, optically thick disc. HEART models a distribution of photons over energy, but as the photon distribution

is discretised we actually model several monoenergetic photon distributions, one for each energy bin.

The reflected spectrum is given by (Lightman & White, 1988),

$$S_{out} = \int_x^{x_0} G(x, x_0) S_{in}(x_0) \mathrm{d}x_0, \tag{3.1}$$

where S_{out} is the reflected spectrum, S_{in} is the spectrum of photons incident on the disc, $x = \frac{h\nu}{m_e c^2}$ and the Green's function, $G(x, x_0)$, is the probability per unit energy that a photon incident on the disc of energy x_0 is reflected at energy x. Consider a fixed x, the energy at which a photon is reflected. All incident photons (of energies x_0) from $x = x_0$ up to x equal to the greatest energy modelled make contributions to the reflected spectrum at x, and these contributions are summed. We require $x_0 > x$, because photons are not allowed to gain energy from the disc (only Compton scattering, not inverse Compton scattering, is considered in the disc).

Equation 3.1 can be solved quite easily in the case where $h\nu \lesssim 15$ keV, as it can be assumed that Compton scattering is completely elastic (electron recoil can be neglected). It can then be shown that (Lightman & White, 1988),

$$S_{out}(x) = \frac{1 - \epsilon^{\frac{1}{2}}}{1 + \epsilon^{\frac{1}{2}}} S_{in}(x), \tag{3.2}$$

where $\epsilon \equiv \kappa_\nu / (\kappa_\nu + \kappa_{es})$, κ_ν is the free-free opacity and $\kappa_{es} = 0.4$ cm^{2}g^{-1} is the Thomson scattering opacity. κ_ν is approximated to $\kappa_\nu = C \kappa_{es} x^{-3}$ where $C = 10^{-5}$ for $h\nu > 10$ keV, assuming cosmic abundance material. For $h\nu \leq 10$ keV, κ_ν can be calculated using Table 2 in Morrison & McCammon (1983) of the cross-section of hydrogen at different energies between 0.03 and 10.0 keV. The opacity is then given by (Rybicki & Lightman, 1979),

$$\kappa_\nu = \frac{n \sigma_\nu}{\rho}, \tag{3.3}$$

where ρ is the mass density and so n/ρ is Avogadro's number divided by the molecular weight of hydrogen.

For $h\nu > 15$ keV elastic Compton scattering is no longer a valid assumption and it is instead assumed that the Green's function can be written as (Lightman & White, 1988),

$$G(x, x_0) \approx W(x, x_0) G_{es}(x, x_0), \tag{3.4}$$

where

$$W(x, x_0) = exp\left[C\left(\frac{1}{4{x_0}^4} - \frac{1}{4x^4}\right)\right]. \tag{3.5}$$

The constant C is defined as above ($C = 10^{-5}$ for $h\nu > 10$ keV) and $G_{es}(x, x_0)$ is calculated according to White et al. (1988), where Monte Carlo simulations are used to approximate the Green's function analytically. Using the conversion $G(x, x_0) = x^{-2} G(\Delta y, y_0)$, where $y = 1/x$ and $\Delta y \equiv y - y_0$, we have

$$G(\Delta y, y_0) = \begin{cases} B[(y_0 + 2)/(y_0 + \Delta y)]^{\beta}, & \text{if} \quad \Delta y < 2 \\ A(\Delta y)^{-3/2} (\Delta y_c / \Delta y)^{\alpha}, & \text{if} \quad 2 < \Delta y < \Delta y_c \\ A(\Delta y)^{-3/2}, & \text{if} \quad \Delta y_c < \Delta y, \end{cases} \tag{3.6}$$

where $\Delta y_c = 10^3 - y_0$ and

$$
\begin{aligned}
A &= 0.56 + 1.12y_0^{-0.785} - 0.34y_0^{-1.04}, \\
\alpha &= -0.30y_0^{-0.51} + 0.06y_0^{-0.824}, \\
\beta &= 0.37 - 1.0y_0^{0.85}, \\
B(A,\alpha,\beta) &= \frac{1 - \frac{U1}{(\Delta y_c)^{1/2}}}{D}, \qquad \text{if} \qquad \alpha \neq -\frac{1}{2} \\
B(A,\alpha,\beta) &= \frac{1 - \frac{U2}{(\Delta y_c)^{1/2}}}{D}, \qquad \text{if} \qquad \alpha = -\frac{1}{2}, \\
U1 &= A\{2 + \frac{[(\frac{\Delta y_c}{2})^{(\frac{1}{2}+\alpha)} - 1]}{(\frac{1}{2}+\alpha)}\}, \\
U2 &= A[2 + \ln\frac{\Delta y_c}{2}], \\
D &= \frac{y_0^{1-\beta}(y_0+2)^{\beta}[(1+\frac{2}{y_0})^{(1-\beta)} - 1]}{1-\beta}.
\end{aligned} \tag{3.7}
$$

Integrating equation 3.1 then gives the reflected spectrum.

In HEART, S_{in} in equation 3.1 is the photon distribution travelling in the downward direction in each injection cell in each energy bin, while S_{out} is the reflected distribution added in the upward direction in the following timestep. For energies $h\nu > 15$ keV the Green's function (equation 3.4) is calculated for every energy bin combination where $x_0 > x$. Equation 3.1 is then integrated numerically using the existing discretisation of the photon distribution (see section 2.1), and a characteristic reflected bump between $\sim$ 10 - 300 keV is created. This is demonstrated in figure 3.1 in section 3.1.3.

3.1.2 Absorption in the disc

This is not modelled in a physical way in HEART and the inclusion of the following implementation causes great problems in HEART, as is discussed in chapter 6. The structure upon which HEART is built does not allow for a better implementation, however, so it is described here, but not used throughout this work.

The photons incident on the disc which are not reflected, are absorbed and

reprocessed into thermal disc emission in real systems. Previously the disc emission was calculated only at the start of the code according to a fixed disc temperature, and the same distribution was added in every timestep. Including absorption in the disc, however, means that the disc emission may change locally between timesteps, so it is not sufficient to calculate it only once at the start. To prevent the code from running much slower the disc emission is only recalculated if enough energy is absorbed to change the local disc temperature noticeably, but it is possible to recalculate it in every timestep.

The energy absorbed by the disc is the total energy incident on the disc minus the total energy reflected away from the disc, and the new blackbody temperature, T_{rep}, is

$$T_{rep} = \left[\frac{(\text{absorbed flux} + \sigma T^4)}{\sigma}\right]^{\frac{1}{4}}, \tag{3.8}$$

where T is the temperature of the disc as described in equation 2.36 (due to gravitational dissipation and friction) and σ is the Stefan-Boltzmann constant.

In order to keep track of the local temperature of the disc I create a layer of disc cells on the surface of the disc with links to their neighbouring corona cells. The initial temperature of each disc cell is given by equation 2.36 using the radius of the midpoint of each cell. It is then possible to change the temperature of a single disc cell, i.e. a single discretised area of the disc, according to the photons absorbed by that area of the disc. The temperature of each disc cell then determines the disc emission into its neighbouring corona cell in the following timestep.

Electron transport is not modelled in HEART, and thus no consideration is given to any coupling between the electrons in the corona and the disc. As mentioned previously, modelling absorption in the disc as described here, and thus the coupling between the corona and the disc, leads to considerable problems in HEART. It is disabled throughout this work, including the simple tests in chapter 4 and the dynamic runs in chapter 5, even when the reflected component is modelled. The effect of including absorption, and thereby heating of the disc, to the results in

chapters 4 and 5 is discussed in section 6.1, where the problems this causes in HEART are also discussed.

3.1.3 Demonstrating the reflection component in HEART

Reflection is more easily demonstrated in the HSS of X-ray binaries than the LHS when using the ECorona model (a hemispherical corona of covering fraction 1) since the reflected photons are subject to the same scattering probabilities as the disc photons. In the LHS the photons undergo enough scattering events (the average number of scattering events $\sim \tau^2 \gg 1$) for the output spectrum to become independent of the input spectrum (Sunyaev & Titarchuk, 1985). Thus including reflection makes little difference to the output spectrum. This is discussed further in section 4.3.1 where HEART is used to fit data of Cyg X-1 in the LHS.

A typical HSS is appropriate to demonstrate the reflected component in HEART. I use similar parameters to the best fit of HEART to data from Cyg X-1 in the HSS from section 4.3.2, with a purely power-law, static electron energy distribution (n_e = 0 m^{-3}) with parameters Q_e = 0.12×10^{22} and q = 4.1, equivalent to an optical depth of $\tau_p = 0.12$. Thus evolution of the electron distribution is not modelled and the calculation of the kinetic equation is disabled. The disc temperature is kT_max = 0.4 keV and the disc extends to the outer edge of the corona. The rest of the parameters are listed in table 2.1, where they are also explained.

In figure 3.1 the output spectra from HEART with and without reflection are compared, and the reflection component as it leaves the disc, before traversing the corona, is also shown separately. Reprocessing of absorbed photons to thermal radiation in the disc is not modelled. The reflected component shows the expected characteristic bump between $\sim 10 - 300$ keV, and the difference it makes to the output spectrum in this energy range is small, but evident. With an optical depth of 0.12 not many photons are expected to scatter towards the disc and reflect so a small contribution from the reflected component is expected. Also, the reflected component shown in figure 3.1 should not change much after traversing the corona.

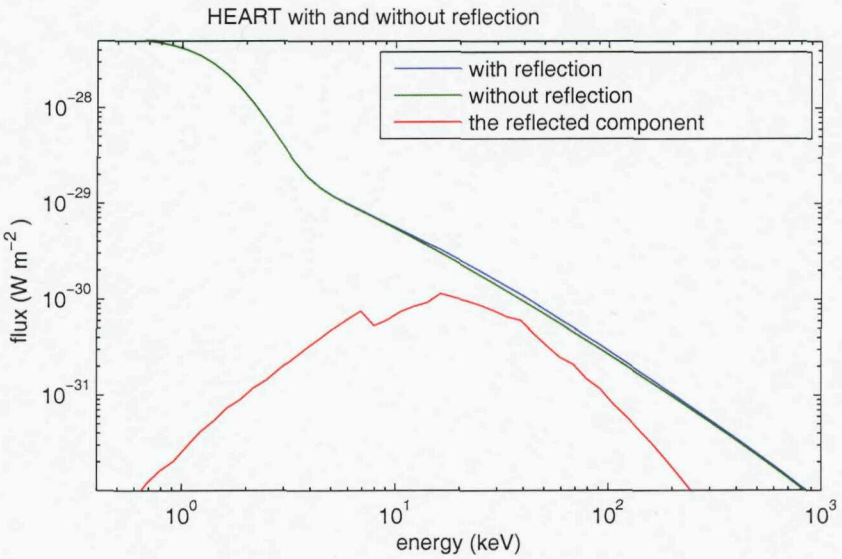

Figure 3.1: HEART with and without reflection implemented. Reprocessing of absorbed photons into thermal disc emission is not modelled. The reflected component, as it leaves the disc before traversing the corona, is also shown separately.

The reflection component is used in section 4.3.2 to fit data from Cyg X-1 in the HSS.

3.2 Full reflection

Now that the photons incident on the disc are being treated more accurately with reflection (previously they were simply deleted from the model, now only the absorbed photons are deleted) it is worth considering what happens to downward travelling photons where there is no disc. There is no necessity for the disc to extend out to the edges of the corona. For example, we may wish to model a sphere with central injection at a point rather than the extended injection of a disc. This is done in section 4.2 to approximate the analytic model by Titarchuk (1994).

In order to determine how to treat photons escaping the corona in a downward direction (those not incident on a disc), consider the fact that only half the corona is modelled and it is assumed to be symmetric. (This decreases the run-time of the

code. In the case of a sphere for example, a hemisphere is modelled, see section 2.1.) Consider a photon, ν_m, leaving the modelled half of the corona in the downwards direction, where there is no disc separating the modelled half from the unmodelled half. By symmetry there is a photon, ν_{um}, in the unmodelled half of the corona with the same energy as photon ν_m, and which is travelling upwards and escaping the unmodelled corona. It will enter the modelled half of the corona at the same time as photon ν_m escapes the modelled half and enters the unmodelled half. To simulate this I simply reflect the photon escaping downwards, photon ν_m, and add it to the upwards distribution in the next timestep without changing its energy. This is illustrated in figure 3.2. I refer to this as full reflection hereafter.

Full reflection causes a greater scattering component in the spectrum (for the same optical depth) than the version where downward photons were simply deleted at the corona boundary. Not only does it cause more scattering events in general as the average photon escape time is increased, but this applies mostly to photons which have already gained energy due to scattering. Photons must have undergone at least one scattering event to be returning to the disc, i.e. travelling downwards in the ECorona geometry considered here. These then have the chance to scatter again and are eventually added to the spectrum rather than lost.

In figures 3.3 and 3.4 I compare HEART with and without full reflection (as for all physical processes in HEART it is possible to disable full reflection) to the analytic model by Titarchuk (1994) as it appears in XSPEC version 11.3.2.t as model *compTT*. This is a widely used and tested model, but is limited to modelling only Compton scattering with no electron evolution in a homogeneous, spherical or slab geometry. Within these limitations, HEART should agree with *compTT*. I approximate the central injection of photons in a sphere used in *compTT* by modelling a very small accretion disc in HEART. The maximum disc temperature is 0.1 keV, the electron distribution is purely thermal at 50 keV and optical depths of $\tau_{th} = 0.5$ and 1.5, corresponding to n_e $= 0.5 \times 10^{22}$ m^{-3} and 1.5×10^{22} m^{-3}, in figures 3.3 and 3.4 respectively are considered. For a full list of parameters see

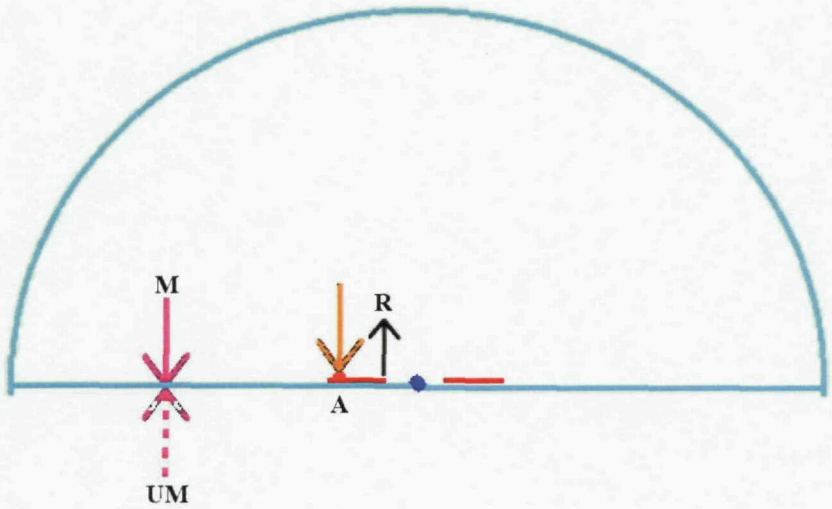

Figure 3.2: A schematic demonstrating reflection and absorption in the disc and full reflection. Seed photons are emitted from the red disc and interact with electrons in the corona, which is modelled within the volume delineated by the cyan line. The black hole is the blue dot at the centre of the red disc. Photons may scatter in the corona and return to the disc, and two downwards arrows in this schematic represent two such photons. The orange one, which is incident on the disc, may be absorbed or reflected. Absorption is demonstrated by the red dot on the disc labelled A and is not modelled in HEART. These photons are lost from the system. Reflection is demonstrated by the black arrow labelled R. In HEART a distribution of photons is incident on the disc, only some of which are reflected, hence the reflected arrow is smaller than the incident arrow. The energy distribution of the reflected photons has also changed.
The pink arrows demonstrate full reflection. The full, downward arrow (labelled M and referred to as ν_m in the text) is leaving the modelled corona as it is travelling downwards, but is not incident on the disc. By symmetry, the broken, pink arrow (labelled UM and referred to as ν_{um} in the text) exists. The photon represented by the broken pink arrow will enter the modelled corona as the photon represented by the full pink arrow leaves the modelled corona. This is modelled by reflecting the photon represented by the full pink arrow in the lower modelled corona boundary, i.e. in the lower cyan line.

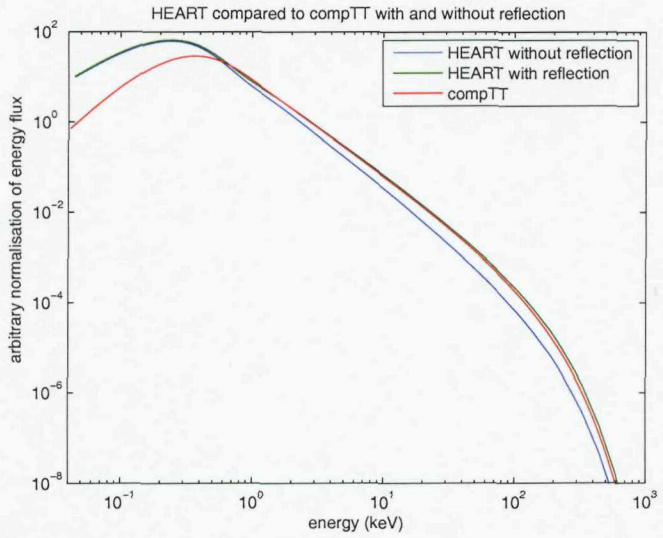

Figure 3.3: HEART with and without full reflection compared to *compTT*. The maximum disc temperature is 0.1 keV, the electron temperature is 50 keV and the optical depth is 0.5. The electron distribution is purely thermal and does not evolve, i.e. the calculation of the kinetic equation is disabled.

table 2.1 in section 2.3. The evolution of the electron distribution is not modelled and the calculation of the kinetic equation is disabled.

It is evident that including full reflection in HEART agrees better with *compTT* in both figures. The spectral slopes of *compTT* and HEART at high photon energies with full reflection included are consistent with each other, whereas HEART without full reflection underestimates the effect of inverse Compton scattering in this geometry. The disc component in HEART is not quite consistent with *compTT*, but the disc in HEART is a slightly extended multicolour disc, whereas in *compTT* photons with a blackbody spectrum are injected from a central point source. Further comparisons between HEART and *compTT* are made in section 4.2.

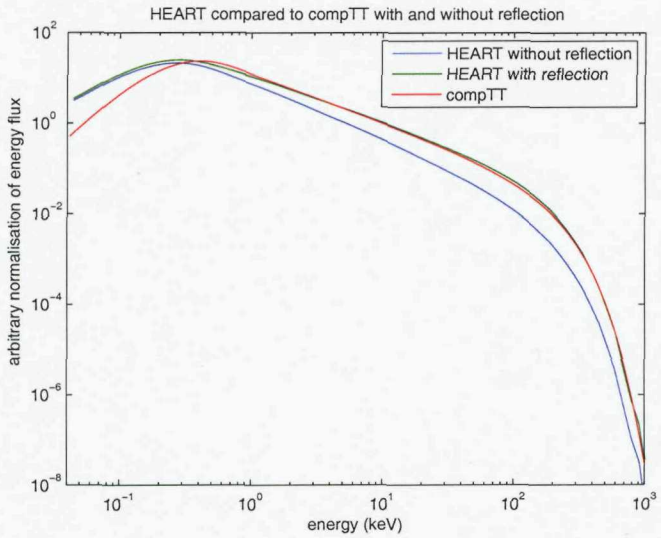

Figure 3.4: HEART with and without full reflection compared to *compTT*. The maximum disc temperature is 0.1 keV, the electron temperature is 50 keV and the optical depth is 1.5. The electron distribution is purely thermal and does not evolve, i.e. the calculation of the kinetic equation is disabled.

3.3 Inhomogeneous electron distributions

Previously in HEART it was only possible to inject the same electron distribution into each cell[2], specified by the global parameters temperature, power-law index and thermal and power-law density (see section 2.3). Due to the discretised representation of the electron distributions in HEART, any electron distribution may be stored, and the electron distributions, which evolve independently in each cell, may previously have evolved into an overall inhomogeneous corona. The parameters used to inject and/or remove electrons, however, were global for all cells.

Thus the structure of HEART is compatible with modelling inhomogeneous coronae, a feature few other models share. Most other models, for example those of Sunyaev & Titarchuk (1980) and Titarchuk (1994) (see section 1.5) model only static, homogeneous coronae, though Poutanen & Svensson (1996) and Stern et al. (1995b)

[2]Electrons are injected into the corona at the start of a simulation. Depending on whether the calculation of the kinetic equation is enabled, the electron distribution may then remain constant, or it may evolve, in which case a time-dependent injection rate is used (as discussed in section 2.2.1).

model some inhomogeneous situations. As this is a particular strength of HEART, and as inhomogeneous coronae are instinctively more physical, it is a feature worth extending to its full capability.

Any inhomogeneous geometry can be modelled within the limitations of the cell structure of HEART, and a simple example is given here. One situation which is more physical than a homogeneous corona with a sudden outer boundary is a corona which gradually thins, or a corona which cools with increasing radius. These geometries can be modelled by decreasing the electron density and temperature respectively with increasing radius[3]. I add the possibility of varying the injected electron distribution as a function of position inside the modelled region according to

$$\text{individual cell parameter} = \text{global cell parameter} \times \left[\frac{\text{scaling factor}}{\text{radius}}\right]^{\alpha}, \quad (3.9)$$

where the scaling factor and index are chosen to give the desired variation of the parameter with radius. Both the density of the thermal and power-law distributions can be varied in this way, as well as the temperature of the thermal distribution and the index of the power-law distribution, and different scaling factors and powers can be given for each. Thus a static, inhomogeneous corona can be modelled, or if electron evolution is modelled, then $Q(\gamma)$, the source function in the kinetic equation (equation 2.2) describing the electron evolution, can change as a function of radius. This enables the modelling of, for example, increased heating of the electrons with decreasing radius.

Rather than using global parameters describing each of the four electron parameters, the four electron parameters are now stored separately in every cell and

[3]This implementation would be more flexible if the electron parameters varied with x, y and z rather than the radius, where x, y and z are a Cartesian coordinate system centred on the black hole with the disc on the z=0 plane. The example given here is easily extendible to such a system, but the simpler example given here, where the electron parameters depend only on radius, illustrates the general principle.

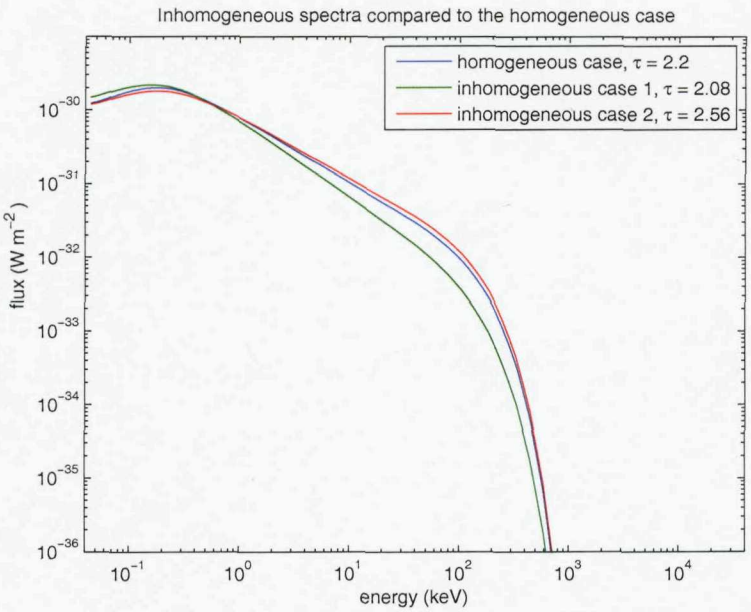

Figure 3.5: A comparison between homogeneous and inhomogeneous coronae in HEART. The parameters for the different cases are given in table 3.1.

can take different values in each cell. The scaling factor and power remain global parameters, however. It is also, of course, possible to disable this feature and return to using only global parameters, as it is possible to disable each of the physical processes (shown in table 2.2).

Spectra created using inhomogeneous and homogeneous coronae are compared in figure 3.5. The homogeneous spectrum is from a typical LHS (the same as in section 4.3.1 where HEART is used to fit Cyg X-1 data in the LHS) with a static, purely thermal electron distribution. Thus the evolution of the electron distribution is not modelled and the calculation of the kinetic equation is disabled. The parameters are listed in table 4.1 (kT_max = 0.08 keV and n_e = 2.2×10^{22} m^{-3}, equivalent to an optical depth, τ_{th}, of 2.2), where they differ from those given in table 2.1. The two inhomogeneous spectra, case 1 and 2, have similar parameters, but n_e varies with radius according to equation 3.9. Two new parameters are introduced, rad_scale_n_e and alpha_n_e, the scaling factor and α in equation 3.9 respectively. These parameters, as well as n_e, are listed in table 3.1.

parameters	homogeneous	inhomogeneous (1)	inhomogeneous (2)
n_e (m^{-3})	2.2×10^{22}	8×10^{22}	8×10^{22}
rad_scale_n_e	n/a	6250	12500
alpha_n_e	n/a	0.3	0.3
equivalent τ_{th}	2.2	2.08	2.56

Table 3.1: The parameters used (where different to those listed in tables 2.1 and 4.1) to model spectra from a homogeneous and two inhomogeneous coronae, referred to in the text as case 1 and case 2.

The settings used are summarised in table 2.2. The corona has a diameter of 3×10^6 m, or 24 cells, so the width of a cell is 125,000 m and the radius of midpoint of the innermost cell is 62,500 m. Hence n_e in the innermost cell is 4.0×10^{22} m^{-3} in case 1 and 4.9×10^{22} m^{-3} in case 2, corresponding to optical depths of 0.33 and 0.41 respectively. Coronae with these parameters throughout would correspond to radial optical depths of $\tau_{th} = 4$ and 4.9 respectively.

The radius of the midpoint of the outermost cell is 1,437,500 m so n_e is 1.6×10^{22} m^{-3} and 1.9×10^{22} m^{-3} in the outermost cell for case 1 and 2 respectively, corresponding to optical depths of 0.13 and 0.16. Coronae with these parameters throughout would correspond to radial optical depths of $\tau_{th} = 1.6$ and 1.9 respectively. To summarise, the optical depth of the corona decreases from 0.33 (0.41) to 0.13 (0.16) in case 1 (case 2), creating a gradually thinning corona. The optical depth of each cell in these two cases in plotted in figure 3.6.

The overall optical depth in all three cases (one homogeneous case and two different inhomogeneous cases with decreasing n_e) is similar, and so it is perhaps not surprising that there is little to distinguish between their spectra in figure 3.5. This would have been a better comparison had the optical depth been the same in all three cases. With such little difference in the spectra, and given the limitations of the model and observational data, however, it seems unlikely that these geometries can be distinguished between based on spectral information. This simple example is encouraging for the applicability of homogeneous models, but also implies that other methods and information may be necessary to determine the geometry of such

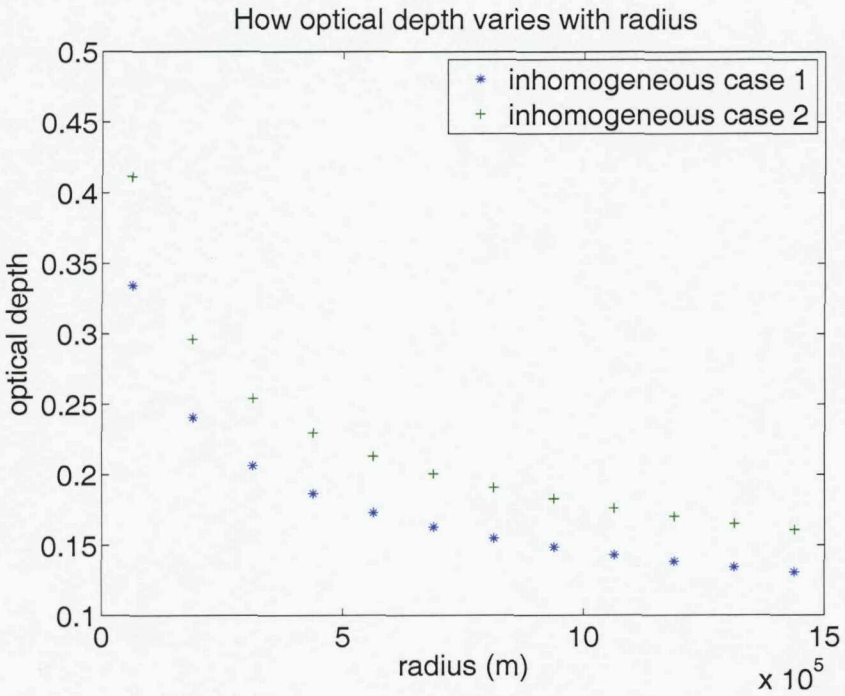

Figure 3.6: A plot of how the optical depth in each cell changes with radius in the two inhomogeneous cases discussed here, with parameters given in table 3.1.

systems.

With this modification in place, however, HEART is more easily adaptable to exploring a wider variety of coronal geometries, not only smooth variations with radius. Although including a great variety of inhomogeneous geometries as parameters becomes messy (see section 2.3 for examples on existing geometries specified as parameters), it is now a trivial matter of changing a few lines of code to model practically any inhomogeneous three-dimensional geometry of the corona. The crucial modification to the HEART code was the capability of each cell to store different electron parameter values.

Another geometry often considered is that of several localised active regions injecting energetic electrons locally, rather than a single homogeneous, spherical corona, see for example Poutanen & Svensson (1996) and Stern et al. (1995b). Such a geometry can be modelled in HEART using a random number generator in each cell, or group of cells, to determine whether an electron distribution should be injected or not. We can then compare a homogeneous geometry with one of active regions, as done above for a radially thinning corona, but in this case we can also compare an inhomogeneous, time-averaged, varying geometry to a homogeneous, static geometry. This enables the evaluation of how appropriate comparisons are between modelled spectra and observed spectra which are integrated over long time-scales. In the case of active regions, there is also information in the temporal variability it causes[4] in addition to the spectral information, which provides more comparison possibilities to observed data.

In figure 3.7 a homogeneous corona (the same as above) is compared to a corona with active regions created randomly in the first timestep. Subsequently their properties remain fixed for the duration of the simulation. The evolution of the electron distribution is not modelled and the calculation of the kinetic equation is disabled, so the electron distribution does not change from the initial configuration. I refer

[4]This is a small preview of chapter 5, where HEART is modified and used to model variability. Details of how lightcurves are created and how the electron distribution is changed between timesteps are given there.

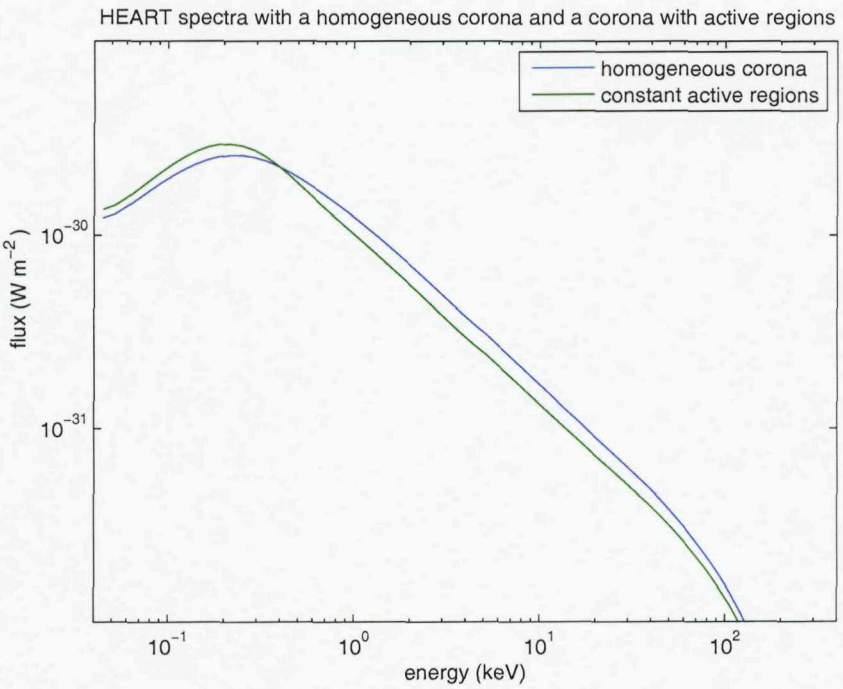

Figure 3.7: The spectra from a homogeneous corona and a corona with random active regions injected initially and then kept constant.

to this geometry as one of constant active regions hereafter. A corona with a 12 cell diameter is used here to model larger active regions, and the parameters used for the active regions are listed in table 3.2. The probability of electron injection into each cell is 0.5, and the electron distribution is purely thermal. Combined with a value of n_e twice that of the homogeneous case this gives a comparable optical depth to the homogeneous case, and the overall spectral shapes are similar. This particular configuration of the corona has a lower optical depth along the normal to the disc (see table 3.2), thus it is not surprising that the disc emission seen at low photon energies contributes more to the inhomogeneous case. Again the homogeneous and inhomogeneous spectra do not differ significantly, so spectral information seems to be insufficient to distinguish between the two geometries. This example is, however, not very different to the homogeneous case, as the covering fraction probably remains 1 and all the photon distributions travel through approximately the same optical depth as the homogeneous case in total. More investigation is required to draw any conclusions.

3.3.1 The reflected component in a corona of active regions

A possible way of distinguishing between a homogeneous corona and one of active regions using only spectral information is by comparing the signature of the reflected component (as described in section 3.1) in the spectra of the two different coronal geometries. When fitting data from Cyg X-1 in the LHS in section 4.3 I find that the reflected component has to be added separately to the HEART model in order to fit the observed data, because the HEART spectrum does not show a reflection feature whereas such a feature is present in the data. This is discussed more fully in section 4.3.1, but, in brief, it is because the seed photons in HEART undergo sufficient scattering events (the average number of scattering events is of order $\tau^2 \gg 1$) to 'forget' their origin. Hence disc photons and reflected photons are no different when they emerge from the corona and contribute to the output spectrum.

One possible reason why the reflection signature is prominent in the data, but

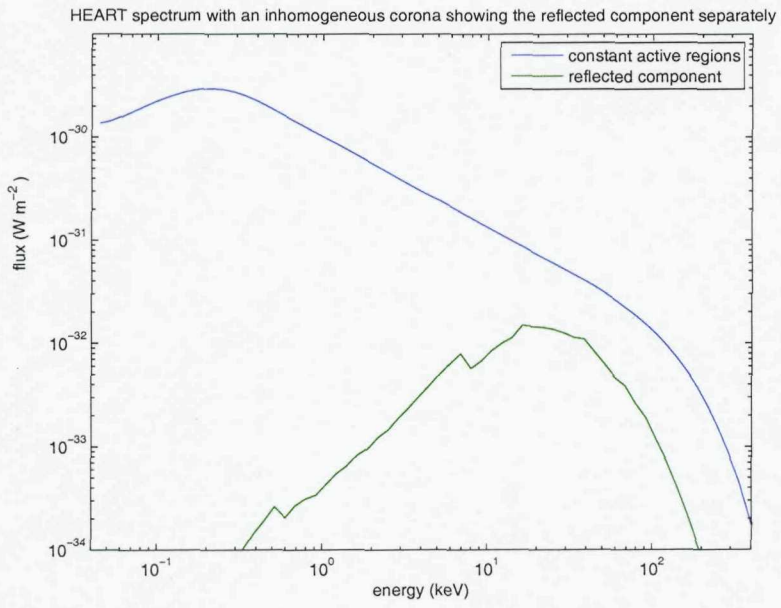

Figure 3.8: The spectrum of a corona made up of random active regions initialised at the start, with the reflected component, as it leaves the disc, shown separately. This reflected component is not added directly to the final output, but is Comptonised as it progresses from the disc, through the corona before it is added to the final output.

not reproduced by HEART, is that HEART models a time-averaged, homogeneous corona, whereas in reality the coronal geometry may be more similar to the active regions geometry described above. In such a geometry some reflected photons may emerge unscattered through a volume of very small optical depth, even though the average optical depth is higher. The reflection signature is, however, no more prominent in the corona of constant active regions than in the homogeneous case presented here, as is shown in figure 3.7, so initially this suggestion has failed.

The reflected component from the corona of constant active regions is shown separately in figure 3.8, as well as the overall spectrum. The reflected component shown is the reflected spectrum as it leaves the disc. It is then Compton scattered as it traverses the corona, before being added to the final output. The part of the spectrum which traverses the corona unscattered is significantly weaker than the overall spectrum in this geometry, and thus is not detectable as a distinct spectral component. Thus the above suggestion, that the unphysical, homogeneous geometry of the corona in HEART prevents the reflected spectrum from being visible, may still be valid, but more investigation than this one example is required.

Petrucci et al. (2001) investigate the effects of Compton scattering on the reflected spectrum in a slab geometry. This is an extreme case, as the covering fraction is 1, but the covering fraction is also 1 in the hemispherical ECorona model of HEART. The authors study the effect of varying the optical depth and temperature of the corona and the inclination angle of the system (and thus the depth of the corona along our line of sight) on how much difference Comptonisation in the corona makes to the reflected spectrum. Coronal optical depths up to 0.9 are considered, which is considerably lower than the case considered here ($\tau \sim 2$), but within the range of optical depths they consider ($\tau = 0.1 - 0.9$) the authors find that the reflected spectrum hardens and deviates more from its original shape as optical depth increases. In the case of $\tau = 0.9$ and high electron energies (> 100 keV) the shape of the Comptonised reflected spectrum approximates the shape of the continuum. Although the electron temperature in the above example from HEART

parameters	homogeneous	constant active regions	varying active regions
n_e (m^{-3})	2.2×10^{22}	4.4×10^{22}	4.4×10^{22}
$\tau_{th,disc}$	2.2	2.9	n/a
$\tau_{th,normal}$	2.2	1.46	n/a
kT_max (keV)	0.08	0.08	0.08
R_cells	12	12	12

Table 3.2: The parameters used (where they differ from those given in table 2.1) to model spectra from a homogeneous and two inhomogeneous coronae, one with constant active regions and the other with varying active regions. $\tau_{th,disc}$ and $\tau_{th,normal}$ are the radial optical depth parallel to the disc and normal to the disc respectively. The optical depth in the case of varying active regions changes in each timestep, but the electron distribution is purely thermal throughout and does not evolve according to the kinetic equation.

is only 50 keV, the higher optical depth makes it reasonable to suppose that after Comptonisation the reflected spectrum in HEART approximates the continuum.

It may be possible to construct a corona with such a geometry that the average optical depth gives an overall spectrum that fits the observed data, but that also allows through a stronger reflected component. For example an inner corona near the black hole may illuminate the outer disc, where the outer disc is not covered by the corona. Such a geometry cannot, however, be modelled in HEART, as directions other than the six parallel to the sides of a cube are required for photons leaving the corona to hit the disc (see section 6.2 for a discussion on such geometries which are not modelled in HEART). This is a possible future improvement to the spectral fitting done in section 4.3.1, but is not expanded on here for reasons discussed in section 4.4 and chapter 6.

3.3.2 Variability in a corona of changing active regions

In a geometry of active regions we also have temporal information. In figure 3.9 the lightcurve (after the system has 'settled', see section 4.1) is shown from another simulation. The parameters are the same as for the constant active regions above, but in this case the active regions may change in every timestep rather than being fixed at the start. In other words, in each timestep electrons are injected into a

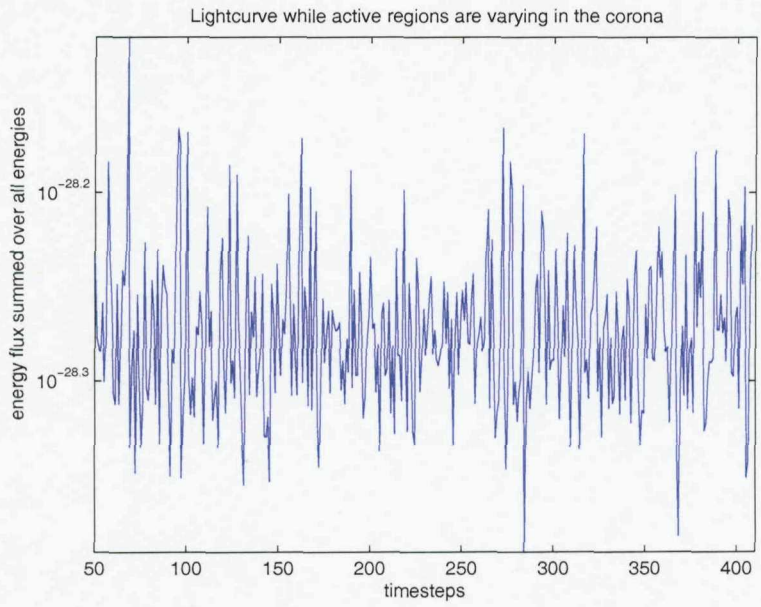

Figure 3.9: A lightcurve showing the varying bolometric flux as the active regions in the corona change in every timestep.

randomly chosen subset of cells, and removed thereafter. No other electron evolution is modelled, i.e. the calculation of the kinetic equation is disabled. The probability for a cell to receive electrons in any given timestep is 0.5. It is shown in the lightcurve that the bolometric flux varies by a factor 2 over the duration of the simulation as the active regions change. The spectra with the highest bolometric flux and two of the spectra with the lowest bolometric flux, one with a low soft bump and the other with a low hard tail, are shown in figure 3.10, as well as the homogeneous case and the (renormalised) integrated spectrum over the whole simulation (after allowing the spectrum to 'settle', see section 4.1).

The integrated spectrum is almost identical to the homogeneous spectrum. So, as well as spectral information being insufficient to distinguish between a homogeneous geometry and one of active regions, it seems it is also insufficient to distinguish between homogeneous, static models and varying, time-averaged models where the observed spectra are integrated over long timescales. This is encouraging for homogeneous, static spectral models, though steady-state models are inadequate if

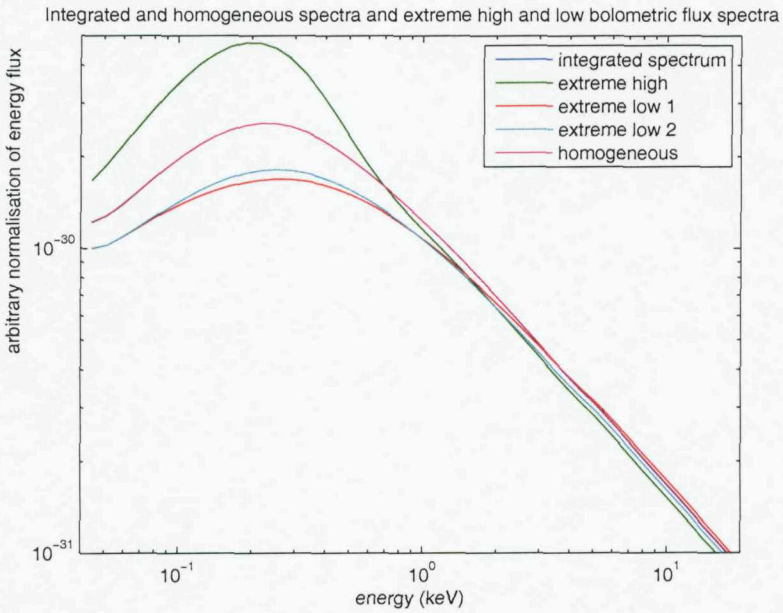

Figure 3.10: A comparison of the (renormalised) integrated spectrum of varying active regions with a homogeneous corona, as well as with the spectrum of the highest bolometric flux and two spectra of the lowest bolometric fluxes occurring during the simulation. The renormalised integrated spectrum is barely visible underneath the homogeneous spectrum as they are almost identical in shape. The actual normalisation of the integrated spectrum is much higher than the other spectra, as it is a sum of the spectra in each timestep, as opposed to the flux from a single spectrum. It is renormalised in order to better compare its shape to the single timestep spectra.
The different extremes can be explained by a corona with electrons in more than half the cells storing a lot of energy, which is suddenly released when a new configuration is randomly chosen where less than half the cells receive electrons.

the object is changing systematically during the integration time-scale, for example during a state transition. It must also be borne in mind that the properties of the corona may change rapidly, which is not captured by a steady-state model, and considering the extremes between which the spectrum changes in figure 3.10, the capability of static, homogeneous models to describe the physical detail of a source may be limited.

The reason for the large difference in output flux between different timesteps, shown in figure 3.10, is explained by the difference in overall optical depth of the corona between timesteps. On average, half the cells will receive electrons in each timestep, but this is not true in a given timestep. Because the probability for a given cell to receive electrons is 0.5, rather than half the cells receiving electrons in each timestep, a different number of cells will receive electrons in different timesteps. In timesteps where more than half the cells are filled with electrons the corona stores more energy, which is then released quickly in a timestep where fewer than half the cells receive electrons.

For technical reasons[5] the corona is changing on unphysical timescales in this simulation (1 timestep $= 4.2 \times 10^{-5}$ s), but similar behaviour is expected on longer timescales. In a simulation where active regions vary more slowly, the system will more closely approach a steady state between changes, but as the steady state in figure 3.7 and the varying spectra in figure 3.10 are comparable this should not affect the result significantly.

Although spectral information is insufficient to distinguish between a steady, homogeneous geometry and one with random active regions when the integration time is long, there is often additional temporal information which may be more useful. More physical simulations and comparisons to temporal data could verify whether modelled active regions produce the same variability as real sources. For

[5]The timestep can only be increased by decreasing the number of cells in the corona, as a timestep is defined to be the time light takes to cross one cell (see equation 2.1). Decreasing the number of cells leads to greater inaccuracies in the modelling, however, and so the only way of modelling a longer time-scale is by running the code for longer, but the code already takes a very long time to run (see discussion in section 4.4).

example Done & Nayakshin (2001) suggest that it may be possible to distinguish between the ADAF model described in section 1.1 and a corona created by magnetic flares, similar to the active regions described here, by the different variability created by the reflected component in the two different geometries. Distinguishing between these two geometries based on their spectra is difficult without more sophisticated models of the reflected component, which take into account the vertical structure of the disc (Done & Nayakshin, 2005).

A significant extension to HEART would be necessary to do this exact comparison, which is beyond the scope of the current work, but this is a demonstration of how HEART can be used to study variability in combination with spectral information. This is investigated further in chapters 5 and 6.

3.4 Energy-dependent removal of low energy electrons

Another feature of the electron distribution that can be improved on is the artificial removal of electrons. In the absence of heating effects for the electrons, the kinetic equation eventually causes a pile-up of electrons in the bin with the lowest energy due to the electron cooling processes described in section 2.2.3. To avoid the numerical problems with this effect, electrons are artificially removed from the lowest energy bin. Whenever the number of electrons in the lowest energy bin, N_l, exceeds the number in the adjacent energy bin, N_{sl}, i.e. whenever $N_l > N_{sl}$, N_l is set equal to N_{sl}.

Sometimes it may be necessary to remove low energy electrons faster than high energy electrons, for example in the HSS where a power-law electron distribution describes the spectrum well, but the thermalisation process of the electrons (Coulomb interactions) prevents the establishment of a long-lived power-law distribution in individual cells.

Previously all electrons escaped as part of the kinetic equation (equation 2.2), which can be represented as,

Parameters	Energy-dependent	Energy-independent
kT_max (keV)	0.39	0.39
Q_e (m^{-3}) t_cross^{-1}	2e22	2e22
equivalent injected τ_p	0.08	0.08
q	3.5	3.5
t_esc t_cross^{-1}	0.8	0.8
t_inj	0.0	0.0
t_esc_threshold (γ)	2.0	n/a

Table 3.3: The parameters used to compare energy-independent and energy-dependent electron removal. t_esc_threshold is T_h in equation 3.11 given in terms of γ, and the other parameters are defined in section 2.3.

$$n_{\gamma_2} = \frac{n_{\gamma_1}}{t_{esc}} \tag{3.10}$$

where n_{γ_2} is the new electron distribution in the next timestep, n_{γ_1} is the old electron distribution from the current timestep and t_{esc} represents the number of timesteps required for n_{γ_2} to escape (t_{esc} is given as a parameter, see section 2.3).

In order to allow electron escape times to depend on energy to counteract fast thermalisation, rather than this energy-independent escape rate, I add the following escape equation,

$$t_{esc,new} = \frac{t_{esc,old}}{\exp(1 - \frac{\gamma}{T_h})} \tag{3.11}$$

where $t_{esc,new}$ is the new value of t_{esc} used in equation 3.10, $t_{esc,old}$ is t_{esc} given as a parameter (see section 2.3) and T_h is a threshold value in γ. Electrons where $\gamma = T_h$ escape as described in equation 3.10, but electrons where $\gamma < T_h$ escape faster and electrons with $\gamma > T_h$ escape more slowly.

This is modelled in addition to the removal of excess electrons in the lowest energy bin whenever $N_l > N_{sl}$.

Energy-dependent electron removal is demonstrated in figure 3.11, where it is compared to energy-independent electron removal. The parameters used are listed in table 3.3 (where they are different from the values given in table 2.1), and in this

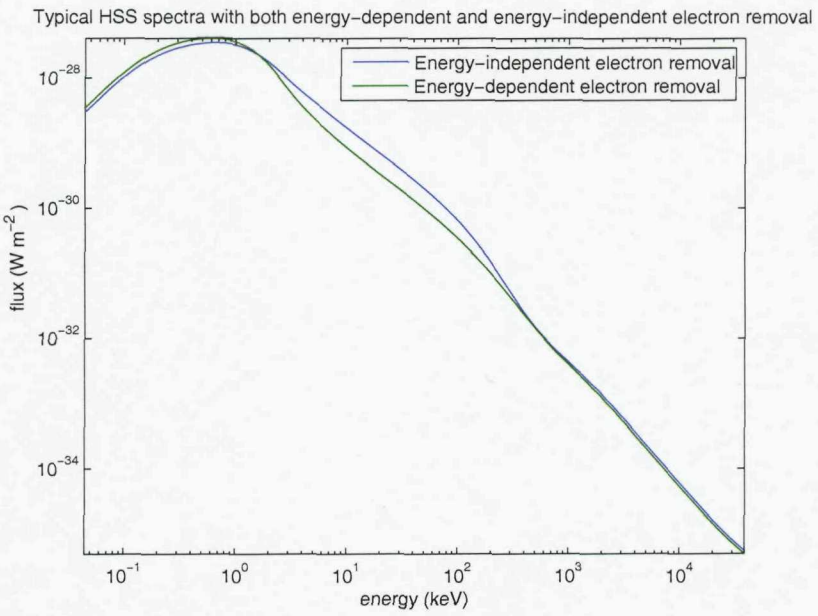

Figure 3.11: Spectra of a typical HSS demonstrating the difference between energy-dependent electron removal and energy-independent electron removal. The spectral bump created by the thermalised electrons in the energy-independent version can be seen clearly, preventing a flat power-law spectrum.

case electron evolution according to the kinetic equation is modelled[6]. Including energy-dependent electron removal gives a smoother power-law tail, and the bump created by the thermalised electrons in the energy-independent case is seen clearly.

This is a technical feature, however, necessary due to the discretisation used in the code, and is not comparable to a physical situation. Two different ways of dealing with this technical issue are compared here without being based on a physical explanation. The physical implications of the technical treatment should, however, be considered, whichever version is used.

3.5 Anisotropy of Compton scattering

One of the greatest weaknesses of HEART is the lack of treatment of the anisotropy of Compton scattering, as the scattering angle, the probability of a scattering event and the energy transfer depend on the interaction angle of the photon and the electron (Blumenthal & Gould, 1970). Isotropic conditions are assumed inside each cell in HEART when using equations 2.31 and 2.32 to calculate the intensity of scattered photons. This is a valid assumption, at least initially, for the electrons, as long as we do not wish to model bulk motion, but all the photons are initially travelling upwards, and later different numbers of photons travel in each of the six modelled directions, a potentially highly anisotropic situation. Initially photons are more likely to continue upward or be back-scattered in the downward direction rather than scatter into a given sideways direction. More than 1/6th of the scattered photons should continue upwards, more than 1/6th should back-scatter and less than 4/6th should be side-scattered, though this is strongly energy-dependent. While at low photon energies (scattered photon energy $\sim$ 0.04 keV) the 1/6th approximation is quite good ($\sim$ 1/5th should forward-scatter and $\sim$ 1/5th should back-scatter, see equation 3.12), the anisotropy effect becomes more important with increasing photon energy ($\sim$ 70% of scattered photons at $\sim$ 40 MeV should forward-scatter).

[6]Electron heating is not modelled in HEART, but rather injection of hot electrons and removal of colder electrons. This is not physical, and the parameters given in table 3.3 do not refer to the equilibrium electron distribution. This is discussed further in chapter 6.

HEART is not suitable for including a full anisotropic treatment of Compton scattering for two main reasons. Firstly, the restriction of only modelling six directions limits the usefulness of any angular treatment that can be implemented. Including an anisotropic treatment of Compton scattering may improve spectra to an extent within the framework of the six direction restriction, but this restriction may be too great to improve the spectra sufficiently. Also, one of the most useful outcomes of including an angular treatment would be to model spectra dependent on viewing angle. This may even be necessary for accurate spectral fitting (Haardt & Maraschi, 1991; Haardt, 1993; Haardt & Maraschi, 1993; Stern et al., 1995a,b; Poutanen & Svensson, 1996). Strictly speaking, with the six direction restriction it is only possible to model spectra of inclination angles 0° and 90°.

Secondly, if the anisotropy of Compton scattering is to be taken into account, the scattering cross-sections used throughout the Comptonisation calculations must be changed as well as the structure in which information about the photon distributions is kept. More information must be stored, for example a larger number of directions for photons to travel in, and each scattered photon must be linked with its pre-scattered energy state to allow the accurate determination of its path after scattering.

In essence, if HEART is to model the anisotropy of inverse Compton scattering accurately, it must be modified significantly, including the basic structure upon which it is built. For example, more photon directions could be modelled by changing the shape of a cell from a cube to a structure with more sides which still tessellates. The algorithm for building the corona and linking the cells would have to be reworked, and this would increase the run-time of the code. Another possibility is to model several photon directions within a cubic cell, but this introduces an error in the photon propagation time. Photon distributions necessarily propagate from one cell to the next in one timestep because of the distribution storage system in HEART. The maximum error would occur for photons travelling along the diagonal, which would travel a factor of $\sqrt{2}$ too fast. In either case, taking these effects into account would increase the run-time of the code.

Before attempting to make such significant changes, we must be sure that they are both feasible and necessary. It is only worth reworking HEART in this way if HEART is suitable for the fitting of spectra with long integration times, and if the anisotropy of Compton scattering can be implemented satisfactorily. The suitability of HEART to spectral fitting in this sense is discussed in chapter 4, but to summarise, it is not practical to use HEART routinely for fitting of steady-state spectra due to its long run-times and limited reliable parameter range[7].

Nevertheless, it is worth investigating how much difference the inclusion of an anisotropic treatment of Compton scattering is likely to make to the angle-averaged spectrum, and whether a slightly better approximation than the assumption of isotropic scattering could improve the spectra for more accurate variability modelling. I have implemented an approximation to an anisotropic treatment of inverse Compton scattering, which I refer to as 'directionality' hereafter. The cell structure and restriction to six directions remain unchanged, and the scattering cross-sections assuming isotropic conditions are still used, but I have modified the fraction of scattered photons being scattered into each possible direction, rather than always assuming 1/6th. This approach should be viewed as the simplest conceivable modification towards an implementation of anisotropic scattering. It also allows test modelling of extreme situations, for example 100% forward scattering, to gauge how significant an improved treatment is likely to be.

Given that a photon has undergone scattering to a pre-calculated energy (determined by the equations in section 2.2.3.3 assuming isotropic conditions), I determine the scattering angle depending on which direction it came from and its pre-scattered energy according to Lei et al. (1997)

$$\frac{\mathrm{d}\sigma_{KN,U}}{\mathrm{d}\Omega} = \frac{1}{2} r_0^2 \epsilon^2 [\epsilon + \epsilon^{-1} - \sin^2\theta], \tag{3.12}$$

where $\sigma_{KN,U}$ is the Klein-Nishina differential cross-section of a free electron at rest in the case of unpolarised radiation, r_0 is the classical electron radius, θ is the

[7]Further limitations are discussed in chapter 6.

scattering angle (the angle between the initial photon trajectory before scattering and the scattered photon trajectory) and

$$\epsilon = \frac{E'}{E_0} = \frac{1}{1 + (E_0/m_e c^2)(1 - \cos\theta)}, \tag{3.13}$$

where E' is the energy of the scattered photon and E_0 is the photon energy before scattering.

In the case of the cubic cells in HEART, equation 3.12 is calculated for three different cases: forward-scattering, back-scattering and side-scattering. A photon is equally likely to scatter into any of the four sideways directions, hence it is only necessary to calculate the probability of scattering into one of the sideways directions. Scattering is assumed to occur at the centre of a cell, thus the probability of a certain photon direction after a scattering event is given by integrating equation 3.12 over the solid angle, Ω, containing the face of the cube that the scattered photon travels towards. This is a large approximation, as is illustrated in figure 3.12, but is necessary due to the fact that only six directions are modelled.

For example, consider a photon entering the cell from face B in figure 3.13. To calculate the probability of forward-scattering I integrate equation 3.12 over the solid angle containing face F. The probability of back-scatter is calculated using the solid angle containing face B and the probability of side-scatter is calculated using the solid angle containing any of the other four sideways faces.

Assume that the scattering event occurs at the origin upon which a cube with sides of length 2a is centred in Cartesian coordinates. Consider forward-scattering only, into a cube face on the plane z = a, and refer to figure 3.14. From equation 3.12 the scattering cross-section is

$$\sigma_f = \int_{-a}^{a}\int_{-a}^{a} \frac{1}{2} r_0^2 \epsilon_f^2 (\epsilon_f + \epsilon_f^{-1} - \sin^2\theta_f) \mathrm{d}\Omega, \tag{3.14}$$

where ϵ_f, θ_f and $\mathrm{d}\Omega$ are calculated below. In figure 3.14 the origin, O, is at the centre of the cell where the scattering event occurs. Only the face into which

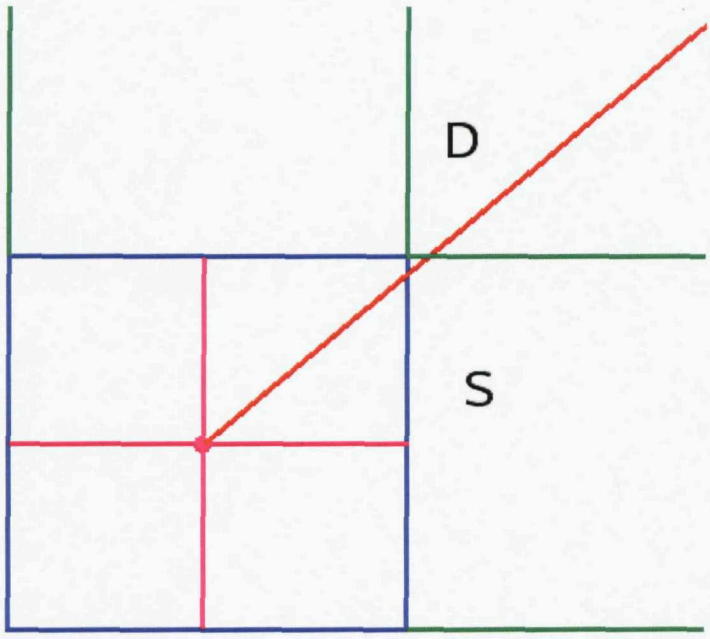

Figure 3.12: A two-dimensional illustration of one of the approximations caused by modelling only six directions. Scattering is assumed to occur at the centre of the blue cell, i.e. at the purple dot. The purple lines represent the photon paths modelled by HEART, whereas the red line represents a possible, physical photon path which is not modelled by HEART. In HEART, a photon travelling along the red line is transferred into the neighbouring green cell labelled 'S', and thus integrating the Klein-Nishina differential cross-section over the solid angle containing each face of the cube gives the probability of scatter into the neighbouring cell sharing that face, as described in figure 3.14. As is clear from this diagram, however, a photon travelling along the red line actually spends very little time in cell 'S', and would more accurately be transferred to the cell on the diagonal, cell 'D'.

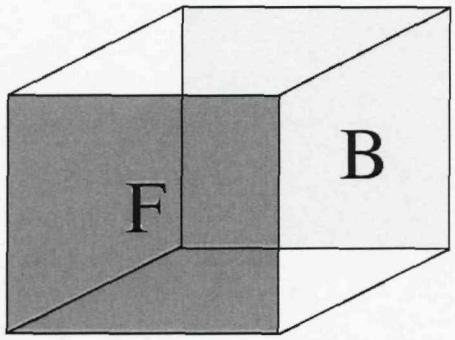

Figure 3.13: The faces of a cell in HEART. The near face is labelled 'F' and the far face is labelled 'B'. For example, if a photon enters the cell through face B and forward scatters at the centre of the cell, then it will subsequently leave the cell through face F.

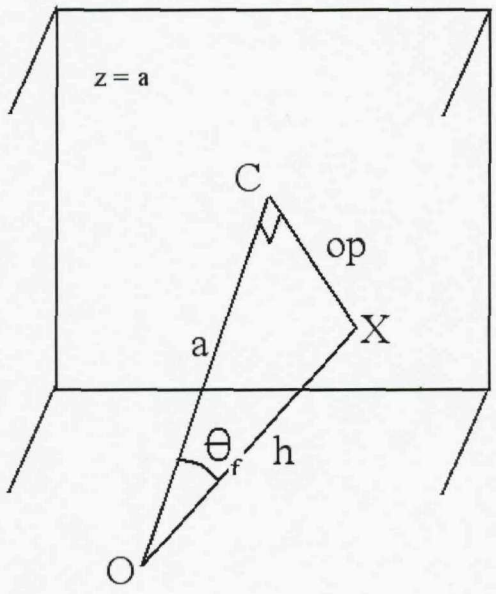

Figure 3.14: Calculating the solid angle containing the face of a cube in Cartesian coordinates.

forward-scattering occurs is shown, and this is the face I compute the solid angle for. This face is located on the plane z=a, so the centre of the face is at point (0,0,a), point C in figure 3.14. The vector joining the origin O to point C, $\overline{OC}$, represents the direction of the photon before scattering, and the vector joining the origin O to a random point X(x,y,a) on the cube face, $\overline{OX}$, represents the direction of the photon after scattering. θ_f is as marked in the figure, the angle between the initial photon trajectory and the scattered photon trajectory.

Now consider the right-angled triangle in figure 3.14. The hypotenuse, h, is equal to the length of $\overline{OX}$, call it r_f, hence h $= r_f = \sqrt{(x^2+y^2+a^2)}$. The adjacent is equal to a as O and C are fixed, and the opposite, op, is the length of $\overline{CX}$ on the z=a plane, so op $= \sqrt{(x^2+y^2)}$. Therefore $\sin\theta_f = \sqrt{x^2+y^2}/r_f$ and ϵ_f is as in equation 3.13 but with $\cos\theta = \cos\theta_f = a/r_f$.

$d\Omega$ can easily be derived for the face of a cube, and I follow the method from Weisstein (2008) here. The solid angle is defined as

$$\Omega \equiv \int\int_S \frac{\mathbf{n}\cdot\mathbf{da}}{r^2} \tag{3.15}$$

where $\mathbf{n}$ is a unit vector from the origin, $\mathbf{da}$ is a small area on the surface Ω of a unit sphere and r is the radius of $\mathbf{a}$ from the origin. To find the solid angle of the face of a cube with sides of length 2a, consider again the face in a Cartesian x,y,z coordinate system which is located on the z plane, z = a, with the cube centred on the origin. Notice that $\mathbf{n}\cdot\mathbf{da} = \cos\theta dxdy$ where θ is the polar angle (the angle between the perpendicular to the area of the face of the cube and the perpendicular to the small area $\mathbf{da}$ on a unit sphere) and that $r = \sqrt{(x^2+y^2+a^2)}$. Then

$$\Omega = \int_{-a}^{a}\int_{-a}^{a} \frac{\cos\theta}{\sqrt{(x^2+y^2+a^2)}} dxdy \tag{3.16}$$

and since $\cos\theta = a/r_f$

$$\Omega = \int_{-a}^{a}\int_{-a}^{a} \frac{a}{(x^2+y^2+a^2)^{3/2}} dxdy \tag{3.17}$$

hence

$$\mathrm{d}\Omega = \frac{a}{(x^2+y^2+a^2)^{3/2}}\mathrm{d}x\mathrm{d}y \tag{3.18}$$

A similar calculation can be done for side-scattering,

$$r_s = \sqrt{(x^2+a^2+z^2)} \tag{3.19}$$

$$\sin\theta_s = \frac{\sqrt{(x^2+a^2)}}{r_s} \tag{3.20}$$

$$\cos\theta = \frac{z}{r_s} \tag{3.21}$$

$$\mathrm{d}\Omega = \frac{a}{(x^2+a^2+z^2)^{3/2}}\mathrm{d}x\mathrm{d}z \tag{3.22}$$

and for back-scattering,

$$r_b = \sqrt{(x^2+a^2+z^2)} \tag{3.23}$$

$$\sin\theta_b = \frac{\sqrt{x^2+y^2}}{r_b} \tag{3.24}$$

$$\cos\theta = \frac{-a}{r_b} \tag{3.25}$$

$$\mathrm{d}\Omega = \frac{-a}{(x^2+y^2+a^2)^{3/2}}\mathrm{d}x\mathrm{d}z. \tag{3.26}$$

Now the number of scattering events in the forward direction is $n_e\sigma_f l$ where n_e is the number density of electrons and l is the distance travelled by a photon, thus the total number of scattering events is $n_e\sigma_f l + n_e\sigma_b l + 4n_e\sigma_s l$. Therefore the probability of forward-scatter, p_f, is

$$p_f = \frac{n_e l\sigma_f}{n_e l\sigma_f + n_e l\sigma_b + 4n_e l\sigma_s} = \frac{\sigma_f}{\sigma_f+\sigma_b+4\sigma_s} \tag{3.27}$$

and similarly for back and side-scattering. By normalising the scattering cross-sections I obtain the probability of scattering into each cube face.

It is only necessary to calculate these cross-sections once at the start of the

code for every modelled photon energy. The same values can then be used in every timestep when calculating the photon direction after each inverse Compton scattering event. In HEART the scattered distribution (equation 2.31) and the pre-scattered distribution (equation 2.32) are calculated separately, i.e. the scattered distribution, ν_1 is calculated and added to the photon distribution, at which point the scattered photons exist twice because the photons ν_0 which scattered to ν_1 have not yet been removed. These photons (ν_0) are 'absorbed' separately using equation 2.32. Because of this procedure it is not possible to link a scattered photon with its pre-scattered energy in HEART. This introduces a complication as the direction of the scattered photon depends on its pre-scattered energy, ν_0. I make an approximation, which is most easily described by considering a specific photon distribution.

Consider a given cell, and consider the photon distribution, Ψ, entering the cell from face B in figure 3.13 at the start of a timestep. Some of the photons in Ψ undergo scattering, call them Ψ_0, and call the scattered distribution Ψ_1. I wish to find the proportion of Ψ_1 which is scattered forwards (into face F), backwards (into face B) and sideways (into one of the other, sideways faces). This proportion must be independent of the pre-scattered energy as the pre-scattered energy is unknown, so that the same proportion can be applied to Ψ_1 over all energies. Now consider only forward-scattering. To find the proportion which forward-scatter, $\Psi_{0,\text{for}}$, I multiply the intensity in each energy bin of Ψ_0 by the energy-dependent probabilities of forward-scattering calculated in 3.12, $\sigma_{\text{for}}(\nu)$:

$$\Psi_{0,\text{for}}(\nu) = \Psi_0(\nu)\sigma_{\text{for}(\nu)} \tag{3.28}$$

I convert to photon number to avoid high energy photons being weighted more than low energy photons later, thus $\Psi_{0,\text{for}}(\nu)$ gives the number of forward-scattered photons in each pre-scattered energy bin. In order to remove the dependence of $\Psi_{0,\text{for}}$ on energy I sum over energy. The total number of photons coming from face B and scattering into face F, Ψ_{BF} is

$$\Psi_{\mathrm{BF}} = \sum_{\nu} \Psi_{0,\mathrm{for}}(\nu). \tag{3.29}$$

Similarly, I find the number of photons coming from face B which back-scatter into face B, Ψ_{BB} and side-scatter into the other faces, $4\Psi_{\mathrm{BS}}$. I then normalise to obtain energy-independent probabilities of forward-scatter, p_f, back-scatter, p_b, and side-scatter, p_s:

$$\begin{aligned} \Sigma &= \Psi_{\mathrm{BF}} + \Psi_{\mathrm{BB}} + 4\Psi_{\mathrm{BS}} \\ p_b &= \Psi_{\mathrm{BB}}/\Sigma \\ p_f &= \Psi_{\mathrm{BF}}/\Sigma \\ p_s &= \Psi_{\mathrm{BS}}/\Sigma \\ p_b + p_f + 4p_s &= 1 \end{aligned} \tag{3.30}$$

The factor of 4 enters because there are four sides into which photons can side-scatter. These probabilities are then applied to the scattered distribution, Ψ_1, over all energies, to determine what fraction of the scattered photons continue in each direction, rather than 1/6th in each.

When this has been done for the photons coming from face B, it is also done for the photons coming from the other faces, and the contributions from each photon distribution to each direction are added. For example photons leaving through face F are those which forward-scattered from B, back-scattered from F and a quarter of those which side-scattered from each of the other faces. This is then repeated for every cell. This treatment is similar to assuming that a given scattered photon was scattered proportionally from all the pre-scattered photons calculated in equation 2.32.

Using an average probability over energies in this way causes low energy photons to have too great a probability of forward-scatter in HEART, and high energy

photons to have too small a probability of forward-scatter. These probabilities are re-calculated in every timestep, and so, as the energy of the overall photon distribution increases, the probability of forward-scatter also increases.

Although this approximation is an improvement on the 1/6th assumed previously, it is still a weak treatment of the anisotropy of Compton scattering. Each of the six distributions in each cell is now treated individually, however, so HEART is in a better form to deal with anisotropic scattering events should such a modification be required in future. It is also easy to change the probabilities of forward, back and side-scatter to any required value, to gain a better understanding of how much difference modelling the anisotropy of inverse Compton scattering makes to the angle-averaged spectrum of HEART, within the current restrictions.

3.5.1 Results of the new approximation to anisotropy of Compton scattering

A comparison of HEART to *compTT* is made in section 4.2, and this new treatment of directionality is included and discussed there, but only for the case where electron evolution is not modelled, i.e. the calculation of the kinetic equation is disabled. I include a short summary here.

Including directionality increases the range of parameters over which HEART can be used to include high Compton y parameters (defined in section 4.2) in excess of 15. Without directionality HEART is valid for low Compton y parameters $\lesssim 3$, and in this case the 1/6th approximation is better. Figures 4.4, 4.5, 4.6 and 4.7 demonstrate the parameter range over which directionality should be used. It is particularly evident in figure 4.5 how the scattered photon component is underestimated with directionality and overestimated without directionality for high optical depths.

This new approximation has made a significant difference to the output spectra, showing that the treatment of anisotropy in Compton scattering changes the angle-averaged spectra from HEART significantly. It is possible that including a more complete treatment would significantly extend the applicability of HEART. It is

also possible, however, that the reason HEART only agrees with *compTT* for low Compton y parameters is that the optical depth per cell is too high in the case of high Compton y parameters, and so does not comply with the restrictions imposed to ensure that the radiative transfer is modelled accurately. Currently, however, a basic form of HEART can be used for restricted parameter ranges discussed in section 4.2.

Chapter 4

Testing HEART

The HEART code includes several physical processes and features described in the previous chapters. Simple checks are made throughout in Collins (2004) and in the figures in chapter 3, to ensure that the HEART output is sensible and qualitatively as expected, but HEART has not yet been properly tested or applied to explain real data.

I test the HEART code by comparing it to the analytic model by Titarchuk (1994), and by fitting observed X-ray spectra of Cyg X-1 in the LHS and the HSS. The analytic model is widely used and tested in the literature (see for example Hua & Titarchuk (1995) and Skibo & Dermer (1995) for comparisons to Monte Carlo codes), but is very limited in that it only describes steady-state configurations in homogeneous spherical and slab geometries. HEART should, however, agree with the analytic model under these limited conditions. As the observed spectra are obtained from observations with long integration times, I model a stationary configuration of the accretion disc and corona without an evolving electron distribution, i.e. the calculation of the kinetic equation is disabled, to allow the comparison with both the analytic model and the observed spectra. This also allows the testing of HEART in its most basic form.

4.1 Practical Considerations

Before testing and using HEART some practical considerations are necessary. 'Equilibrium' is detected within the code by comparing the output spectra of two consecutive timesteps. If they agree with each other within a user-specified tolerance, then the code assumes that a steady state has been established. Here I use an analytic estimate combined with a simple Monte Carlo code to set a number of timesteps (sim = Normal, see section 2.3) to avoid an apparent equilibrium being reached too early. While the photons undergoing multiple scattering events make little difference to the output of each consecutive timestep, their summed effect is significant over a large number of timesteps, making equilibrium conditions difficult to implement in the case of a corona with high optical depth.

The analytic estimate is valid only in optically thick cases, and is described in appendix A.3. The Monte Carlo code is valid for all optical depths, and calculates an escape time estimate. I use the same cell structure as the corona in HEART in the Monte Carlo code, and scattered photons are equally likely to scatter into any of the 6 modelled directions. The probability of undergoing scatter is equal in all cells and is set initially by an optical depth given by the user. No energy dependence is modelled, though a fraction can be specified to multiply the scattering probabilities by, to mimic the decreasing scattering probability with increasing energy. A specified number of photons, usually $\sim$ 1000, are then followed as they traverse the corona one by one, and the code outputs the maximum number of timesteps any photon required to escape, where a timestep is as defined in HEART (see equation 2.1). This is a fairly crude estimate, but gives a good starting point.

After obtaining estimates from appendix A.3 and this Monte Carlo code, I run HEART for the maximum estimate for the number of timesteps, and also for twice as long to ensure that the code reaches a steady state. If the spectrum is identical in these two runs, then I assume that I can safely use the number of timesteps suggested by the estimates described above. This method is used throughout my work, and I find that my crude estimates of the required number of timesteps is

always sufficient.

4.2 Comparison to an analytic model

With these practical considerations, I now compare the output of HEART with the analytic model of Titarchuk (1994) as implemented in XSPEC version 11.3.2.t as model *compTT*. To approximate the conditions assumed in the *compTT* model, a spherical corona with central injection of blackbody seed photons, I continue to use the ECorona model (see section 2.3), a spherical corona with an accretion disc, but with a very small disc to approximate only central seed photon injection. The solution of the kinetic equation in individual cells is disabled as *compTT* assumes a static electron energy distribution. Thus the electron density parameter in equations 2.3 and 2.4, n_γ, refers to the actual electron density and not the time-dependent density of electron injection. Bremsstrahlung, synchrotron radiation and reprocessing in the disc are also disabled.

3604 cells (corresponding to a 24 cell diameter of the corona) are used to construct a hemisphere and the corona is assumed to be symmetric. Full reflection is modelled, so photons propagating out of the modelled hemisphere through its circular cross-section are reflected back into the modelled region as, by symmetry, they correspond to photons entering the modelled hemisphere from the unmodelled hemisphere (see section 3.2). A purely thermal electron distribution is modelled in each cell (Q_e = 0 m^{-3}, see section 2.3), and does not evolve.

Parameters within the applicability region given by Skibo & Dermer (1995) for the *compTT* model are used. The HEART and *compTT* spectra are plotted in figures 4.1, 4.2 and 4.3 for optical depths $\tau_{th} = 0.5, 1.5$ and 5, for electron temperatures 50 and 100 keV and for maximum disc temperatures of 0.1 and 0.3 keV.

The slopes of the Comptonised spectra are consistent between HEART and *compTT* at low optical depth, up to $\tau \sim 2$, and at electron temperatures up to ~ 100 keV for both disc temperatures. Equivalently, the models agree for the non-relativistic Compton y parameter $y_{NR} = (4kT/mc^2)\mathrm{Max}(\tau, \tau^2) \lesssim 3$. The models

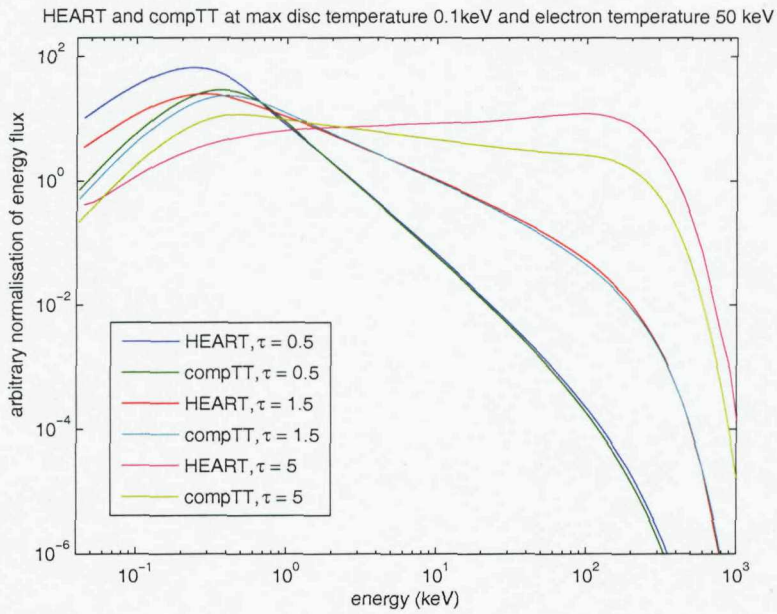

Figure 4.1: Spectra from HEART and *compTT* for optical depths $\tau_{th} = 0.5$, 1.5 and 5 with a maximum disc temperature of 0.1 keV and electron temperature 50 keV.

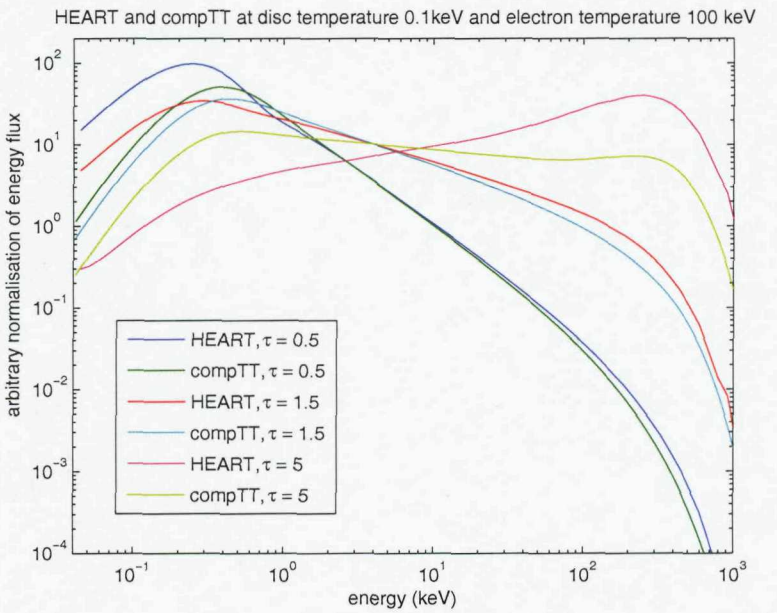

Figure 4.2: Spectra from HEART and *compTT* for optical depths $\tau_{th} = 0.5$, 1.5 and 5 with a maximum disc temperature of 0.1 keV and electron temperature 100 keV.

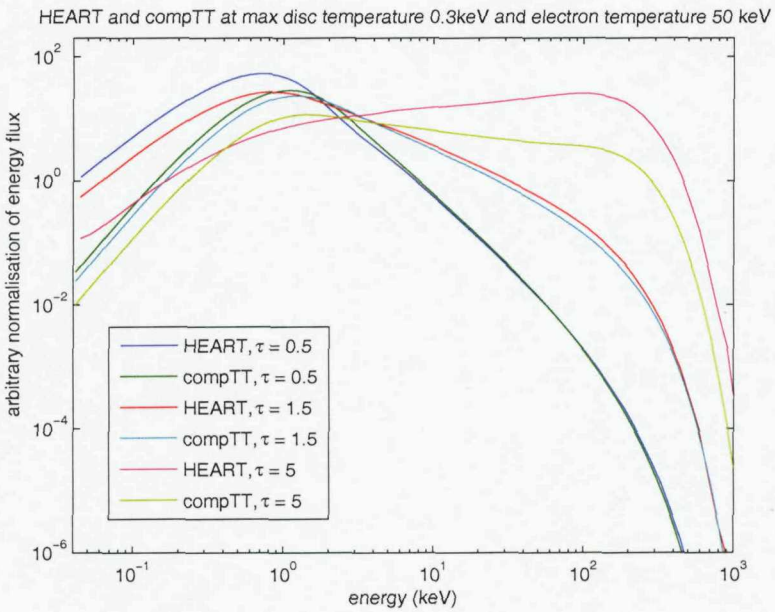

Figure 4.3: Spectra from HEART and *compTT* for optical depths $\tau_{th} = 0.5$, 1.5 and 5 with a maximum disc temperature of 0.3 keV and electron temperature 50 keV.

are not expected to match exactly as the approaches are quite different, but two possible reasons for the significant discrepancy at large optical depths are easily deduced from the limitations of HEART. Firstly, the optical depth per cell, τ_{cell}, must be much smaller than 1 for equation 2.30 to be valid. Here, $\tau_{cell} = 0.04$ in the examples where the radial optical depth, τ_{th}, is 0.5, but $\tau_{cell} = 0.4$ when the radial $\tau_{th} = 5$. Thus the approximation used to model Compton scattering is only valid for small radial optical depths, the cases where HEART agrees well with *compTT*. The only way of modelling a radial optical depth of 5 with a sufficiently small τ_{cell} for this approximation to be valid, is by modelling more cells. A corona diameter, R_cells, of significantly more than the 24 cells used here is necessary, but that is prohibitively computer intensive. Thus HEART is limited to modelling small radial optical depths by the combined limitations of $\tau_{cell} \ll 1$ and R_cells $\lesssim 24$.

A second possible reason is that the lack of treatment of the anisotropy of inverse Compton scattering in HEART contributes to HEART overestimating the scattered

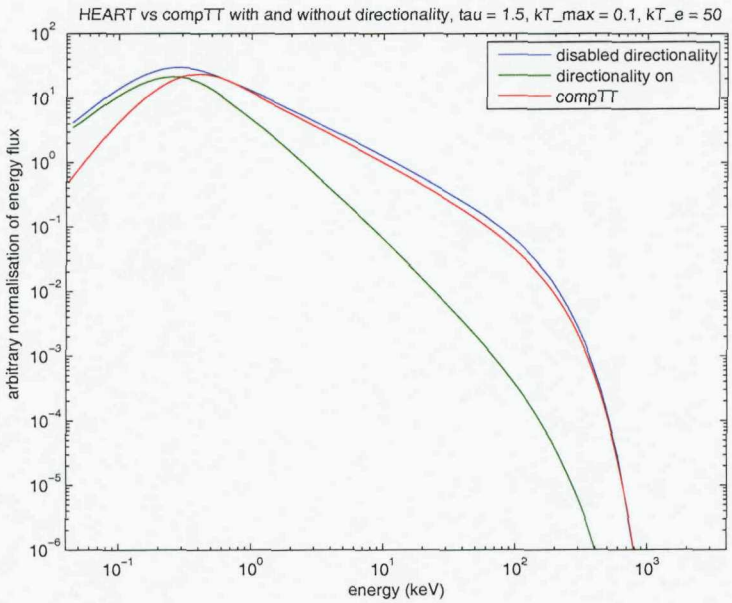

Figure 4.4: Spectra from HEART with and without directionality and *compTT* for optical depth $\tau_{th} = 1.5$ with a maximum disc temperature of 0.1 keV and electron temperature 50 keV.

photon distribution for high optical depths and electron temperatures. As the photons gain energy they become more likely to undergo forward-scatter (with minimum energy transfer) and escape the corona faster than HEART predicts.

The high (relativistic) Compton y parameter case, $y_R = 16(kT/mc^2)^2\mathrm{Max}(\tau, \tau^2) \gtrsim 15$ can be improved on by including the new approximate treatment of anisotropy of Compton scattering, 'directionality', described in section 3.5. Figures 4.4, 4.5, 4.6 and 4.7 show a comparison between compTT, HEART with directionality and HEART without directionality. The approximation of scattered photons being equally likely to undergo scattering into any of the faces of the cell works better for $y_{NR} \lesssim 3$, but for $y_R \gtrsim 15$ including directionality is a better approximation. Low energy photons are more likely to forward-scatter and escape than they should be with directionality on, hence the deficiency of scattering events in the low optical depth case. Where scattering events are more likely and photons are scattered to higher energies (i.e. at higher optical depth), however, this increased probability of

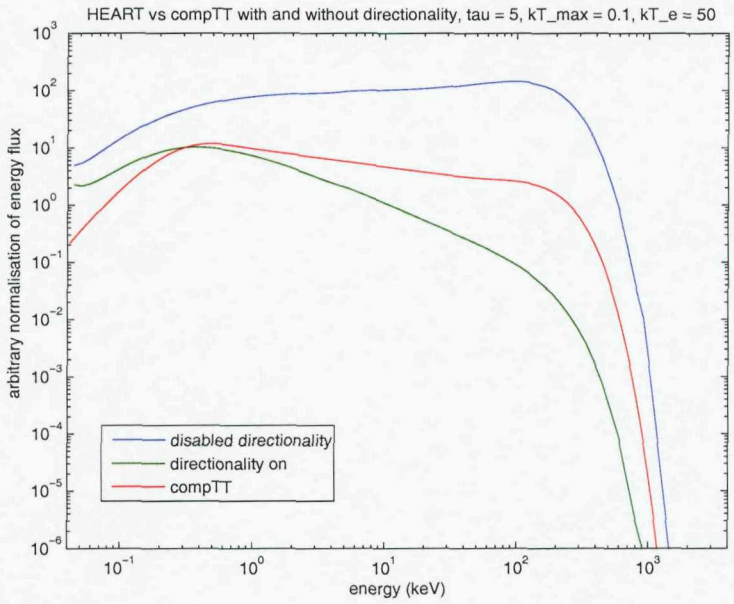

Figure 4.5: Spectra from HEART with and without directionality and *compTT* for optical depth $\tau_{th} = 5$ with a maximum disc temperature of 0.1 keV and electron temperature 50 keV.

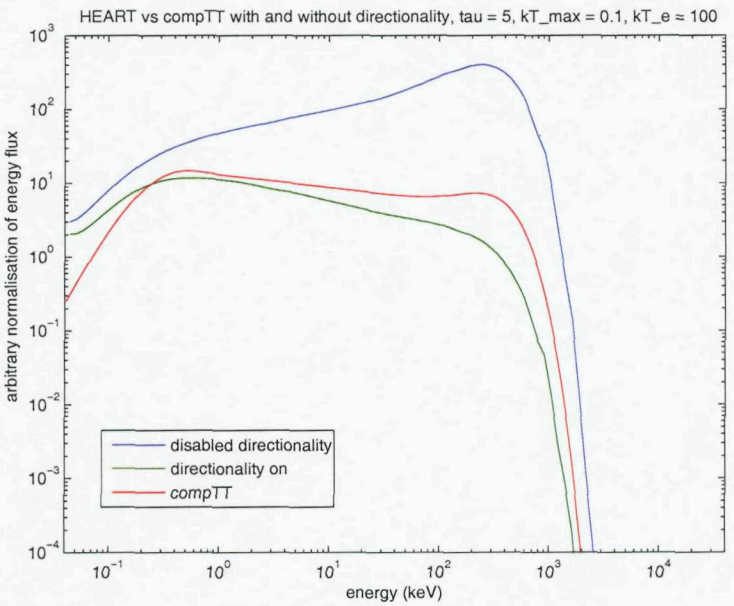

Figure 4.6: Spectra from HEART with and without directionality and *compTT* for optical depth $\tau_{th} = 5$ with a maximum disc temperature of 0.1 keV and electron temperature 100 keV.

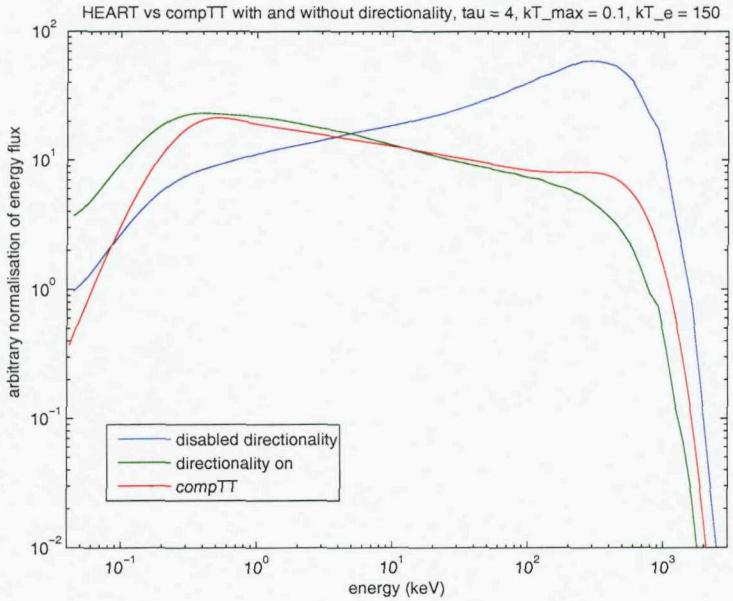

Figure 4.7: Spectra from HEART with and without directionality and *compTT* for optical depth $\tau_{th} = 4$ with a maximum disc temperature of 0.1 keV and electron temperature 150 keV.

escape is necessary. For Compton y parameters between $y_{NR} \gtrsim 3$ and $y_R \lesssim 15$, including directionality underestimates the scattering component whereas using the 1/6th approximation overestimates the scattering component (as in figure 4.5). A better treatment of anisotropic Compton scattering is required. Using this new approximation of the anisotropy of Compton scattering changes the output spectra significantly, however, and so including an improved treatment of this anisotropy may provide sufficiently accurate spectra, though the requirement that $\tau_{cell} \ll 1$ must also be included.

The greater soft excess in the HEART spectrum is due to a slightly extended multicolour disc in HEART compared to a central blackbody in *compTT*. The expected high energy cut-off at $\sim 3\mathrm{kT_e}$, where $\mathrm{kT_e}$ is the temperature of the thermal electron distribution, is seen in both models.

It is not ideal that different treatments are necessary for different values of y, or that only low and high values of y are modelled well, but for the purposes of fitting

data from X-ray binaries the expected fitting parameters ($y_{NR} \lesssim 3$) lie within the region where HEART agrees well with *compTT*.

4.3 Comparison to data from Cyg X-1 in the low hard state and the high soft state

After comparing HEART to the analytic model of Titarchuk (1994), the next test is to apply HEART to fit observational data. I use HEART to fit Cyg X-1 data in the LHS and the HSS. No attempt is made to improve on previous fits, only to demonstrate the capability of HEART to fit observed data with reasonable physical parameters. This is done for testing purposes only, and a discussion of how suitable HEART is for spectral fitting is given in section 4.4. For simplicity, and for ease of comparison to previous spectral fitting of the same data, a spherical, static, homogeneous electron corona is used, and only inverse Compton scattering of multicolour blackbody photons injected from an underlying disc (as described in section 2.2.4) is modelled. As above, evolution of the electron energy distribution is disabled. Thus HEART is being used with similar capabilities to *compTT* within its restricted parameter range, for the purposes of fitting this data and is, again, being tested in its most basic form.

Cyg X-1 was observed by *BeppoSax* on May 3rd and 4th 1998 (DiSalvo et al., 2001) in the LHS and on 22nd June 1996 (Frontera et al., 2001) in the HSS, and HEART is used to fit this data. I use XSPEC version 11.3.2.t to analyse the fits, where the HEART output is implemented as a table model. A multiplicative constant allows different normalisations for different instruments allowing for uncertainties in the absolute calibrations of individual instruments. The reflection component and fluorescent iron line are added separately in the LHS using the XSPEC models *reflect* by Magdziarz & Zdziarski (1995) and a Gaussian respectively. In the HSS HEART models the reflection component, and a Gaussian is used to fit the iron line. This different treatment of the two states is discussed in sections 4.3.1 and 4.3.2,

but in both cases the reflection component is added without modelling the heating of the disc caused by the absorbed photons, i.e. the coupling of the disc and corona are not modelled. This is therefore not a self-consistent model.

A full list of HEART parameters and settings is given in tables 2.1 and 2.2 respectively, and the best fit parameters are given in table 4.1 for both states where they differ from those given in table 2.1. The parameters which are the same for both fits are discussed here, and the ones which differ between the states are discussed in sections 4.3.1 and 4.3.2. I model a spherical corona covering an optically thick, geometrically thin disc (the ECorona model). Photons of frequency $1.0 \times 10^{16} - 1.0 \times 10^{22}$ Hz (0.0414 keV - 41 MeV) are modelled, covering a significantly broader band than the observational data, and electrons with $\gamma = 1$ - 1000 are modelled, including a range of nonrelativistic to highly relativistic electrons. The diameter of the corona is 3×10^6 metres, although this is somewhat arbitrary and the total optical depth is more important. The fitting algorithm of XSPEC is used to set the overall normalisation and the model *phabs* determines absorption by neutral hydrogen. Hence the distance assumed for Cyg X-1, 2 kpc, is not important, and galactic absorption is set to 0 in HEART itself. The mass of the black hole in Cyg X-1 is assumed to be 5 $M_\odot$ which is within the range given in Herrero et al. (1995). The exact number used is not crucial as it is only used to provide a scaling factor for values given in Schwarzschild radii. I model only inverse Compton scattering and reflection (without absorption and heating in the disc), so I assume no magnetic field (B = 0), and bremsstrahlung and electron evolution by the kinetic equation are disabled. Hence the electron distribution remains the same in each cell throughout the simulation, and n_e and Q_e represent actual electron densities rather than time-dependent injected densities.

4.3.1 Cyg X-1 in the LHS

The best fit parameters to the LHS data are listed in table 4.1 and the range of parameters used in determining this best fit is listed in table 4.2. Only thermal

HEART parameters	The LHS	The HSS
n_e (m^{-3})	2.2×10^{22}	0
(equivalent to τ_{th})	2.2	0
kT_e (keV)	49.6	0
Q_e (m^{-3})	0	0.12×10^{22}
(equivalent to τ_p)	0	0.12
q	0	4.1
kT_max (keV)	0.08	0.39

Table 4.1: The best fit parameters of HEART for the LHS and HSS data. n_e and kT_e are the thermal electron parameters n_e and kT_e as defined in equation 2.3 and Q_e and q are the power-law electron parameters n_e and q as defined in equation 2.4. kT_max converted to Kelvin is t_{max} at r_{in} in equation 2.36. Note that the evolution of the electron distribution is not modelled and the calculation of the kinetic equation is disabled.

HEART parameters	The LHS	The HSS
n_e (m^{-3})	$2 \times 10^{22} - 4 \times 10^{22}$	0
corresponding τ_{th}	2-4	0
kT_e (keV)	45-65	0
Q_e (m^{-3})	0	$1.24 \times 10^{17} - 3.3 \times 10^{22}$
corresponding τ_p	0	$1.24 \times 10^{-5} - 3.3$
q	0	1.1-4.5
kT_max (keV)	0.01-0.2	0.01-0.8
r_max (Schwarzschild radii)	5-100	10-100

Table 4.2: The range of parameters used in HEART for the fitting of observed Cyg X-1 data.

electrons are modelled, with n_e = 2.2×10^{22} (see equation 2.3), equivalent to a Thomson optical depth of $\tau_{th} = 2.2$ along the radius, and temperature kT_e = 49.6 keV, producing a photon index of 1.75. The seed photons have a maximum blackbody temperature of 0.08 keV (kT_max = 0.08 keV) at the inner disc radius.

The corona covers the disc fully in this model. Therefore any photons reflected by the disc are subject to the same Comptonisation as the directly injected photons. Because the optical depth is fairly high (the average number of scattering events $\sim \tau^2 \gg 1$), the scattered spectrum is almost independent of the properties of the seed photons (Sunyaev & Titarchuk, 1985), which means that a distinct reflection component is not produced in the HEART output. However, the data show evidence

XSPEC parameters	The LHS	The HSS
LineE (keV)	6.54 +/- 0.284	6.20 +/- 0.111
Sigma (keV)	6.06×10^{-4} +/- 6.12	0.972 +/- 0.532×10^{-1}
nH ($\times10^{21}$cm^{-2})	4.46 +/- 0.441×10^{-2}	4.96 +/- 0.231×10^{-2}
rel_refl	3.92 +/- 3.04	n/a
redshift	0	n/a
abund	13.0 +/- 8.77	n/a
Fe_abund	5.58×10^{-3} +/- 3.96	n/a
cosIncl	5.00×10^{-2} +/- 0.716×10^{-1}	n/a
reduced χ^2	2.1	2.0

Table 4.3: The best fit parameters of the XSPEC models used (*gaussian*, *phabs* and *reflect*).

for such a component. I model this component using the output of HEART as the input for the XSPEC reflection model *reflect* (Magdziarz & Zdziarski, 1995). I also add a Gaussian profile to model the fluorescent iron line (see table 4.3 for a list of XSPEC parameters, including the value for nH).

Because of this, and also because reprocessing and energy balance are not modelled, the HEART model spectrum is not self-consistent. Three possible scenarios may explain the need for a separate reflection component:

1. Cold matter external to the corona is reprocessing photons from the corona, for example the companion star. In Cyg X-1 the solid angle subtended by half the companion star covers approximately 5% of the 2π solid angle of the hemisphere above the disc, so in an isotropic situation 5% of emitted photons should be reflected by the companion star. This is sufficient for a possible observable effect, though it is a rough estimate.

2. The corona is not homogeneous or static, but rather lumpy and evolving, and so at times photons escape unscattered from the disc and at other times they travel through regions of even higher optical depth than modelled here. The HEART corona contains a time averaged electron distribution, which does not allow the reflected component through unscattered[1].

[1]A limited investigation into this scenario is discussed in section 3.3.1, where a corona of active

LHS parameters	HEART	DiSalvo et al. (2001)
nH ($\times 10^{21}$cm^{-2})	4.46	~ 7.0
kT_max (keV)	0.08	~ 0.12
photon index	1.75	~ 1.6
kT_e (keV)	49.6	~ 90

Table 4.4: HEART parameters compared to the best fit parameters in DiSalvo et al. (2001) for the LHS of Cyg X-1.

3. The geometry is completely different to that modelled here, such that the corona does not fully cover the disc. Parts of the disc are not obscured by the corona, and any reflected photons may escape the system without further scattering[2].

This model gives a reduced χ^2 of 2.1 in XSPEC, and the best fit is shown in figure 4.8 with the $\Delta\chi$ deviation plotted in figure 4.9. The best fit parameters are compared to those of DiSalvo et al. (2001) in table 4.4. The parameters from DiSalvo et al. (2001) are an approximate single representation of the four models they use, as the parameters do not vary much between models. This comparison shows that HEART fits the data with the same general physical properties as DiSalvo et al. (2001). The disc size is also consistent, as the disc in HEART (extending to 3 Schwarzschild radii) is within the range found by DiSalvo et al. (2001). HEART does not really constrain this, however, as the emission from the outer disc is much weaker than that from the inner disc.

DiSalvo et al. (2001) include a second soft component which improves the fit and which I have not modelled, though HEART could model such a component either as a second blackbody or as an additional or hybrid electron population. With the fairly high reduced χ^2 obtained here it seems a sensible attempt, but I do not improve on the fit here. This is discussed further in section 4.4 after the fit to the HSS data is discussed in the following section.

regions is modelled. The reflected component is no more prominent in the active regions geometry than the homogeneous geometry, but only one example is considered. More work is required to draw any conclusions as to the validity of this scenario.

[2]This cannot be modelled by HEART and is discussed further in section 6.2

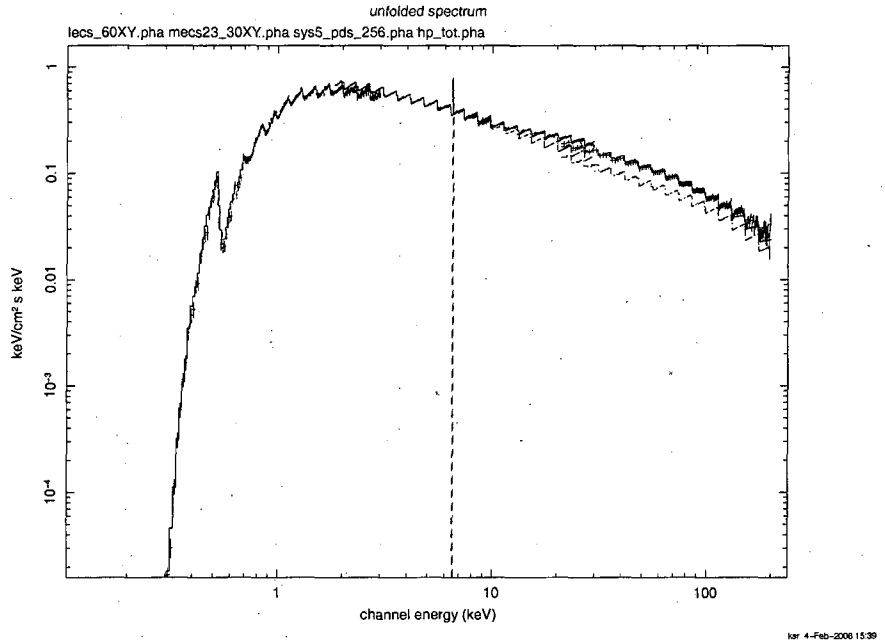

Figure 4.8: The best fit to the LHS data using the HEART model in XSPEC as well as a Gaussian iron line and the reflect model. The spectrum of the Comptonised component is shown separately in addition to the overall spectrum, and so the contribution from the reflected component is seen clearly between $\sim 10 - 200$ keV.

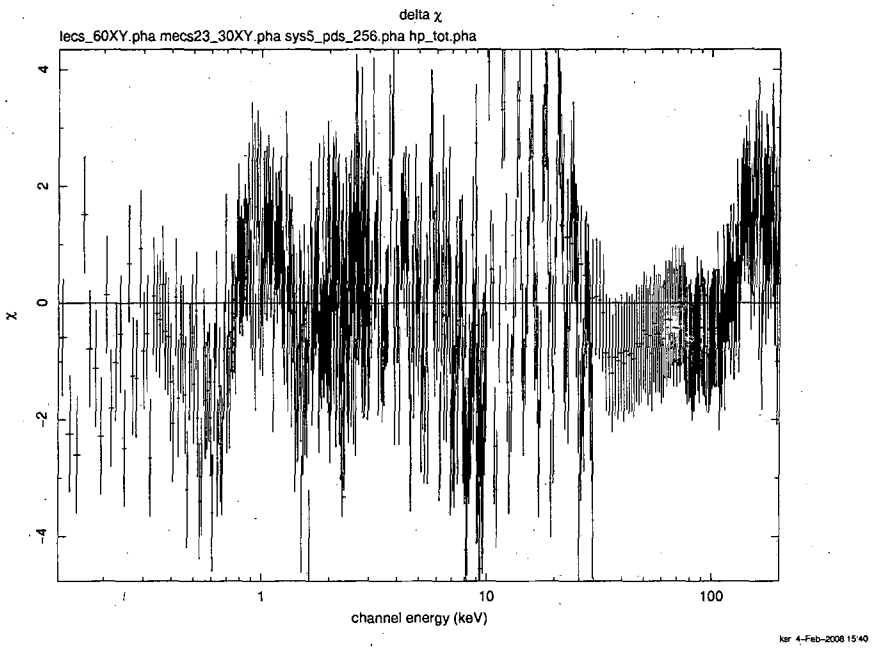

Figure 4.9: $\Delta\chi$ for the best fit to the LHS data in XSPEC.

4.3.2 Cyg X-1 in the HSS

A static distribution of only power-law electrons (i.e. n_e = 0 m^{-3}) are modelled in the HSS as there is no observable high energy cut-off, and the best fit parameters are listed in table 4.1 with the fitting range of the parameters used to determine this best fit in table 4.2. Thus the evolution of the electron distribution is not modelled and the calculation of the kinetic equation is disabled. The index of the power-law distribution is $q = 4.1$. This should give a photon index $(q + 1)/2 = 2.5$ (using the best fit values of q before rounding to 4.1) in the Thomson limit (Blumenthal & Gould, 1970), which is close to the photon index I obtain of 2.4. The density of the electron distribution is given by Q_e = 0.12 × 10^{22} m^{-3} (Q_e is n_e in equation 2.4), giving a radial optical depth of $\tau_p = 0.12$. The blackbody emission from the disc dominates with a maximum temperature of kT_max = 0.39 keV at 3 Schwarzschild radii. The disc extends in to the ISCO at 3 Schwarzschild radii, which is consistent with the findings of Frontera et al. (2001), and extends out to 100 Schwarzschild radii. As explained in section 4.3.1, I cannot constrain the size of the disc.

Since the optical depth is much smaller in this case than in the LHS, HEART is used to model the reflected component, so there is no need to add it separately in XSPEC. This does not make the model self-consistent, however, as absorption in the disc is not modelled, similarly to the fit to the LHS. More details of the reflected component modelled by HEART is given in section 3.1.3 where the reflected component is also shown separately in figure 3.1. A Gaussian is, added to represent the iron line. The best fit values for nH and the Gaussian are listed in table 4.3. This fit gives a reduced $\chi^2 = 2.0$ in XSPEC and is shown in figure 4.10 with the $\Delta\chi$ deviation plotted in figure 4.11.

Frontera et al. (2001) fit this data using the model of Coppi (1992), where a steady-state hybrid electron distribution is used. HEART produces the same general features as Frontera et al. (2001) with similar values for the maximum disc temperature, photon index and galactic absorption. These parameters are compared in table 4.5. As for the LHS, it is possible that using a hybrid electron distribution in

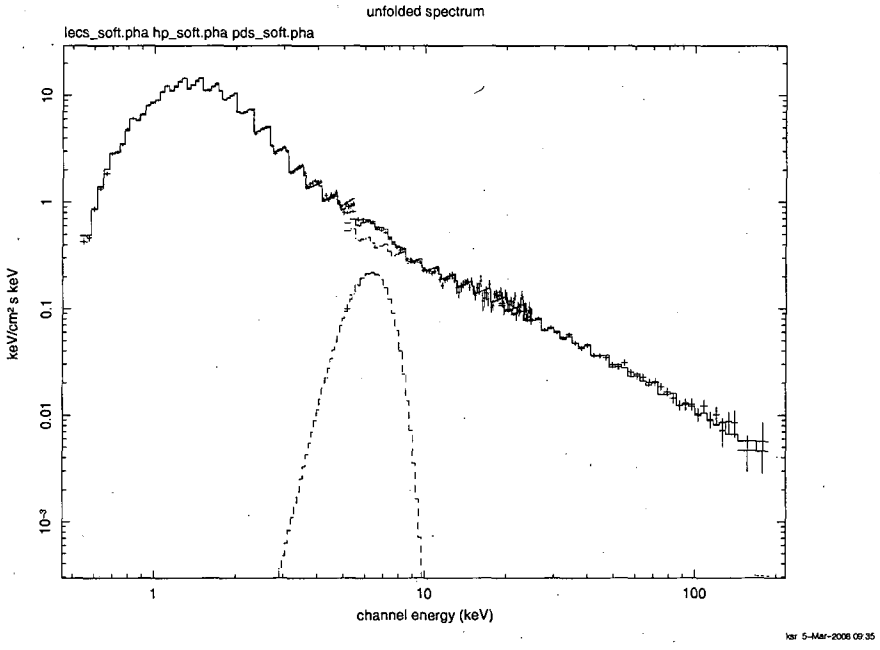

Figure 4.10: The best fit to the HSS data using the HEART model in XSPEC as well as a Gaussian iron line.

HSS parameters	HEART	Frontera et al. (2001)
nH ($\times 10^{21}$ cm^{-2})	4.96	6.0
kT_max (keV)	0.39	0.37
Γ (photon index)	2.4	2.8

Table 4.5: The best fit HEART parameter values for the HSS compared to the best fit values found by Frontera et al. (2001).

HEART would produce a better fit, but I do not attempt that approach here. This is discussed further in section 4.4.

4.4 Conclusions to the testing of HEART

I have now tested HEART by comparing it to the analytic model by Titarchuk (1994) and using it to fit Cyg X-1 data, and the results are mixed. HEART agrees well with *compTT* for $y_{NR} \lesssim 3$, and it agrees reasonably for $y_R \gtrsim 15$ when directionality is included. HEART fits the Cyg X-1 data reasonably within these limited boundaries in its most basic form, where electron evolution and reprocessing are not modelled.

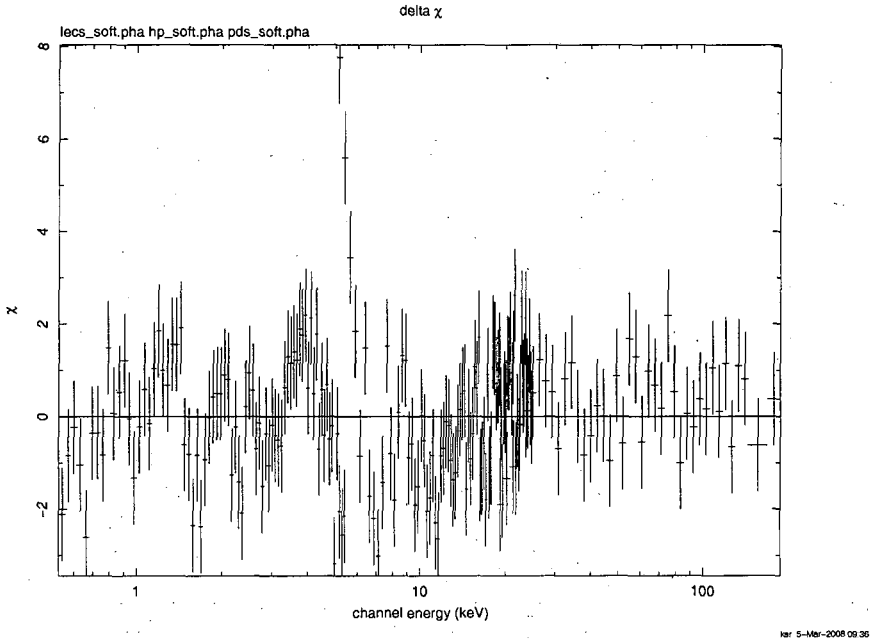

Figure 4.11: $\Delta\chi$ for the best fit to the HSS data in XSPEC. The large deviation at $\sim$ 5 keV is probably due to the Gaussian not modelling the iron line accurately.

It is possible that by including the extra components described above, a second thermal electron distribution in the LHS and a hybrid electron distribution in the HSS, I would obtain considerable better reduced χ^2 fits. There are significant obstacles to doing this successfully, however, one of which is the run-time of HEART. With current computer technology HEART is too computer intensive to be used successfully for spectral fitting. A typical homogeneous run where electrons do not evolve and with sufficient resolution takes $\sim$ 6 hours on a dual 2.2 GHz Opteron processor with 6 GB memory, and 81 runs are needed for a single multiparameter fit where four parameters are varied between three values each. The number of necessary runs and multiparameter fits grows quickly when extra parameters are added. With such timescales it becomes infeasible to use HEART routinely for spectral fitting, especially as its reliable parameter range is also limited. There are several fast fitting models available which fit observational data within its error bars for a greater parameter range than that over which HEART has been shown to be valid.

Even if it were reasonable to use HEART for spectral fitting, an improved fit to the data should include energy balance and the coupling of the disc and corona through reprocessed flux in the disc. With this included, the ECorona geometry modelled by HEART in the LHS will produce a significantly different spectrum which does not fit the data, as discussed in section 6.1.

A potential strength of the cell-structure of HEART is the simultaneous modelling of the photon and electron energy distributions evolving in time, making it suitable for modelling variability. Few other models are available which model spectra in addition to their evolution in time, and variability models are less dependent on very accurate spectra. HEART may therefore be better suited to modelling variability, and it is better to focus on investigating this feature than attempting to obtain perfect fits to the Cyg X-1 data above with a model which cannot practically be used for routine spectral fitting. The above tests show that HEART models the general spectral features sufficiently well within the parameter boundaries $y_{NR} \lesssim 3$ and $y_R \gtrsim 15$ in static situations, and it may be possible to extend HEART to model spectral evolution in time within these boundaries. This is investigated in chapter 5 and discussed further in chapter 6.

Chapter 5

Using HEART to model dynamic systems

On testing HEART in the previous chapter I find that HEART is unsuitable for spectral fitting, but may have potential for modelling dynamic systems, thus combining spectral and temporal information. Simultaneous modelling of spectra and their evolution in time is often not included in other models of the physical processes which dominate the spectra from X-ray binaries and AGN. For example, the evolution of the electron distribution is not modelled in *compTT*, and it is therefore not possible to model the effect of the radiative processes on the electron distribution and the consequent effect on the spectrum. In principle, electron evolution can be modelled in the cell-based structure of HEART, though there are problems with this in the current form of HEART. This is discussed in chapter 6. Combining all available data, both spectral and temporal, is important in furthering our understanding of these systems, as discussed in the introduction (chapter 1).

While the structure of HEART allows for the modelling of evolving systems, as the evolution of the electron and photon distributions is modelled in every timestep, HEART is not immediately capable of modelling interesting dynamic situations. The version of HEART described in chapter 2 does not, for example, allow parameters to change with time. Thus only the evolution until a steady state is reached, with

a single parameter set, can be modelled, after which the simulation remains in equilibrium and the output spectrum remains unchanged.

For example, if state transitions are to be modelled, the physical parameters must be allowed to change. The disc may cool and/or recede as a transition is made from the HSS to the LHS, and the corona may become denser with a greater proportion of thermal electrons than in the HSS. In order to model this physical evolution of the system, the physical parameters must also evolve.

In this chapter I describe the necessary modifications of HEART to enable the modelling of evolving systems. Two dynamic systems are then modelled, a state transition from the LHS to the HSS in a BHXB and an X-ray burst on the surface of a neutron star, with the aim of testing these additions, and investigating the capability of HEART for dynamic modelling.

5.1 Modifications to the code

In order to study the variability of a system evolving in time, the spectral output previously produced by HEART is insufficient. A more flexible form of output is necessary in order to produce, for example, lightcurves and hardness-intensity diagrams (HIDs). The numerical spectral data and data describing the electron distribution in every timestep is therefore output to a file. This file can then be imported into a plotting program while maintaining full flexibility of producing different plots.

For example, a simple Matlab program imports HEART data and produces a lightcurve by summing the spectrum from each timestep over energy to produce a single bolometric flux per timestep. It is then easy to only plot portions of the lightcurve. For example the part of the lightcurve which is created before the system has 'settled' (as discussed in section 4.1) is usually of no physical interest and is best not included. The lightcurve shown in figure 3.9 is an example of a lightcurve produced in this way. A lightcurve can easily be modified to sum only over certain energy ranges to produce separate hard and soft lightcurves, as is done in section

5.3.

HIDs are plotted similarly. The output flux in given energy ranges is summed for each timestep, producing a value for the soft flux, the hard flux and the total flux for every timestep. The hardness ratio, (hard flux)/(soft flux), is then plotted versus the total flux for every timestep, and so the system's evolution on the HID is displayed. Examples of HIDs with different energy ranges, produced in this way, are shown in figures 5.3 and 5.4.

5.1.1 Changing parameter values during a simulation

The parameters which describe the injected electron distribution (see section 2.3) were previously set at the start of a simulation, where the electron distribution was calculated and then used throughout. In order to change the parameter values describing the injected electron distribution as the simulation progresses, I create a function within the time loop which recalculates the injected electron distribution at the start of every timestep, if required. Distinct individual electron distribution parameters are already stored within each cell (see section 3.3), so, in addition to initially injecting different electron distributions into each cell, an evolving, inhomogeneous electron corona can be modelled by specifying a different parameter evolution path in each cell.

These parameters describe the evolution of the injected electron distribution from one timestep to another. Electron distributions also evolve during a timestep, however, according to the kinetic equation (equation 2.2). These two types of evolution combine as follows. The injected electron distribution changes instantaneously between timesteps according to user-specified parameter changes, providing a different source term in the kinetic equation in each timestep. The electron distribution in a cell then evolves according to the kinetic equation during a timestep, with this new source term. If the injected electron distribution is then kept constant, the calculation of the kinetic equation causes the electron distribution in each cell to evolve to a new steady state. Thus the evolution of the actual electron distribution in each

cell occurs more slowly than the changes in the injected electron distribution. This allows the evolution between two spectra, produced by two distinct steady-state electron distributions, to be modelled[1]. Alternatively, if the electron distribution does not evolve during each timestep, i.e. the calculation of the kinetic equation is disabled, then the electron distribution in each cell is changed instantaneously to a different distribution.

The flexibility in changing the electron parameters is great. It is, for example, possible to only recalculate the injected electron distribution in certain timesteps. This can be used to allow the system to reach a steady state before the parameters start varying, producing a more physical simulation. The system may then reach a second steady state before introducing further parameter changes.

There is also little limitation in the way in which the electron parameters may change. The changes may depend on time, for example the electron temperature may be proportional to the timestep. So in timestep 2 the temperature may equal 2*kT_e, whereas in timestep 3 the temperature may be 3*kT_e, where kT_e is an initially specified electron temperature. Alternatively, the electron parameters may follow a pre-specified pattern. The temperature may, for example, increase by 0.1 keV in one timestep and by 0.01 keV in the next. Single, instantaneous changes are also possible. The injected electron distribution in each cell is treated individually, so there is no restriction for the parameter changes to be the same in all cells.

An example is given in section 5.2, where the power-law component of the injected electrons decreases linearly over 31 timesteps (timesteps 100-131), while the thermal component increases linearly over only 5 timesteps (timesteps 127-131). This is done after allowing the system to reach a steady state for the first 100 timesteps.

Output spectra depend on the injected seed photon distribution as well as the injected electron distribution. The disc must be allowed to cool to evolve from the HSS to the LHS. To implement the evolution of the disc temperature in HEART,

[1]As electron heating is not modelled, the steady-state electron distributions are not physical. See chapter 6 for more details.

a feature added when expanding the code to include reflection and reprocessing in the disc (see section 3.1) is used. The seed photon distribution can be recalculated in every timestep for disc cells, if the photons absorbed by the disc change the disc temperature locally. This is not modelled due to the problems it causes, which are discussed in chapter 6, but here this recalculation is used whenever a new temperature of the disc is required. Equations 2.35 and 2.36 are used for this recalculation, so only the maximum temperature of the disc, the value of kT_max (see section 2.3), can be changed.

For example, in the state transition from the HSS to the LHS, the maximum disc temperature, kT_max, is decreased by 0.01 keV per timestep from 0.39 keV in the HSS to 0.08 keV in the LHS. This change starts at timestep 100, when a steady state has been reached, and kT_max remains at 0.08 keV once this temperature is reached. The parameter kT_max can be varied at any timestep(s) and between any values required in any specified manner.

It is not currently possible to change the size, or the inner and outer radii, of the accretion disc during a simulation, or to dictate local changes to the disc temperature. The local disc temperature is always determined by the temperature at the inner radius, kT_max, and local absorption of photons. Such changes require more modifications to HEART, but the framework is written and so these additional features should be easily included if required.

Such modifications could be used to model the scenario described by the ADAF model during state transitions. In section 5.2, however, the disc temperature, rather than the inner disc radius, is changed to model a state transition. This provides starting and end points for the state transition, as they can be based on the HEART model fits to data from Cyg X-1 in the HSS and the LHS in section 4.3. The disc extends in to 3 Schwarzschild radii in these fits in both states.

One other modification to the injected seed photon distribution is made, in order to simulate an X-ray burst in section 5.3. A second blackbody or multi-colour disc distribution may be added during a given set of timesteps. The parameters

of this second seed photon distribution, i.e. the maximum temperature, the inner and the outer radii, are specified in the parameter file similarly to the original seed photon distribution (see section 2.3). An additional normalisation parameter, factor_2, is added, and its purpose is discussed later in section 5.3. The two seed photon distributions are then added in the relevant timesteps and treated as one, reverting back to the original seed photon distribution if required.

It is unnecessary to allow any other parameters to vary during simulations for the purposes of the current work. There is no need to vary non-physical parameters, for example the maximum and minimum photon and electron energy modelled, and it is unphysical to vary some parameters, for example the mass of the source and the distance from the observer to the source. Bremsstrahlung and Coulomb interactions are not determined by user-specified parameters, but vary as the electron and photon distributions vary. The only other parameter which it might be useful to vary is the magnetic field strength, but as HEART has yet to be applied to any situation where the magnetic field is considered, this is not included here.

5.2 Modelling a state transition

To demonstrate the capability of HEART to combine spectral and temporal modelling, and to test the features described above, a state transition from the HSS to the LHS is modelled. HEART is in its early stages of temporal modelling, and so no attempt is made to model a specific observed state transition, with spectral and temporal fitting throughout. Such an exercise could, in future, aid in distinguishing between different suggested geometries before, during and after state transitions, by comparing both spectral and temporal model information with observed data. Understanding which physical parameters must change, and in what way, to initiate a state transition could aid models for the driving mechanism of state transitions, something which is still a matter of debate. This is, however, considerably beyond the scope of the current work, where the evaluation of the capability of HEART to do such modelling is the focus.

HEART parameters	value
n_e (m^{-3})	7×10^{22}
kT_e (keV)	30.0
equivalent τ_{th}	2.1
Q_e (m^{-3})	0.6×10^{22}
equivalent τ_p	0.6
q	3.5
t_inj	0.0
t_esc t_cross^{-1}	0.3

Table 5.1: The electron parameters used to model the steady-state HSS and LHS spectra with the calculation of the kinetic equation included. This gives a very similar scenario to the best fit static models in section 4.3. Electrons are continuously injected, and may escape in the length of time it takes light to cross 0.3 times the width of the corona (equivalent to the length of 7.2 cells). Definitions of the parameters are given in section 2.3.

The injected seed photon and electron distributions are changed to simulate a state transition. A model based on the best fit HEART parameters to the HSS data is used initially, and the parameters are then gradually changed to those of a model based on the best fit HEART parameters of the LHS data. These best fit parameters are listed in table 4.1, but can not be used directly. The evolution of the electron distribution as calculated by the kinetic equation (equation 2.2) is disabled in the HEART best fits to the HSS and LHS observational data in section 4.3. As an evolving system is modelled here, electron evolution must be included, so new steady-state HEART models describing the HSS and LHS data are used, which include the evolution of the electron distribution as calculated by the kinetic equation. Thus here the electron density parameter in equations 2.3 and 2.4, n_γ, refers to the electron density injected per unit time. Electron evolution is not treated in a physical way in HEART, however, as the only way of heating electrons is by injecting more high-energy electrons, and the only way of preventing this from causing an extremely high optical depth is by removing electrons from the system. The parameters given in table 5.1 are therefore not very meaningful, as they do not describe the steady-state electron distribution. This problem is discussed in more detail in chapter 6, and including the calculation of the kinetic equation here, and

thus the evolution of electrons, should be seen as a test of a simple implementation of electron evolution in a dynamic simulation.

The steady-state models are very similar to the static ones of section 4.3, as they are set up to be, with only the electron parameters being different[2]. The new electron parameters are listed in table 5.1, but, as mentioned before, these do not describe the steady-state electron distribution and are not physically meaningful. The spectra produced by the static models from chapter 4 and the steady-state models presented here, i.e. with and without the calculation of the kinetic equation, are extremely similar, so no more detail is included here.

As no direct transition was ever made by Cyg X-1 from the HSS observed data to the LHS observed data used in section 4.3, this is not a simulation of a real transition. Instead, the models describing the data in section 4.3 are used as typical HSS and LHS spectra, and a typical state transition is modelled, for the purposes of this exercise. The progress of the state transition is plotted as a lightcurve and as a HID.

So, initially the HSS is modelled, and the system reaches a steady state after 100 timesteps. The disc then decreases in temperature from 0.39 keV in the HSS to 0.08 keV in the LHS, and, in this example, is set to decrease by 0.01 keV per timestep. Hence the maximum disc temperature reaches the LHS value in 31 timesteps. The electron distribution in the HSS is a pure power-law distribution, while in the LHS it is a pure thermal distribution. In the first 100 timesteps, while the system reaches a steady state, the injected electron distribution is the pure power-law distribution of the HSS (see table 5.1). The density of this injected distribution then decreases linearly to 0 over the same 31 timesteps over which the disc temperature decreases. Towards the end of this decrease, a thermal electron distribution is injected. This is the thermal electron distribution of the LHS (see table 5.1), and its density increases linearly from 0 to the LHS value over timesteps 127-131. A plot of how the injected

[2]The disc is also slightly smaller than in section 4.3, with an outer radius of 85 Schwarzschild radii. This makes no significant difference, except that it gives a marginally better fit to the data in XSPEC when the kinetic equation is not disabled.

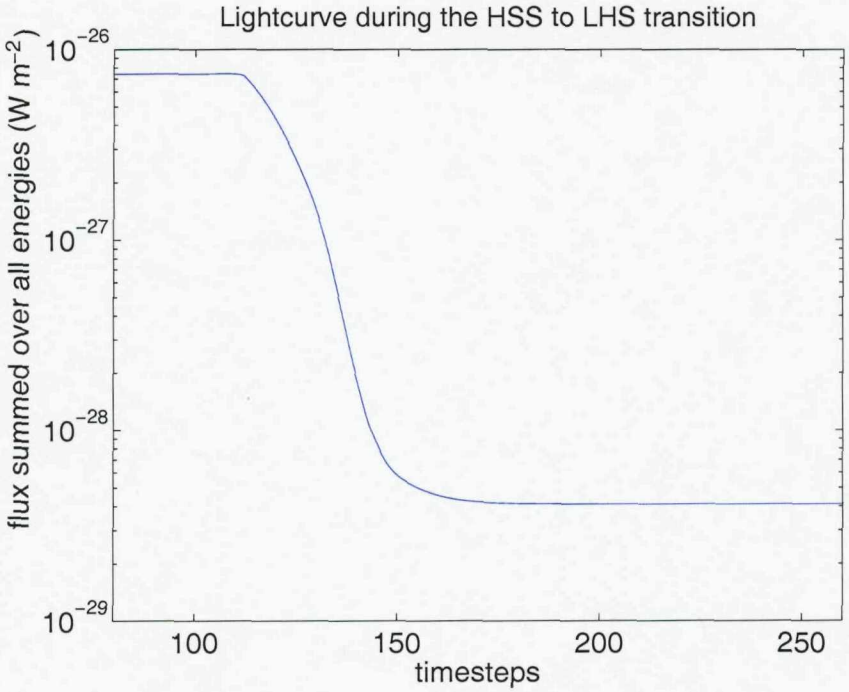

Figure 5.1: A lightcurve showing a state transition from the HSS to the LHS.

density of the thermal and power-law electron distributions vary over timesteps 100-131 is shown in figure 5.5, where 'thermal 1' is relevant to this example. The variation of the disc temperature is also shown in the same figure. In timestep 131 and thereafter the parameters of the system are identical to those of the LHS. A steady state is reached in the LHS after another $\sim$ 50 timesteps.

The simulated state transition is illustrated in figures 5.1, 5.2, 5.3 and 5.4 by the lightcurve, a few spectra at different times showing the evolution between the states and two HIDs. The energy ranges used in Fender et al. (2004) are used in the first HID, whereas the second HID uses all modelled energies with the boundary between the soft and the hard flux set to 4.5 keV. This is where the soft bump becomes a hard power-law tail in the HSS. Comparing the two shows that the general movement of the source in the HID is fairly independent of the exact energy ranges chosen. Both HIDs show similar evolution during the state transition to HIDs of observational data. Hereafter the energy ranges from Fender et al. (2004) are used, for better

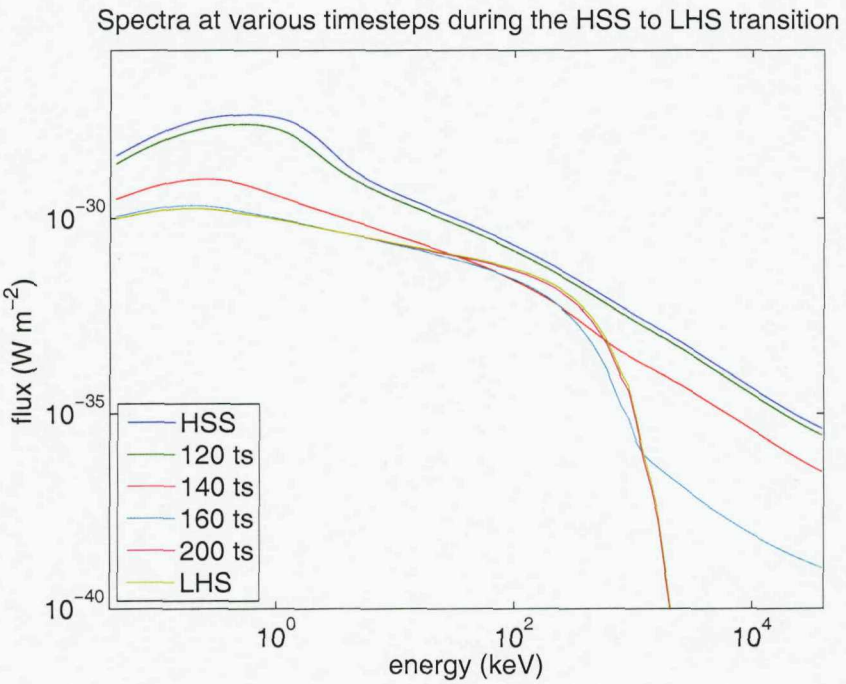

Figure 5.2: Spectra showing the evolution from the HSS to the LHS. The spectrum evolves from that labelled HSS, through the spectra at 120, 140, 160 and 200 timesteps and finally reaches the LHS spectrum.

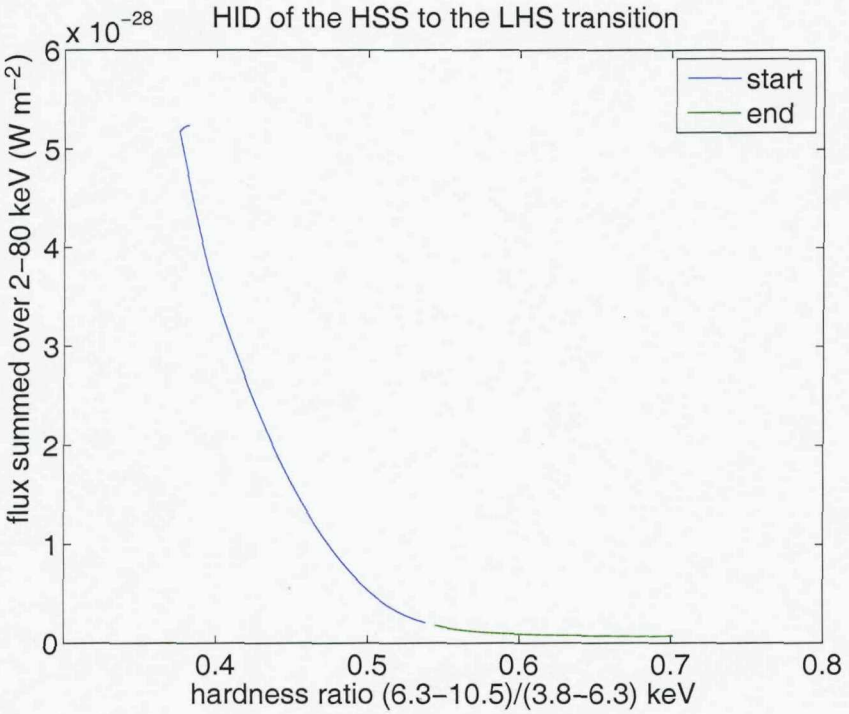

Figure 5.3: A HID, using the energy ranges from Fender et al. (2004), showing the evolution from the HSS to the LHS. The shape is similar to that of observed HIDs during a HSS to LHS transition. The HID is given in two colours so that the progression of the source on the diagram can be followed. The HSS is at the top left hand corner, on the curve labelled 'start'. The source progresses down the blue curve through to the green curve during the state transition. This progression ends at the bottom right hand corner, i.e. the end of the green curve labelled 'end', which represents the LHS. This convention is used in all the HIDs plotted here.

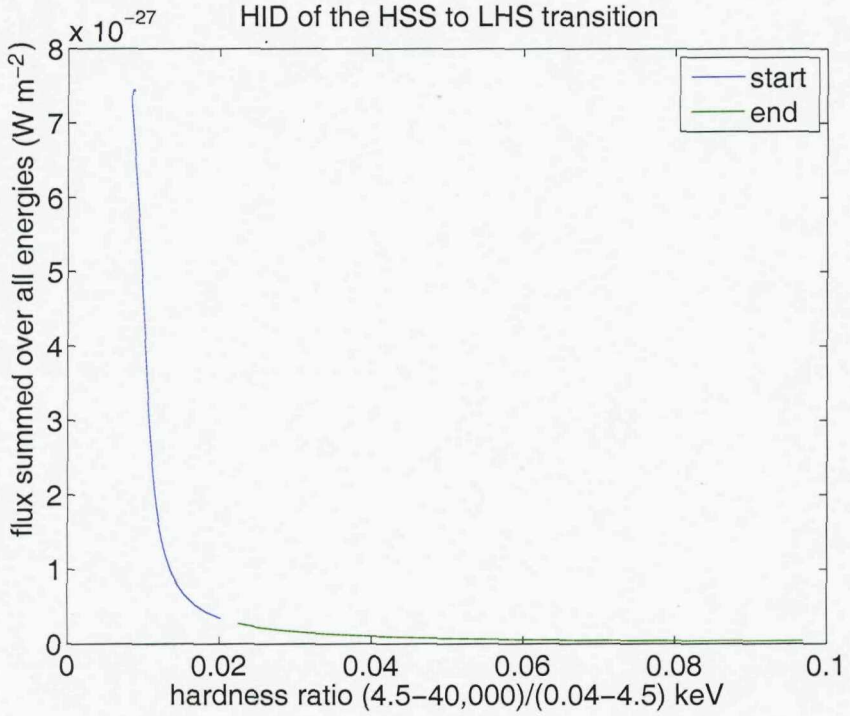

Figure 5.4: A HID, using all the modelled data, showing the evolution from the HSS to the LHS. The general movement of the source on the HID during the state transition does not depend significantly on the energy ranges chosen, as is seen by comparing this figure to figure 5.3 where different energy ranges are used. The labels are defined under figure 5.3.

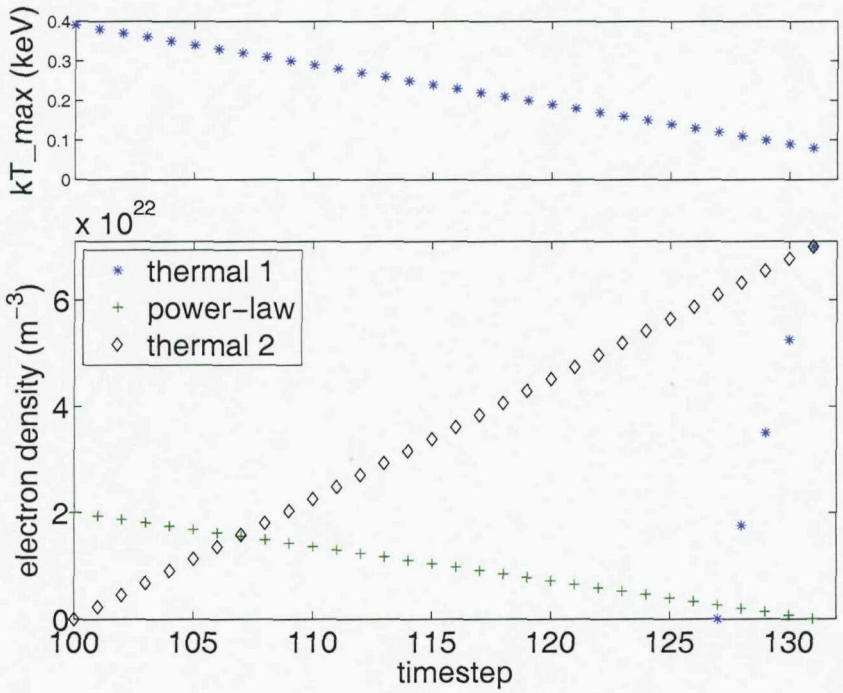

Figure 5.5: How the density of the injected thermal and power-law electron distributions vary during the modelled state transition. Thermal 1 refers to the thermal electron distribution used for the state transition, while thermal 2 demonstrates increasing the density of the thermal electron distribution over the same timesteps as the power-law distribution is decreased. This is used in figure 5.6.

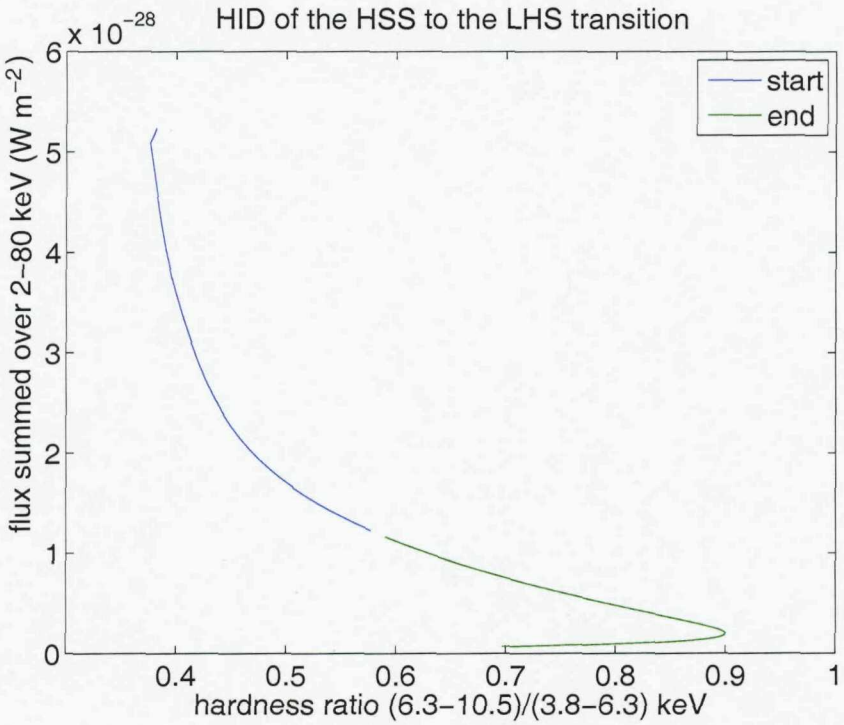

Figure 5.6: A HID for the HSS to LHS transition where the power-law electron distribution is decreased, and the thermal electron distribution is increased, over the same 31 timesteps as the disc temperature is changed. The shape does not agree with observations. The labels are defined under figure 5.3.

comparisons to observable scenarios.

This simulation does not last as long as a real state transition. The complete transition takes place in less than 100 timesteps, which is equivalent to $\sim$ 0.04 seconds. It is, however, not currently possible to run HEART over realistic state transition timescales, and this is discussed further in section 5.4.

The reason for delaying the injection of thermal electrons is most easily explained by considering the HID produced if the injection of the thermal electrons is not delayed. Such a HID is shown in figure 5.6. Here the seed photon injection decreases due to a decrease of the maximum disc temperature from 0.39 keV to a maximum disc temperature of 0.08 keV in steps of 0.01 keV over 31 timesteps, and the power-law electron distribution decreases linearly over the same timesteps, as above. In this case, however, the injected thermal electron distribution also increases linearly,

from 0 to 7×10^{22} m^{-3}, over the same 31 timesteps, as shown in figure 5.5 under 'thermal 2'. It can be seen in the HID that the source initially follows a path similar to that of observed state transitions, and figures 5.3 and 5.4, but finishes off by softening again.

Initially the source hardens as the luminosity decreases, but a state is reached in the intermediate steps, while the injected power-law electron distribution decreases and the thermal electron distribution increases, where the overall electron distribution becomes significantly denser than during either the HSS or the LHS. A blackbody bump is created by the electron distribution at high energies, making the spectrum considerably harder than in the LHS. As the overall electron distribution decreases to the thermal one of the LHS, this bump disappears, and the source softens to reach the LHS spectrum, though the final LHS spectrum is harder than the initial HSS spectrum. The intermediate spectrum reached in this simulation, which is harder than the LHS, is very transient, and may not be visible in observational data if it does exist. As nothing like it has been observed, however, the delayed injection of the thermal electron distribution is used.

A linear decrease of the power-law electron distribution simultaneously with a linear increase in the thermal electron distribution is a simple first attempt, with the more successful delayed increase of the thermal electron distribution being a similar, simple attempt of modelling the HSS to LHS transition. It is possible that other combinations of the rate of decreasing the power-law electron distribution and increasing the thermal electron distribution reproduce the observed HID equally well. It may be possible to constrain this by studying intermediate spectra, but the main result here is that HEART can reproduce the observed shape of the HID during a state transition from the HSS to the LHS by changing the disc temperature and the injected electron distribution, even without changing the size of the disc, during a simulation.

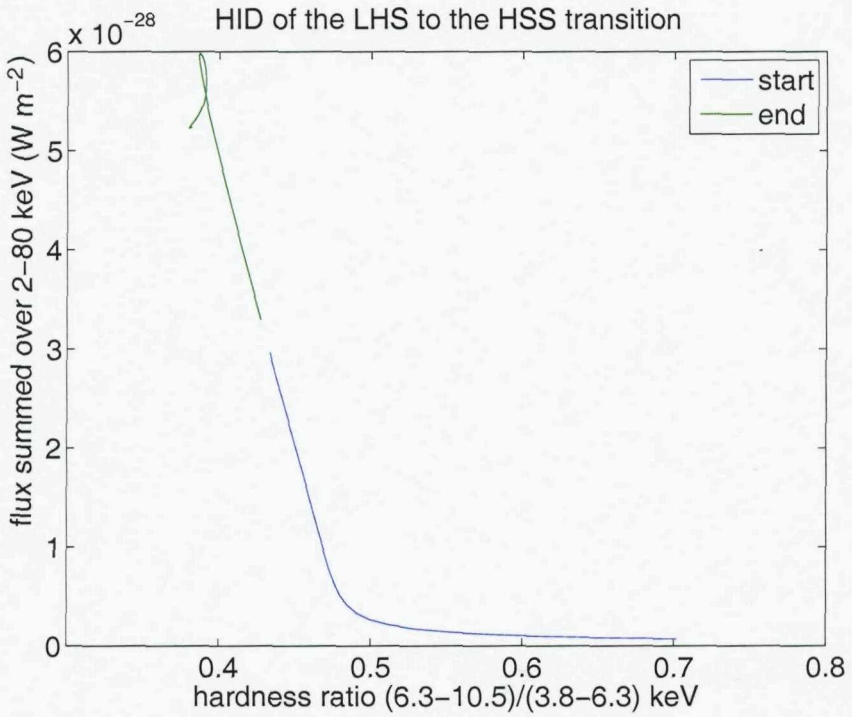

Figure 5.7: A HID for the transition from the LHS to the HSS. This does not reproduce the typical observed shape of an increase in luminosity while the spectrum remains hard, and then a softening to the HSS at approximately constant luminosity. The labels are defined under figure 5.3.

5.2.1 A state transition from the LHS to the HSS

It should be possible to model a state transition from the LHS to the HSS as well, to complete the movement of the source in the HID during a complete outburst. This is not, however, trivial, as it is necessary to increase the luminosity of the LHS without changing the spectral shape before modelling the state transition. If the above procedure used in the HSS to LHS state transition is simply reversed, with the maximum disc temperature increasing from 0.08 to 0.39 in steps of 0.01 keV for 31 timesteps, and the thermal electron distribution increasing linearly and the power-law electron distribution decreasing linearly over the same 31 timesteps, the HID in figure 5.7 is produced. Instead of increasing in luminosity and then softening, an initial softening occurs, before the increase in luminosity. Changing the timing and rates of the evolving electron distribution does not produce the desired result here, as it did above in the opposite state transition. As soon as the disc temperature increases, the spectrum softens.

An investigation into how to increase the luminosity of the LHS without changing the spectral shape is necessary, perhaps by increasing the area of the accretion disc providing the seed photons while keeping the disc temperature roughly the same. Considering an ADAF geometry, the area of the inner disc in the LHS is much larger than that modelled here, as the inner disc is further from the compact object. The inner disc in HEART is at 3 Schwarzschild radii, with the contribution from seed photons from the outer disc being negligible as they are considerably colder. If a more luminous LHS steady-state spectrum were modelled, perhaps by modelling a larger inner disc radius, the state transition from the LHS to the HSS could easily be modelled. The necessary increase in luminosity while remaining in the LHS on the right-hand side of the HID would still have to be modelled, however, but in a considerably different geometry where the disc is much further from the compact object throughout the LHS.

Such an investigation requires significantly more work and is not done here. The current aim is to demonstrate how HEART models the evolution between two

distinct steady states, which is done above for a state transition. HEART is also successfully used, in conjunction with Matlab, to produce lightcurves, HIDs which agree with observations and spectra throughout the evolution from a HSS to a LHS.

5.3 An X-ray burst in Aql X-1

To further investigate the capabilities of HEART to model dynamic systems, a very different evolving system is modelled. An X-ray burst on the surface of a neutron star is simulated here. The similarities between neutron star and black hole X-ray binaries (BHXBs), and the applicability of models describing BHXBs to neutron star X-ray binaries, are discussed in the introduction (section 1.3). Although both systems can be modelled by HEART, the focus here has been on BHXBs. In this section, however, HEART is applied to describe the behaviour of Aql X-1, a low mass X-ray binary (LMXB) where the compact object is a neutron star, during a type 1 X-ray burst, referred to here as an X-ray burst.

A review of X-ray bursts is given in Lewin et al. (1993), and a brief summary is included here. X-ray bursts have been observed in approximately 40 neutron star LMXBs, and are most likely caused by a thermonuclear flash on the surface of the accreting neutron star, hence they are not observed in BHXBs. Hydrogen and helium accrete onto the surface of the neutron star from the donor star, and the weight of the accreted matter on the surface of the neutron star builds up until there is sufficient pressure for fusion of hydrogen and helium into heavier nuclei to occur. This is likely to be an explosive event, and the energy emitted, in the form of gamma rays, kinetic energy and neutrinos, eventually emerges from the surface of the neutron star in the form of X-rays, and is observed as an X-ray burst. Such bursts typically last only a few seconds to minutes, but can in rare cases last up to $\sim$ 25 minutes.

A typical spectrum of an X-ray burst is similar to that of a blackbody spectrum, though a hard tail, possibly from Comptonisation, has also been observed in some burst spectra. In general, however, the time-dependent X-ray burst spectra are well

modelled by a blackbody spectrum (Lewin et al., 1993).

5.3.1 Modelling the X-ray burst

Maccarone & Coppi (2003) present RXTE data from Aql X-1, observed during an outburst in May/June 1999. An X-ray burst was observed during Observation 40047-01-01-01, which lasted from 22:24:23 to 23:04:15 on May 19th 1999. An increase in the soft lightcurve (15-30 keV) of $\sim$ 20%, simultaneously with a decrease in the hard lightcurve (30-60 keV) by a factor $\sim$ 2, is the main signature of this burst and is shown in figure 5.8. The spectral data is not well constrained, with the high energy data having particularly large errors associated with them. This observation is also integrated over a time period when the source is undergoing substantial, systematic variability due to the burst, and so the integrated spectrum is probably not representative of a single physical situation in the source. Therefore, only the general features of the spectra before (Observation 40047-01-01-00) and during the burst are modelled. The evolution between these spectra then provides a lightcurve of the source as the burst occurs, and the soft and hard lightcurves are compared.

Steady-state HEART parameters are first found to model the general features of the spectral data before the burst. These parameters are listed in table 5.2 and are used throughout this section (see section 2.3 for definitions of each parameter). Electron evolution is modelled, so the calculation of the kinetic equation is enabled, but as in the previous section, section 5.2, this not modelled in a physical way and is used as a simple test of modelling evolution in HEART. Thus the electron parameters given are not physically meaningful and do not apply to the steady-state electron distribution. See chapter 6 for a more detailed discussion. The range of parameters used to obtain this fit is listed in table 5.3.

The distance to Aql X-1, and the value used for nH (3.4×10^{21} cm^{-2}) whenever fits in XSPEC are referred to (the model *phabs* is used, as in section 4.3), are those used in Maccarone & Coppi (2003). The distance modelled by HEART is not important as the focus here is on the general features of the spectra, and XSPEC is

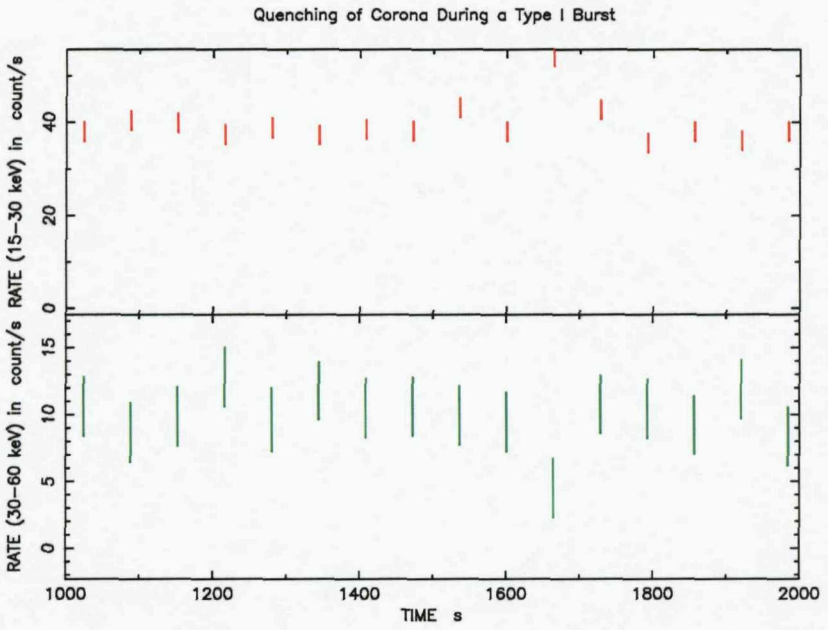

Figure 5.8: A simultaneous drop in the hard lightcurve with an increase in the soft lightcurve during an X-ray burst between 1600 and 1700 seconds. The points at 1600 and $\sim$ 1650 seconds correspond to the spectra fitted here. Figure taken from Maccarone & Coppi (2003).

HEART parameters	value
model	ECorona
nu_min (Hz)	1×10^{16}
nu_max (Hz)	5×10^{20}
gamma_min	1
gamma_max	20.0
w (m)	826,978
D (pc)	2500
M_bh ($M_\odot$)	1.4
N_H (cm^{-2})	0
B (T)	0
n_e (m^{-3})	8.7×10^{22}
equivalent radial τ_{th}	1.2
kT_e (keV)	32.0
Q_e (m^{-3})	0
q	0
t_inj	0.0
t_esc t_cross^{-1}	0.5
kT_max (keV)	0.1
r_min (Schwarzschild radii)	3
r_max (Schwarzschild radii)	13

Table 5.2: The parameters used to model the Aql X-1 data before the X-ray burst. See section 2.3 for definitions of the parameters.

HEART parameters	Before	Bursts 1, 2 and 3
kT_max (keV)	0.01 - 0.3	0.01 - 0.9
n_e (m^{-3})	2×10^{22} - 3×10^{23}	1×10^{22} - 3×10^{26}
equivalent τ_{th}	0.5 - 8.3	7.3×10^{-8} - 7.4
kT_e (keV)	5 - 150	0.1 - 30
kT_max_2 (keV)	n/a	0.1 - 2.5
factor_2	n/a	1×10^{-8} - 2.5×10^{-4}
kT_max_3 (keV)	n/a	0.6 - 2.0
factor_3	n/a	4×10^{-6} - 8×10^{-6}
r_min (Schwarzschild radii)	3	0
r_max (Schwarzschild radii)	5-15	8-15

Table 5.3: The range of parameters used to obtain the HEART models describing the general features of the data before and during the X-ray burst in Aql X-1.

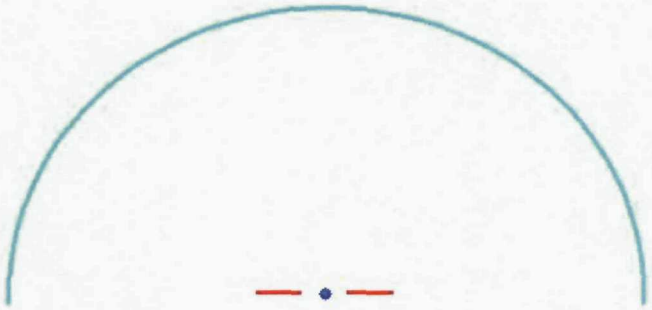

Figure 5.9: The ECorona geometry in HEART used to model the X-ray burst in Aql X-1. The red disc, previously used to model an accretion disc, is here used to model the neutron star surface. Thermal seed photons are injected from this area. Seed photons modelling the burst are injected centrally at the blue diamond. Hot electrons surround the neutron star, and are modelled within the volume delineated by the cyan line.

allowed to set the normalisation of the model when used for fitting data. A multiplicative constant also allows different normalisations for different instruments allowing for uncertainties in the absolute calibrations of individual instruments, when fits in XSPEC are referred to. The mass of Aql X-1 is assumed to be the canonical neutron star mass, as suggested by Maccarone (2003) and Lewin et al. (1993).

The modelled electron and photon energy ranges are smaller than in the work described previously, but the size of the energy bins is unchanged, and the energy ranges modelled cover a sufficiently greater energy range than the data to give equally accurate results[3]. The same number of cells as previously, a 24 cell diameter, is modelled.

Similarly to work in previous chapters, the ECorona geometry is used (a hemispherical corona above a circular disc). It would be preferential to use a slab geometry, as the surface of a neutron star is being modelled, not a central black hole. One slab, the neutron star surface, would emit seed photons while the other would act as the corona surrounding the neutron star. Such a geometry is, however, not properly tested in HEART, and so the ECorona model is used instead. By using a small

[3]Simulations of both energy ranges have been run and compared, with no detectable difference.

central disc and injecting seed photons only at the centre, the shortest escape path of each photon is identical, similarly to a slab geometry. Furthermore, including full reflection provides a similar effect to those seed photons which travel some distance parallel to the neutron star surface before escaping from the corona. The boundary layer and accretion disc are not modelled, but it is often difficult to distinguish between the emission from the neutron star surface and the disc in observed data, and the neutron star surface may inject seed photons into the corona as well as, or even instead of, the accretion disc in some geometries. The modelled geometry is not ideal, but sufficient for the current purpose of fitting the general spectral features of the data.

Compton scattering is modelled, while synchrotron radiation and bremsstrahlung are disabled to keep the model simple. Sufficiently detailed spectral fitting to determine any components from these processes is not done. The kinetic equation is calculated, with continuous injection of thermal electrons and an escape timescale of half the time taken for light to cross the corona. As mentioned before, this is not a physical way of modelling an evolving electron distribution. Ideally, reflection would be modelled over the entire surface of the neutron star. This would, however, not necessarily follow the same form as reprocessing in an accretion disc, and is currently only modelled in the disc. Here the disc is too small for reflection to make a difference to the output spectrum. Reprocessing of absorbed photons in the disc is not modelled, as is the case throughout.

Fitting the HEART spectrum produced by these parameters and settings, imported as a table model into XSPEC, gives a reduced χ^2 of 4.8. The *phabs* model is used to model the interstellar hydrogen column density and a Gaussian models the iron line. This is not a very accurate fit, but the general features are consistent with the observations (as can be seen in figure 5.10, where the steady-state HEART spectrum and observed data are shown; the other spectrum in this figure is referred to later), and accurate spectral fitting is not a current aim. The HEART model is flatter than the data at high energies, but due to the large errors associated with

HEART parameters	Burst 1	Burst 2	Burst 3
kT_max_2 (keV)	1.5	2.5	2.5
factor_2	6×10^{-7}	9×10^{-8}	8×10^{-8}
kT_max_3 (keV)	n/a	n/a	0.8
factor_3	n/a	n/a	4×10^{-6}
r_min (Schwarzschild radii)	0	0	0
r_max (Schwarzschild radii)	8	8	8
n_e (m^{-3})	7×10^{25}	5×10^{25}	5×10^{25}
equivalent τ_{th}	0.9	0.7	0.7
kT_e (keV)	0.2	0.2	0.2

Table 5.4: Three different parameter sets used to model the data during the X-ray burst in Aql X-1.

the high energy data it is still a good fit. A better overall fit is not found within the parameter ranges given in table 5.3. The maximum temperature of the seed photons in HEART, 0.1 keV, is determined by the slope of the data in the energy range 3-20 keV, but is not well constrained as the spectrum of the seed photons themselves dominate below 1 keV where no observational data is available. The corona is injected with thermal electrons at a temperature of 32 keV and has a radial optical depth of 1.2 in the steady state.

After determining parameters that describe the features of the spectrum before the burst, the same is done for the spectrum during the burst. Three such parameter sets are given in table 5.4 with the range of parameters used to obtain them given in table 5.3. The first, Burst 1, is discussed here, while the other two parameter sets are discussed in section 5.3.2.

The blackbody spectrum of the burst is injected in addition to the seed photons used to model the data before the burst (listed in table 5.2), as the localised blackbody spectrum from the burst is emitted in addition to the radiation from the overall neutron star surface. The burst is modelled as a single temperature blackbody (r_min = 0 sets the seed photons to a single temperature blackbody) of temperature 1.5 keV, which is scaled by a factor, factor_2, as the area producing the emission of the burst is much smaller than the surface area of the neutron star. As the modelled surface area of the neutron star is necessarily small due to the

geometry discussed above, it is not possible to model a sufficiently smaller area for the burst, so a normalisation factor is used instead. The actual area of the burst cannot be constrained from the observations.

The parameters describing the injected electron distribution are different in the HEART model during the burst and the HEART model before the burst (see tables 5.2 and 5.4). During the burst, the corona is injected with thermal electrons of a much lower temperature, 0.2 keV, and lower density, producing a lower radial optical depth of 0.9 (a discussion into whether it is necessary to change the injected electron distribution is given later in section 5.3.3). The general features of the steady-state spectrum predicted by HEART during the burst and the data points agree well, as is shown in figure 5.10.

Now that HEART has produced a steady-state model with the same general features as the data both before and during the burst, the evolution of the 'switching on' of the burst is modelled. After the model describing the data before the burst has reached a steady state, the second blackbody spectrum at 1.5 keV is injected in timestep 400 and remains on thereafter. The parameters describing the injected electron distribution are simultaneously changed from those listed in table 5.2 to those under Burst 1 in table 5.4. The system is then allowed to reach a steady state with the burst on. This steady state is reached in less time than the duration of a typical X-ray burst, with a steady state being reached in ~ 200 timesteps, or ~ 0.02 seconds. Only the region close to the compact object is modelled. Hence it makes sense to model the steady-state spectrum during the burst when comparing to the current data set.

Figure 5.10 shows the HEART spectra, as well as the data points, before and during the burst. Error bars are not included, as this is not a fit of the HEART spectra to the data, but rather an indication that the general features of HEART and the data are similar. The bolometric (3-190 keV), soft (15-30 keV) and hard (30-60 keV) lightcurves during this evolution are shown in figure 5.11. The soft and hard energy ranges are those used in Maccarone & Coppi (2003), with the bolometric

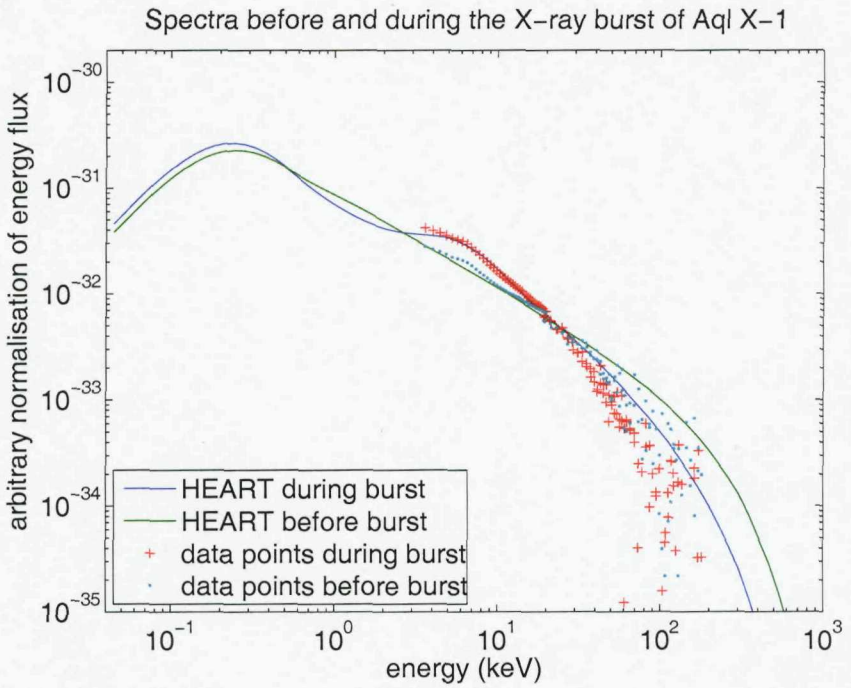

Figure 5.10: HEART spectra before and during the X-ray burst of Aql X-1 as well as the data points. The burst model shown here is Burst 1. Error bars are not included as this is not a fit of the HEART spectra to the data, but rather an indication that the general features predicted by HEART and the data are similar.

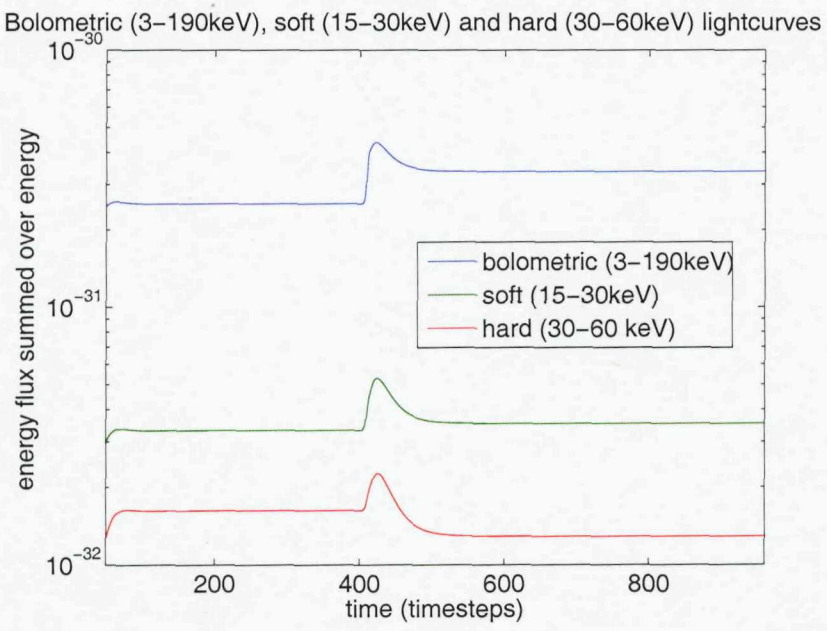

Figure 5.11: The bolometric (3-190 keV), soft (15-30 keV) and hard (30-60 keV) lightcurves during the 'switching on' of the burst. Parameter set Burst 1 is used here to model the burst. The burst occurs at timestep 400 and is on thereafter. During the burst, the hard lightcurve decreases (by a factor 1.3) simultaneously with the soft lightcurve increasing (by a factor 1.1), similarly to the lightcurves shown in figure 5.8 (Maccarone & Coppi, 2003).

energy range being the same as the energy range of the data. The simultaneous decrease in the hard lightcurve (of a factor 1.3) accompanied by an increase in the soft lightcurve (of a factor 1.1) is clearly visible. This corresponds to two data points in the observed lightcurve given in Maccarone & Coppi (2003), one before the burst and one during the burst, see figure 5.8.

The spike in the lightcurves at timestep 400 is due to the sudden release of energy stored in the corona as the additional seed photons of the burst are injected and the electron distribution reduces in temperature and density. If such a phenomenon is present in the source, it would not be visible in the observed data due to the long integration time-scales (the spike lasts for less than 100 timesteps, which is equivalent to $\sim$ 0.01 s). The instantaneous change, throughout the corona, in the injected electron distribution, is, however, unphysical, as the cause of this change takes some time to affect the whole corona, but it is not possible to constrain the short-term evolution of the electron distribution with this data.

Even though the error bars are large at high energies, HEART is systematically underestimating the high energy slope during the burst. On fitting the HEART model to data in the energy range 17-190 keV in XSPEC, a reduced χ^2 of 1.9 is obtained. A steeper slope in the HEART model would fit the data better at high energies and make the effect in the lightcurves more pronounced. This is described by the second and third models of the burst, Burst 2 and Burst 3, in the next section.

5.3.2 Modelling a hotter burst

A hotter burst gives a steeper high energy slope, which is modelled by injecting a 2.5 keV blackbody spectrum instead of the 1.5 keV blackbody spectrum described above. The injected electron distribution is thermal and has a temperature 0.2 keV, as above, but with a lower density giving a lower radial optical depth of 0.7. A list of the HEART parameters used to produce this spectrum is given in table 5.4 under Burst 2. This creates a large discrepancy between the HEART spectrum and the data at low energies, as can be seen by comparing the steady-state spectrum to

the data during the burst in figure 5.12. The high energy tail, however, produces a better fit with a reduced χ^2 of 1.15 in XSPEC when fitting only the 17 - 190 keV data.

Instead of directly modelling the evolution of the parameters describing the spectrum before the burst to those of Burst 2, an improvement is first made to the soft spectrum of the Burst 2 model. A third blackbody spectrum, with a temperature of 0.8 keV, is injected simultaneously with the burst blackbody spectrum, creating a steady-state situation during the burst which agrees better with the general features of the low-energy data. This is Burst 3, and this spectrum is also shown in figure 5.12.

This third blackbody spectrum can be viewed as the cooler edges of the burst, i.e. the third blackbody spectrum is emitted by the outer region of the burst area, or it could be emitted by the same burst, but at a later time when the burst has cooled. The hot and cooled burst would be visible in the same spectrum due to the long integration time used in the observations. Both of these scenarios are better modelled by a varying blackbody spectrum which decreases in temperature with radius (but probably not according to equation 2.36) or time, for example according to equation (3.1) in Lewin et al. (1993) discussed earlier, where the blackbody spectrum changes with time. This is, however, currently not possible in HEART.

It is also not immediately necessary to model the soft spectrum more accurately as the overall spectral features are modelled sufficiently with a third blackbody spectrum. Especially as a typical burst lasts of the order of a few seconds or minutes, and the observed spectrum is integrated over 29.9 minutes, a single physical model describing the soft data has limited validity. The slope of the hard data is more important as it determines the relative shape of the soft and hard lightcurves. This slope should, perhaps, be considered to be an upper bound to the hard emission during the burst for the same reason. The long integration time could mean that all the hard emission is from before and/or after the burst. Table 5.4 lists the parameter set Burst 3, where factor_2 is slightly lower than in Burst 2, due to

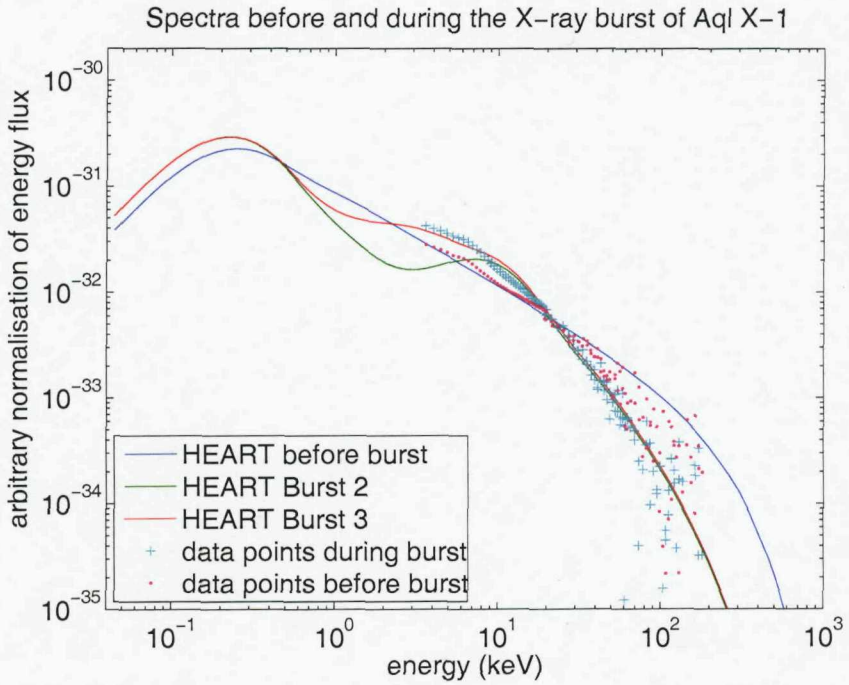

Figure 5.12: HEART spectra before and during the X-ray burst of Aql X-1, as well as the data points. Both the HEART spectrum without a third blackbody, Burst 2, and with a third injected blackbody spectrum, Burst 3, are shown. Error bars on the data points are not included, as in figure 5.10.

the added contribution from the third blackbody spectrum in Burst 3. Another normalisation constant is also added for the third blackbody spectrum.

With this improved low-energy spectrum, HEART simulates the evolution between the parameter set of the spectrum before the burst and parameter set Burst 3. The HEART steady-state spectra before and during the burst, as well as the data points, are shown in figure 5.12, and the lightcurves of the evolution between these spectra are shown in figure 5.13. The simultaneous decrease in the hard lightcurve (of a factor 1.8) with an increase in the soft lightcurve (of a factor 1.1) are more pronounced than in the previous example of a colder burst.

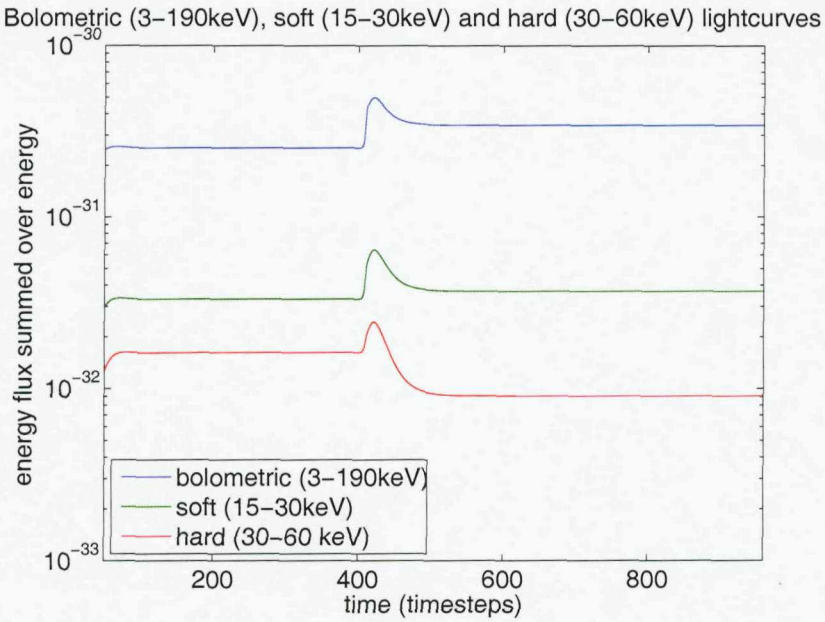

Figure 5.13: The bolometric (3-190 keV), soft (15-30 keV) and hard (30-60 keV) lightcurves during the evolution from the parameter set modelling the spectrum before the burst to the parameter set Burst 3, modelling the spectrum during the burst. The burst occurs at timestep 400 and is on thereafter. During the burst, the hard lightcurve decreases (by a factor 1.8) and the soft lightcurve increases (by a factor 1.1) in a more pronounced way than in parameter set Burst 1 in figure 5.11.

HEART parameters	Burst
kT_max_2 (keV)	0.1 - 2.5
factor_2	1×10^{-6} - 1×10^{5}
r_min (Schwarzschild radii)	0
r_max (Schwarzschild radii)	1 - 6

Table 5.5: The parameters used to model the X-ray burst in Aql X-1 without changing the injected electron distribution.

5.3.3 An unchanged injected electron distribution

In both examples considered above, the system evolves from a set of parameters that fits the general features of the data before the burst to a specified set of parameters describing the spectrum during the burst. Both the injected seed photon and electron distributions are changed. Instead, it would be interesting to simply inject a blackbody spectrum, representing the burst, to the steady-state model before the burst. Without changing any other parameters, such a simulation shows how the system reacts to a sudden change of the seed photons only. In particular, it will show whether the extra seed photons from the burst cool the corona sufficiently through Compton cooling, to produce the observed drop in the hard lightcurve, without changing the injected electron distribution. This is done for a large range of burst parameters, covering a range of temperatures and normalisations, which is listed in table 5.5. Not one of these simulations reproduces the observed decrease in the hard lightcurve. The hard spectrum during the burst is at best the same as the hard spectrum before the burst.

The steady-state spectra before and during the burst of such a simulation, where the injected electron distribution is not changed, but the distribution which is continuously injected before the burst continues to be injected throughout, are shown in figure 5.14. This example is of an identical burst to that in parameter set Burst 3, i.e. a blackbody spectrum at 2.5 keV combined with one at 0.8 keV, but without changing the electron parameters.

The bolometric (3-190 keV), soft (15-30 keV) and hard (30-60 keV) lightcurves during this evolution are shown in figure 5.15, where the burst occurs at timestep 400 and is on thereafter. Both the hard and the soft lightcurves increase during the burst. It is clear from these simulations and figures that the additional seed photons from the burst do not cool the corona sufficiently. Instead, both the soft and hard photon flux increase.

Thus, in this model, the energy injected into the electron distribution in the corona must change as the burst occurs, so the mechanism which accelerates the

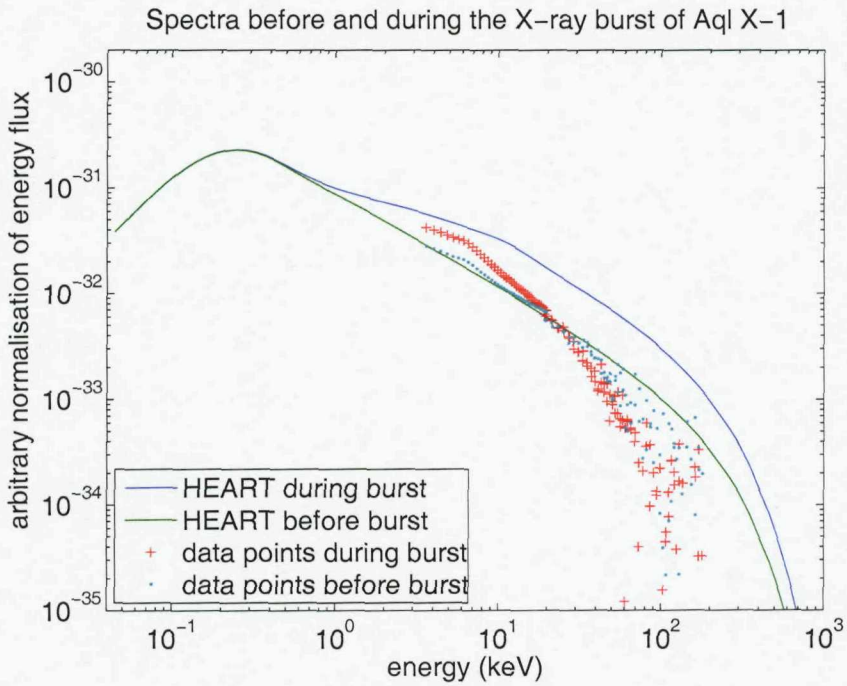

Figure 5.14: HEART spectra before and during the X-ray burst of Aql X-1 without changing the injected electron distribution, as well as the data points. Error bars are not included, as in figure 5.10.

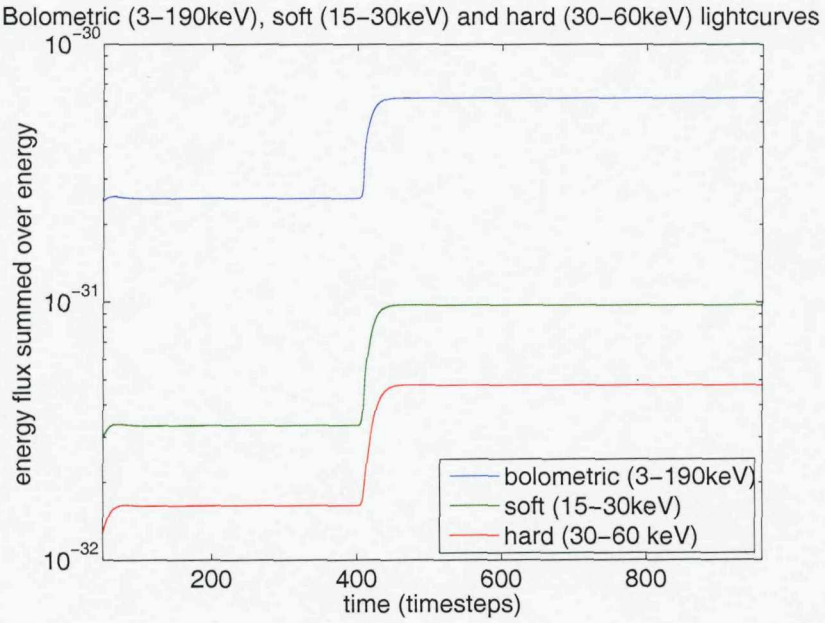

Figure 5.15: The bolometric (3-190 keV), soft (15-30 keV) and hard (30-60 keV) lightcurves, where the burst occurs at timestep 400 and is on thereafter. The injected electron distribution is not changed and the hard lightcurve does not decrease as in the previous hard lightcurves (figures 5.11 and 5.13) and the one shown in Maccarone & Coppi (2003), but increases with the soft flux instead.

electrons in the corona is affected by the burst. A limitation of the HEART model which has until now caused no problems, but which may be significant in this case, however, is the inability of HEART to model bulk electron motion. In longer, stronger bursts, it is thought that the radiation pressure from the burst causes the photosphere to expand and cool (Lewin et al., 1993), thus Compton cooling is not the only mechanism for cooling the corona. Depending on the mechanism invoked to accelerate the electrons, this acceleration may also be affected by the size of the corona. For example gravitational dissipation is less effective in parts of the corona which are further from the neutron star surface after expansion. It is not possible to determine the length of this burst from the data, and thus the extent of the expansion effect of radiation pressure in this case.

More importantly, electron evolution is not modelled in a physical way here, with an infinite energy reservoir for the electrons in the corona. This causes problems, such as preventing the corona from cooling as is the case here. This is discussed in more detail in section 6.1.

5.4 Evaluation of dynamic modelling in HEART

Two distinct evolving systems are modelled in this chapter, the state transition which occurs on comparatively long timescales, and an X-ray burst which occurs on shorter timescales. The evolution between two known steady states is successfully modelled using HEART, with every intermediate spectrum being available for inspection, as well as lightcurves and HIDs. HEART in conjunction with Matlab can even create an animation of the changing spectra during the evolution. The electron evolution is, however, unphysical, and would have to be modified for physically significant dynamic modelling.

The evolution of the 'switching on' of the X-ray burst in Aql X-1 is modelled successfully when evolving from one steady-state model before the burst to another such model during the burst. Modelling the injection of additional photons during a burst and studying the subsequent evolution of the system over time is also done,

but it is possible that the inability of HEART to model bulk electron motion is restrictive in this case, in addition to the unphysical modelling of electron evolution.

Previously discussed restrictions, in chapters 2 and 4, still apply. Only spectra in certain parameter ranges can be modelled by HEART and finding good, steady-state fits to the spectra before and after the change of the state of the modelled system is computer intensive and can be very time consuming. If intermediate spectra are also to be compared to data, more time is required. In addition, only a very basic form of HEART has been tested and used here. In particular, energy balance and reprocessing of flux in the disc have not been modelled, yet this must be included for physical consistency and has a significant effect on the emitted spectrum. It will significantly change both the spectrum of the LHS in section 5.2 and the effect the burst has on the corona in section 5.3. This is discussed in section 6.1.

The examples of evolving systems presented here, particularly the state transition, are also modelled over shorter timescales than those which are observed in several sources. As 100 timesteps is equivalent to ~ 0.04 second in the state transition model presented here, a simulation has to run for 150,000 timesteps to simulate one minute. As a 400 timestep simulation already takes ~ 8 hours to run (on a computer specified in section 4.4), it is currently not feasible to run HEART over physical timescales of minutes. Time must also be allowed for the system to reach a steady state when necessary.

There is a trade-off between run-time and accuracy, so it is possible to reduce the run-time of HEART if less accuracy is required. The run-time is approximately proportional to the number of cells along the diameter cubed, so reducing the corona from a 24 cell diameter to a 12 cell diameter decreases the run-time by a factor of 8. A 400 timestep simulation then runs in 1 hour rather than 8 hours. A 24 cell diameter is, however, the minimum number of cells giving a good approximation to the disc emission for the examples studied here. This also restricts the radial optical depth to be less than 3, if an optical depth as high as 0.5 is allowed in each cell.

Decreasing the number of energy bins that the photon and electron distributions

are discretised into also reduces the run-time, but this is only approximately linear with the product of the number of energy bins used for the electron distribution, R_e, and the number of energy bins used for the photon distribution, R_ph. Thus by reducing R_e to 57 and R_ph to 76 (from 96 in both cases) a factor of 96*96/(76*56) $\approx$ 2 is gained. Thus a 400 timestep simulation runs in $\sim$ 4 hours. This is done for the X-ray burst simulations in this section. By reducing R_e and R_ph, however, either a smaller energy range must be modelled, or the energy bins into which the electron and photon distributions are discretised become larger. The models presented here would probably not suffer from modelling slightly smaller energy ranges. The modelled energy range must, however, always be greater than the energy range of interest, as higher (or lower) energy electrons and photons can affect those in the range of interest. For example in processes such as reflection in the disc, where high energy photons are down-scattered in the outer layers of the disc to energies between $\sim$ 10 and 300 keV, photons of higher energy than the data may contribute to the shape of the spectrum energies within the range of the observed data.

HEART is perhaps better suited to modelling short term variability, on timescales of milliseconds. This is not modelled here, though the lightcurve in section 3.3.2 varies on very short timescales.

When using HEART in future, an evaluation must initially take place to determine whether the limitations of HEART allow the modelling of a given physical situation. The necessary accuracy of the model must be compatible with the limitations presented here. These limitations are discussed in more detail in the next chapter.

Chapter 6

A critical analysis of HEART

Throughout most of the work presented here, HEART is tested and used in a very basic form, with most of its features disabled. In this basic form Compton scattering is the only radiative process calculated, the corona is a homogeneous hemisphere over a circular disc with a thermal electron distribution which does not evolve, i.e. the calculation of the kinetic equation is disabled. In section 4.2, this basic form of HEART is found to agree well with the analytic model by Titarchuk (1994) for small Compton y parameters, but instead of being an improvement on the analytic model HEART is the opposite. HEART takes several hours to run compared to a few seconds for the analytic model, and HEART is valid for a more restricted parameter space, namely small Compton y parameters only.

In order for HEART to be considered for use, it must model more physical situations than the analytic model. Energy balance and the reprocessing of flux in the disc must be modelled, as well as the evolution of the electron distribution and, ideally, more radiative processes. To an extent, some of these are already implemented, but there are serious problems with all of them.

6.1 Modelling energy balance and reprocessing

Energy balance is not modelled in HEART, and the basis upon which HEART is buildt is not suitable for the inclusion of energy balance. This is most easily understood by considering two separate cases: the case where the solution to the kinetic equation is calculated and electron evolution is modelled and the case where electron evolution is disabled. Consider first the case where electron evolution is not modelled, i.e. the calculation of the kinetic equation is disabled. Thus the Comptonised spectrum, assuming that some constant electron distribution is maintained, is calculated. Any energy lost by the electrons to the photons is implicitly assumed to be replenished, as the electron distribution does not change. The amount of energy that is implicitly replenished is not restricted, i.e. there is, in effect, an infinite energy reservoir available to the cooled electrons.

Including reprocessing of photons in the disc, as described in section 3.1.2, to such a scenario causes a thermal equilibrium to be reached between the disc and corona at the electron temperature. Thermal disc photons gain energy from the electrons in the corona through inverse Compton scattering, without the electrons losing that energy. Some of those photons return to, and are absorbed by, the disc, thus heating the disc and adding more energy to the system in the form of hotter disc photons. This leads to increased hard X-rays from the corona and thus even more reprocessed energy in the disc and an even hotter disc. A cycle is created where energy is continuously added to the system until the disc photons reach the same temperature as the electrons in the corona, at which point, on average, energy is no longer transferred from the electrons to the photons and so the infinite energy reservoir is no longer being tapped. A blackbody spectrum is created from the whole system at the temperature of the electrons. As an infinite energy reservoir is not available to the electrons in X-ray binaries and AGN, this is not a good model.

Consider now the case where electron evolution is modelled, i.e. the kinetic equation is calculated in each timestep. If electron number is conserved, i.e. there is no source or sink term in the kinetic equation, and in the absence of any heating of

the electrons, the initial energy of the electron distribution is quickly transferred to the photons and radiated away, leaving a cold electron distribution. It is necessary to heat the electrons in order to simulate the equilibrium conditions expected in X-ray binaries and AGN, with an example of the source of this heating being magnetic reconnection events in the corona.

It is not, however, possible to heat the electrons in HEART. The only way of increasing the energy in the electron distribution is by adding more high-energy electrons. This does not conserve electron number, but rather continuously increases the electron number. The corona becomes increasingly optically thick with the cooled electrons dominating more with every timestep. It is possible to remove electrons to obtain an equilibrium situation, as is done in chapter 5, but this is an ad hoc solution to the problem required by the particular treatment of electrons implemented in HEART. The addition and removal of electrons in this way is unlikely to represent a physical system. Also, the electron injection and escape are forced to maintain a given electron distribution, causing a similar situation to the case above, where the electron distribution does not evolve. All energy lost by the electrons is assumed replenished by an infinite energy reservoir, and energy is lost as the energy of the removed electrons is also removed, so energy balance is not modelled on any level.

It is possible that energy balance could be modelled by limiting the energy injected into the electron distribution, i.e. limiting the energy reservoir in some way, and keeping track of the energy lost by removed electrons. It may then be necessary to redistribute the energy of the electron distribution in each timestep. This would, however, be an unphysical method which might be able to reproduce physical spectra. If adding reprocessing to HEART were to be attempted, it would be better to restructure HEART to allow for the heating of electrons and to include a control of the amount of power dissipated in the system and where that power is dissipated. Checks should also be put in place in the code to ensure conservation of energy.

6.1.1 The LHS with reprocessing modelled

The model used to fit Cyg X-1 in the LHS in section 4.3 is unphysical because energy balance and reprocessing are not included. The fits to the data can therefore only be taken as confirmation that HEART can reproduce similar fits to those of *compTT*, when HEART is used only to model Comptonisation of soft seed photons by a set, non-evolving electron distribution in a spherical coronal geometry for low Compton y parameters. The model is not self-consistent, as the electron distribution does not evolve, reprocessing and energy balance are not modelled and reflection is added separately. Instead of being absorbed and heating the disc, the scattered photons which return to the disc are simply lost.

Haardt & Maraschi (1993) present detailed calculations to determine the effect of including energy balance and reprocessing on Comptonised spectra. They only consider a slab geometry and an optically thin corona ($\tau \leq 1$), and their spectra suffer slightly from the use of an exponential cut-off to model the high-energy cut-off in the spectrum and the assumption that the flux incident on the disc is isotropic (Poutanen & Svensson, 1996). Apart from the high-energy cut-off and some difference in the relative strength of the reflected component at high energies, however, the general shape of the spectra agrees well with those of Poutanen & Svensson (1996) where a more accurate treatment is used. Poutanen & Svensson (1996) also treat spherical and cylindrical geometries, but their model is restricted to $\tau \lesssim 0.7$. Stern et al. (1995a) also include energy balance and reprocessing in their model, which is considerably more flexible in the geometries and optical depths it can model.

For the purpose of discussing the effect of including energy balance and reprocessing in HEART the work by Haardt & Maraschi (1993) is most appropriate as these authors include a detailed discussion of the effect of such an inclusion. The results of the three models by Haardt & Maraschi (1993), Poutanen & Svensson (1996) and Stern et al. (1995a) are sufficiently similar that the limitations of the model by Haardt & Maraschi (1993) are not significant for this general discussion. The slab geometry is also sufficiently similar to that used in HEART (the covering

fraction of both is 1) to give a good indication of what HEART would model if energy balance and reprocessing were included. For detailed spectral fitting with energy balance and reprocessing included, however, it would be better to use one of the other two models.

Haardt & Maraschi (1993) find that, in cases where Compton cooling is the dominant cooling process for the electrons[1], and if all the energy is assumed to be dissipated in the corona[2], reprocessing causes the electron temperature to adjust so as to maintain a roughly constant spectral index, $\alpha \sim 1$, and also an almost constant Compton y parameter, independent of the optical depth for $\tau \lesssim 0.5$. The adjustment of the electron temperature naturally implies that the ratio of the luminosity in the soft to hard components of the spectrum does not depend on the total power dissipated in the system, and so the spectral index is independent of the total power dissipated in the corona. This depends only weakly on the soft photon temperature.

As the optical depth increases above 0.5, Haardt & Maraschi (1993) find a sudden decrease in the Compton amplification factor and thus an increase in the spectral index, α, making the spectrum steeper. They also find that the spectral index remains within the range $0.4 \lesssim \alpha \lesssim 1.1$ for reasonable parameter values. Stern et al. (1995a) include a simulation of a hemispherical pair corona of optical depth 2 which reaches equilibrium at a coronal temperature increasing from 31 keV (at the bottom) to 72 keV (at the top), with energy balance and reprocessing included. This simulation models very similar conditions to the HEART model in section 4.3, i.e. a hemispherical corona with electrons of temperature 50 keV and optical depth $\tau = 2.2$. With energy balance included, however, Stern et al. (1995a) obtain a spectral index of 1.09, and this spectrum is shown as the dotted line in figure 6.1. Thus the spectral index found by both Haardt & Maraschi (1993) and Stern et al. (1995a) is significantly steeper than that modelled by HEART in the LHS in section 4.3, and in this geometry, harder spectra ($\alpha < 1$) are only produced by lower optical depths

[1]This imposes a lower limit on the electron density to prevent bremsstrahlung from dominating over Compton cooling. See equation (1) of Haardt & Maraschi (1993).

[2]If some power is assumed to be dissipated in the disc, the spectral index is steeper.

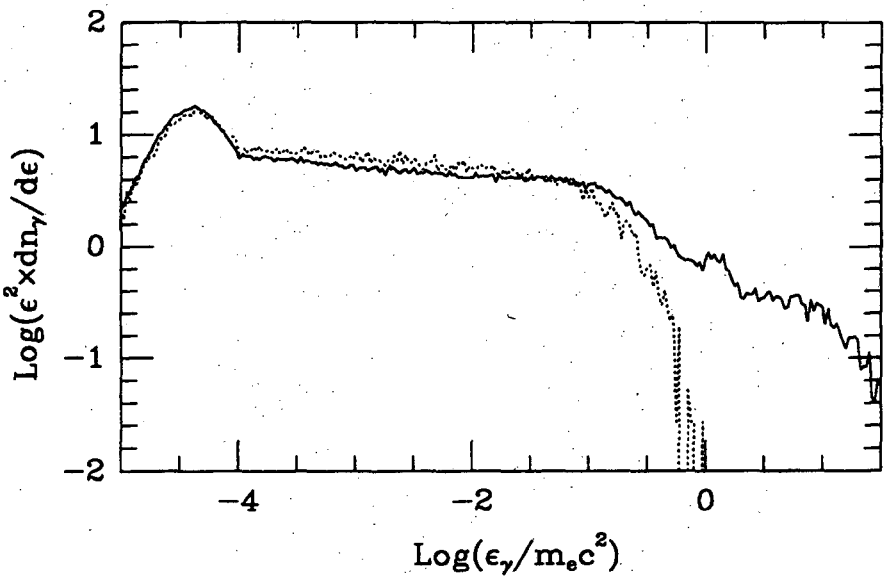

Figure 6.1: A spectrum obtained by Stern et al. (1995a) using similar parameters to those used in HEART to model the LHS in section 4.3, but with reprocessing included. The dotted line assumes a thermal electron distribution in the corona, similarly to that modelled in HEART, while the solid line is for combined thermal and non-thermal power supplies to the corona. Both spectra represent the angular range $\cos\Theta > 0.5$, where Θ is measured from the normal to the disc. The figure is taken from Stern et al. (1995a).

($\tau < 1$). With energy balance and reprocessing included, the HEART spectrum used to fit the LHS cannot be produced using this geometry.

Thus, if reprocessing were 'switched on' in the steady-state HEART model used to fit the LHS data of Cyg X-1, then, rather than photons absorbed by the disc being lost, they would be reprocessed into soft seed flux, increasing the soft seed flux. Keeping the heating of the electrons constant would then cause an overall cooling of the electrons and a steeper spectrum. The steady-state spectrum will be as described by Haardt & Maraschi (1993), Stern et al. (1995a) and Poutanen & Svensson (1996), and not as modelled by HEART in section 4.3.

6.1.2 The X-ray burst in Aql X-1 with reprocessing modelled

The X-ray burst in Aql X-1 occurs towards the start of a state transition, so slower underlying changes are occurring in the system. These take place over a longer timescale than considered here, so they are ignored for the purpose of this discussion. The spectrum of Aql X-1 before the burst can be approximated by an equilibrium situation such as those discussed in Haardt & Maraschi (1993). By the same arguments as in section 6.1.1, the spectrum will be steeper than that modelled by HEART for the same optical depth, if reprocessing and energy balance are included. Deducing the spectrum during the burst is less straightforward, however, as it is not an equilibrium situation where all the power is dissipated in the corona.

Considering the seed photons to be an external addition to the equilibrium situation before the burst, the extra seed photons will initially create more hard X-rays in the corona as they tap the energy of the electrons. The electrons will not be reheated to their original temperature, however, because this temperature cannot be maintained with the increased cooling by the additional seed photons, assuming a constant amount of heating to the electrons (which is not affected by the burst). Thus a lower temperature will be reached in the corona, with the Thomson optical depth remaining unchanged, and therefore the spectrum will be steeper than before the burst occurred. The increased energy in these additional seed photons will also

cause the luminosity to increase.

Alternatively, the extra seed photons can be seen as additional energy dissipation, but occurring in the disc, not the corona. In this case, three effects need to be considered to find the equilibrium spectrum during the burst: the overall power dissipated in the system increases, the temperature of the seed photons increases and some of the power is dissipated in the disc. Increasing the power of the system does not affect the spectral index. Instead, a similar equilibrium is reached at a higher bolometric luminosity. More energy dissipation in the corona causes more efficient re-heating of the electrons, hence more hard X-rays are continually produced, and more reprocessing occurs. This heats the disc so that the same ratio of soft to hard luminosity is maintained at a higher bolometric luminosity.

Spectra are only weakly dependent on the temperature of the soft seed photons, so the increase in seed photon temperature during the burst should only have a small effect on the spectrum. Haardt & Maraschi (1993) find that higher blackbody temperatures create slightly flatter spectra (in the energy range 2-20 keV) due to the hotter corona, assuming that optical depth remains constant. There is also an increased contribution from the reflected spectrum as the increased effect of the anisotropy of Compton scattering at higher energies causes more photons to return to the disc.

So the increased power dissipation, and the increased seed photon temperature cause little change in the spectral index. One consideration remains: some of the energy is dissipated in the disc. Such systems are not as well studied, but allowing some of the energy to be dissipated in the disc causes the spectrum to steepen (Haardt & Maraschi, 1993). Thus overall, a steeper spectrum is expected during the burst.

Both these arguments lead to a steeper spectrum during the burst, as is observed in Maccarone & Coppi (2003), where the soft luminosity increases during the burst while the hard luminosity decreases. Therefore, if reprocessing and energy balance were included in HEART, and electron heating were treated properly, modelling the

Process	Testing	Limitations
Compton scattering	comparison to *compTT*	Compton y parameter $\lesssim 3$
bremsstrahlung	qualitative	electron-electron only
synchrotron	qualitative	
Coulomb interactions	qualitative	only between electrons
kinetic equation	qualitative	no energy balance and no electron heating
reprocessing	not implemented	no energy balance
pair production	not implemented	
pair balance	not implemented	
annihilation	not implemented	
electron transport	not implemented	

Table 6.1: A summary of the limitations of, and testing done on each physical process in HEART. Qualitative testing refers to the qualitative checks done in Collins (2004). All the physical processes are also subject to the general limitations summarised in the text.

'switching on' of the burst should have been more successful, without the necessity of forcing changes in the electron parameters. Different values for the electron parameters would also have been found, given that the geometry modelled is compatible with the system (unlike in the LHS above).

6.2 Technical limitations to HEART

Many limitations to HEART have been presented throughout this thesis, but a few still remain that should be mentioned. This is summarised in table 6.1. Firstly, the physical processes presented in chapter 2 have not all been thoroughly tested. Simple tests are done for all the radiative processes in Collins (2004) to demonstrate that the HEART output seems reasonable and qualitatively reproduces the expected effects of, for example, increasing the temperature and/or density of the electron distribution. Only Compton scattering has been quantitatively compared to any other models, however, and it has only been compared to the analytic model by Titarchuk (1994) in section 4.2. Before trusting the implementations described in chapter 2 they should all be tested more thoroughly, for example by comparing the HEART output to Monte Carlo simulations and/or other well-tested models.

Some of the radiative processes are not implemented with all physical situations taken into account. For example, there is no treatment of any particle other than electrons. This means that pair production, pair balance and annihilation are not modelled, and only electron-electron bremsstrahlung is treated. While an ion accelerated in an electric field emits negligible amounts of energy compared to an electron, electron-ion bremsstrahlung is significant. Ion synchrotron radiation is, however, negligible compared to electron synchrotron radiation, as the power emitted is proportional to m^{-2}, where m is the mass of the particle.

All these processes are important in modelling accretion onto compact objects, the main application of a code such as HEART. Compton scattering and synchrotron radiation may either, or both, be the main mechanism for producing hard X-rays. Bremsstrahlung and Coulomb interactions will occur in these systems, though their effects may be negligible. Coulomb interactions are important at high electron densities where electrons thermalise on shorter timescales than they cool. In other words, Coulomb interactions are important when $l_e/l_s \gg 1$, $l_s \leq 1$ where l_s is the soft photon compactness and l_e the electron compactness (Coppi, 1992). Bremsstrahlung is negligible under more conditions, but it also important at high electron densities (see equation (1) of Haardt & Maraschi (1993)), or if $\tau \gtrsim 1$ and $\Theta \gtrsim 1$ where $\Theta = kT_e/m_ec^2$ (Skibo & Dermer, 1995). The presence of positrons is also expected, for example from photon-photon pair production, and although annihilation lines have not been detected in most X-ray binaries[3], possible smearing of such lines may have effects at lower energies. Electron transport is also important, as evaporation from the disc, disc winds and other bulk motion of the electrons is likely to be occurring and have an important effect on the spectrum. It may even be necessary to reproduce observed spectra (Beloborodov, 1999). Most importantly, electron cooling and heating, energy balance and reprocessing occur naturally in the geometries modelled for these systems and cannot be neglected in a physical model. Their inclusion has a significant effect on the spectra, as discussed in section 6.1,

[3]High energy data from Nova Muscae 1991 has been interpreted as showing annihilation lines. See for example Sunyaev et al. (1992), Gilfanov et al. (1994) and Smith et al. (1995).

and may even hold the key to understanding the geometry of these systems.

Modifications to the code to include positrons and ions are possible, but thorough testing of what is already implemented should be prioritised. More importantly, including energy balance, reprocessing, controlled energy dissipation, electron heating and bulk motion of the electrons would require a complete restructuring of the code to be implemented properly.

HEART is also limited in the geometries it can model. Although almost any geometry of the corona can be approximated using cubic cells, the restriction of only modelling the six directions parallel to the sides of a cube significantly limits the applicability of HEART. Two examples of geometries that HEART cannot model are illustrated in figure 6.2. It is impossible to model reprocessing in any uncovered part of the disc in HEART, because photons cannot return to an uncovered part of the disc. Thus only a covering fraction of 1 can be modelled properly, because a covering fraction of less than 1 will underestimate the reflected component by not modelling the reflected photons which escape without a chance of scattering[4].

A summary of the limitations of HEART is given here.

- The optical depth per cell must be $\ll 1$. This is to ensure the validity of equation 2.30 and because the code can only model a maximum of one scattering per cell.

- A diameter of $\gtrsim 24$ cells is required for sufficiently accurate discretisation of the disc emission, and a diameter of $\lesssim 24$ cells is required to prevent runtimes from exceeding a few hours.

- Compton scattering is only valid for $y_{NR} \lesssim 3$, possibly due to the combined effect of the two previous items. High optical depths cannot be modelled with a diameter of $\lesssim 24$ cells because the optical depth per cell is too high.

[4]An attempt at modelling a spherical corona near the black hole with a disc surrounding it is done in Collins (2004), and is called the ICorona model. Photons are injected sideways into the corona instead of upwards, but only the six directions of the ECorona geometry are modelled. This suffers from the same problems as illustrated here, i.e. scattered photons cannot return to the disc.

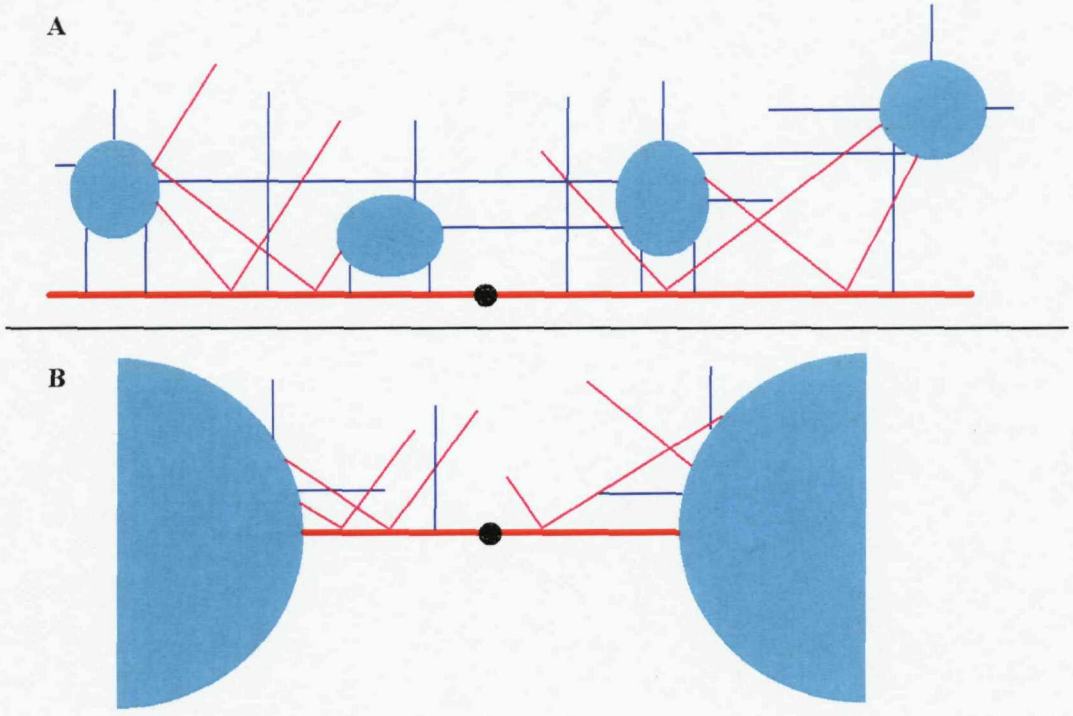

Figure 6.2: These are two examples of coronal geometries which HEART cannot model in a physical way. The red line represents the cross-section of a circular accretion disc with the black dot being the black hole. The cyan regions represent the corona, i.e. volumes with electron populations. Blue lines represent directions which photons in HEART may travel along, and the purple lines represent directions which photons in a real system may travel along, but which are not modelled by HEART.
In example A, disc photons in HEART may either leave the disc directly, or enter a coronal volume. After entering a coronal volume the photons may return to the disc and be reprocessed, but the photons cannot then escape the disc without re-entering a coronal volume. In a real system, however, such photons may leave the system without re-entering a coronal volume, because the photons may travel along diagonals.
In example B, disc photons from HEART cannot enter the corona at all, and even if they could, they can then not return to the disc. Real photons, however, can easily move from the disc to the corona and then return to the disc again.

- A small energy transfer from the electron distribution to the photon distribution, compared to the total energy of the electron distribution, must be ensured in each cell, in each timestep.
- Only a few hundred timesteps can be modelled in a reasonable length of time, i.e. a few hours, and unless very few, large cells can be used this corresponds to physical timescales of less than a second.
- Despite the considerable flexibility of the cell-generating algorithm, many physical geometries cannot be modelled by HEART due to the six direction restriction.
- Energy balance and reprocessing are not modelled. This has a significant effect on the spectrum, as is discussed in section 6.1.
- Particle number is not conserved when modelling electron evolution due to the necessity of adding hot electrons and removing cold electrons to simulate electron heating. If electron addition and removal is not modelled, then the algorithm used to solve the kinetic equation does conserve particle number (Park & Petrosian, 1996).
- The physical processes included have not been thoroughly tested.
- Electrons are the only particle modelled. Thus only electron-electron bremsstrahlung and Coulomb interactions are considered and pair production, pair balance and annihilation are not modelled. Synchrotron radiation from ions is negligible compared to that from electrons.
- The anisotropy of Compton scattering and reflection are not modelled, and spectra from different viewing angles cannot be calculated.
- Electron transport between cells is not modelled.

6.2.1 Comparison to other codes

A short review of other Comptonisation codes is given in section 1.5, and a short discussion of HEART in this context is given here. The codes can be divided into two classes: the analytic codes and the numerical codes. Analytic codes include those by Sunyaev & Titarchuk (1980); Titarchuk (1994); Hua & Titarchuk (1995); Zdziarski (1985); Poutanen & Svensson (1996) and Coppi (1992), whereas numerical codes include the Monte Carlo (MC) code by Skibo & Dermer (1995) and the large particle Monte Carlo (LPMC) code by Stern et al. (1995a). Pozdnyakov et al. (1983) and Haardt & Maraschi (1991) combine the two.

In general, analytic models run much faster than MC codes, but are also less accurate and model more limited systems. The analytic models use escape probabilities rather than modelling the photon propagation, and models are generally limited to simple geometries such as static, homogeneous slab, hemispherical and cylindrical geometries. Within these limitations, however, they agree well with MC codes (Skibo & Dermer, 1995). Thus the analytic models can give a good indication of the general spectral features expected from Compton scattering, but cannot accurately model more complicated systems such as inhomogeneous, dynamic systems.

MC codes take considerably longer to run, with the LPMC code taking over an hour to run on a SPARC 20[5], but they allow for much more flexible and physical modelling. MC codes are also very accurate given that a sufficient number of particles is modelled, and are often used as tests to determine the accuracy of other models. The LPMC by Stern et al. (1995a) is capable of inhomogeneous, dynamic modelling, but does, as always, have other limitations. It does not obtain as good particle statistics in low-density volumes and in the low luminosity parts of the spectrum as other MC codes, and cannot model synchrotron self-absorption properly without modifications (Stern et al., 1995a).

HEART cannot currently compete with the analytic models or the MC codes.

[5]This timing specification was given in 1996. On current computers, this would be considerably faster, but later applications of the LPMC code have been extended and combined with other codes, slowing the run-time down.

Although HEART can achieve as accurate spectra as *compTT* in a restricted parameter space, it can never compete with an analytic model in situations which can be modelled analytically. An analytic model will always be much faster, and probably at least as accurate (*compTT* is accurate over a larger parameter space than HEART). HEART, and any other numerical code, must achieve more than an analytic model in order for the longer run-times to be justified.

In its current form, HEART cannot compete with MC codes, either. The LPMC code of Stern et al. (1995a) is accurate over a greater parameter range, and achieves much of what HEART was intended to achieve, i.e. self-consistent, complete, inhomogeneous, dynamic modelling. It is considered to be computer intensive, but runs considerably quicker than HEART. It is, however, not used for more than approximately 7 different regions to model inhomogeneous systems because of run-time restrictions. A modified HEART would have to do at least as well, as quickly, to be worth considering, and to achieve this will require modifications taking HEART beyond recognition.

It is possible that a cell-based code such as HEART can compete with standard MC codes as far as run-time is concerned, especially in a strongly inhomogeneous system, as the run-time of HEART does not increase when different electron distributions are modelled in each cell. Finding a situation which does not suffer significantly from the other limitations of HEART is, however, unlikely. Again, modifications taking HEART beyond recognition are necessary.

Chapter 7

Conclusion

A detailed overview of HEART, as created by Collins (2004), is given in chapter 2, with details of the equations used for both the radiative transfer and electron evolution and the running of the code. An investigation into the capabilities and validity of HEART is then discussed, making up the majority of this thesis. HEART is tested for a simple case (in chapter 4), where only Compton scattering is calculated and the evolution of the electron distribution is disabled. Some of my additions to the code, detailed in chapter 3, are used in this testing process. For example, full reflection is used to approximate the geometry of a spherical corona with central injection used in the model by Titarchuk (1994), to enable the comparison between output spectra from the two models. In this comparison, the models are found to agree only at low Compton y parameters, $y_{NR} \lesssim 3$. Agreement is poor for high optical depth and/or high electron temperatures. One possible reasons for this is that the optical depth must be much less than 1 in each cell for equation 2.30 to be valid (the equation describing radiative transfer due to Compton scattering). A cell diameter of 24 is therefore not sufficient to model high coronal optical depths, but increasing the number of cells sufficiently is prohibitively time-consuming. Another possible reason is the very simple determination of photon directions after Compton scattering events, in which scattered photons are distributed evenly into the six modelled directions.

It is therefore possible that the valid parameter range of HEART may be increased by including an anisotropic treatment of Compton scattering. It is not possible to calculate the energy from which a photon is scattered in HEART, however, due to the method used for calculating Compton scattering. As the photon direction after scattering depends on its energy prior to the scattering event, it is therefore difficult to include an anisotropic treatment of Compton scattering within the current framework of HEART. The cubic cell structure may also limit the success of such a treatment. Thus it is useful to gauge how significant the inclusion of an anisotropic treatment of Compton scattering is likely to be, before attempting to re-write the Compton scattering code. An improved, yet still simple, approximation is therefore implemented, detailed in section 3.5, and is shown to make a significant difference to the output spectrum.

With this new approximation, agreement is found between HEART and the model by Titarchuk (1994) at high Compton y parameters, though the isotropic approximation is better for low Compton y parameters. Thus an improved treatment of the anisotropy of Compton scattering is likely to make a significant difference to the output spectra, but how accurately this can be done within the current cell structure remains uncertain. It may be more important to enable the modelling of more cells to ensure that the optical depth per cell is much less than 1.

For the purpose of testing HEART further, within the low Compton y parameter restriction, HEART is used to fit data from Cyg X-1 in both the HSS and the LHS (in chapter 4). The same geometry and physical processes are modelled as those tested by comparing HEART spectra to the model by Titarchuk (1994) (as discussed above), though reflection from the disc is also included in the HSS. Reasonable fits to the observational data are obtained with this simple version of HEART. No attempt is made to improve upon these fits by including more of the features of HEART, as these features have not been tested, and including reprocessing and energy balance will have a more significant effect as discussed in section 6.1. The fits are, however, sufficient for the purpose of testing this simple form of HEART, and it is found that

HEART is required to run for roughly a few hundred timesteps, depending on the optical depth of the corona, to produce accurate spectra (as discussed in section 4.1). HEART is thus extremely computer intensive, and, even within the parameter range in which HEART agrees with Titarchuk (1994), HEART is therefore not suitable for routine spectral fitting (as is discussed in section 4.4).

Instead of attempting to improve on the restrictions to spectral fitting at this stage, the focus is moved to modelling dynamic systems, a possible strength of HEART where detailed spectral fitting is less important. HEART, as opposed to most other models, is designed to simultaneously model the evolution of the electron and photon distributions, without the dependence on escape probabilities for the electrons. A better understanding of the capability of HEART for dynamic modelling is required to evaluate whether improving the spectral fitting of HEART is likely to be worthwhile. Dynamic modelling must, however, be used within the restrictions presented so far; only certain parameter ranges can be modelled and any necessary spectral fitting is computer intensive.

For the purpose of investigating the capabilities of HEART for dynamic modelling, further additions to the code are presented in chapter 5, some of which build on modifications discussed in chapter 3. These additions enable the physical parameters of the photon and electron distributions to be varied during a simulation, and output such as lightcurves and hardness-intensity diagrams to be produced. These new features are used to model a state transition from a typical HSS to a typical LHS in a BHXB system, as well as an X-ray burst in the neutron star binary Aql X-1. A lightcurve of short-term variability is also produced in section 3.3.2, where an inhomogeneous corona of changing active regions is modelled.

HEART successfully models the evolution from one set of parameters, usually representing some steady state, to another set of parameters. Every spectrum during the evolution can be studied and lightcurves and hardness-intensity diagrams are compared to observed data. As well as modelling the evolution between two parameter sets, it is also possible to change given parameters and study the effect

such a change has on the spectrum over time.

The limitations of the spectral fitting in HEART also significantly restrict the usefulness of HEART for dynamic modelling, however. A more comprehensive discussion of the limitations of HEART is given in chapter 6. Even in the simple case where electrons do not evolve, the parameter range over which HEART can be applied is limited. Spectra from different viewing angles cannot be modelled, yet observed spectra can change significantly at different viewing angles, and these spectra are greatly affected by the geometry of the source. HEART is also significantly limited in the geometries it can model, as is discussed in section 6.2. Improving the angular treatment of Compton scattering within the current cell structure may improve the valid parameter range, but in order to model different viewing angles and more physical geometries a more drastic modification is required. Two suggestions, discussed in section 3.5, include a cell structure made up of tessellating cells with more sides, or storing a distribution of directions with the photon distributions. Both of these modifications are also approximations, and require yet more computational resources, and yet HEART is already very computer intensive. It can only reasonably be run for a few hundred timesteps, with 600 timesteps modelling of order 0.24 seconds in the source and taking roughly 12 hours to run, so the physical timescales HEART can model are also limited (as discussed in section 5.4).

One possible way of speeding up HEART might be to parallelise the code. This should be possible, as the calculations done in each cell could be done on different processors. With several runs being required for any form of spectral fitting, however, speeding up the run-time of a single run on several computers is not necessarily an advantage over running a slower version of HEART with different parameters sets simultaneously on several computers. The overall required computing time would have to be reduced. Alternatively, computers will almost certainly be significantly faster in future, possibly enabling HEART to run on reasonable timescales even for routine spectral fitting.

More importantly, however, energy balance and reprocessing are not included

in HEART. This significantly changes the spectra, as is discussed in section 6.1. The inclusion of energy balance and reprocessing in HEART requires a complete restructuring of the code, where the total amount of energy injected into the system is controlled, and where electrons are heated rather than being injected and then escaping. Currently, the heating of the electron distribution is modelled in an unphysical way, where high energy electrons are added and colder electrons are removed, rather than heating a constant electron population, and an infinite energy reservoir is assumed. Thus electron evolution is not modelled in a physical way either.

If all the processes implemented in HEART are to be used, further testing is also required. Only a simple case, where Compton scattering is the only physical process modelled in a spherical geometry, is tested here. The other modelled physical processes must be similarly tested before being used.

A code which models spectra simultaneously with the variability of a system is an important tool in furthering our understanding of X-ray binaries and AGN. HEART in its current form is not, however, the answer. The limitations outlined above and in chapter 6 are too large to be overcome without restructuring HEART into a completely different code. The large particle Monte Carlo (LPMC) code by Stern et al. (1995a) is currently a good, available code. Fast, analytic Comptonisation codes dealing with simple Comptonisation problems have been around for a long time now, and have established multiple Compton scattering events as a likely cause of X-ray spectra from X-ray binaries and AGN, and have given a general idea of the optical depth and coronal temperatures required. To progress in Comptonisation models, more detail is required, including the effects of different geometries, bulk motion of the corona, different viewing angles, the structure of the disc and the variability signature. Reprocessing and energy balance must also be included. The LPMC code has so far provided a basis for further developments in this direction, as, for example, in Malzac et al. (2005) where it is combined with another code which models the structure of the disc. Such models, as well as fast analytic calculations to

guide the way, combined with improved observational data, should lead to a better understanding of X-ray binaries and AGN in future.

Appendix A

Appendix

A.1 Coulomb interactions

For Coulomb interactions the treatment of Nayakshin & Melia (1998) is used, and

$$a(\gamma) = \frac{3\sigma_T c \ln\Lambda}{4p\gamma} \int \frac{n'_\gamma}{p'\gamma'}(\gamma - \gamma')\chi(\gamma,\gamma')\mathrm{d}\gamma' \tag{A.1}$$

where $\ln\Lambda$ is the Coulomb logarithm. This is a weak function of energy and therefore a constant value of 20 is assumed. We also set

$$\begin{aligned}\chi(\gamma,\gamma') &= \int_{\gamma^-}^{\gamma^+} \frac{x^2}{\sqrt{(x+1)(x-1)^3}}\mathrm{d}x \times \\ &\left[\sqrt{x^2-1} - \sqrt{\frac{x+1}{x-1}} + 2\ln\left(\sqrt{\frac{x-1}{2}} + \sqrt{\frac{x+1}{2}}\right)\right]_{\gamma^-}^{\gamma^+}\end{aligned} \tag{A.2}$$

where $\gamma^\pm = \gamma\gamma'(1 \pm \beta\beta')$.

For the dispersion we use the corrected version given by Blasi (2000),

$$D(\gamma) = \frac{3\sigma_T c \ln\Lambda}{4p\gamma} \int \frac{n'_\gamma}{p'\gamma'}\left[\zeta(\gamma,\gamma') - \frac{1}{2}(\gamma-\gamma')^2\chi(\gamma,\gamma')\right]\mathrm{d}\gamma' \tag{A.3}$$

where,

$$\begin{aligned}\zeta(\gamma,\gamma') &= \int_{\gamma^-}^{\gamma^+} \frac{x^2}{\sqrt{x^2-1}}\left[\frac{(\gamma+\gamma')^2}{2(1+x)}-1\right]\mathrm{d}x \\ &= \frac{1}{2}\left[\frac{(\gamma+\gamma')^2\sqrt{x^2-1}}{(1+x)\sqrt{(1+x)^2-2x-2}}+(\gamma+\gamma')^2\sqrt{x^2-1}-\right. \\ &\left. x\sqrt{x^2-1}-[1+(\gamma+\gamma')^2]\ln\left(x+\sqrt{x^2-1}\right)\right]_{\gamma^-}^{\gamma^+}. \end{aligned} \tag{A.4}$$

A.2 Compton Scattering

The photon redistribution functions for the three cases defined in section 2.2.3.3 are detailed below.

The solution for case 1 is taken from Coppi & Blanford (1990) and treats the case of mildly relativistic electrons ($\gamma < 10$) interacting with high-energy photons ($k > 10^{-2}$),

$$xF_C(x) = 3\sigma_T x^2 \int \frac{\mathrm{d}P}{\mathrm{d}z}\mathrm{d}z \tag{A.5}$$

where $\frac{\mathrm{d}P}{\mathrm{d}z}$ is given by:

$$\begin{aligned}\frac{\mathrm{d}P}{\mathrm{d}x} = \frac{1}{(1-\beta z)\sqrt{\beta^2+\epsilon^2+2\beta\epsilon z}} \times \left\{2y_0k-ak^2+\frac{1+y_0^2-2ay_0k+a^2k^2}{\sqrt{a^2-b^2}}+\right. \\ \left.\frac{1}{k^2(1-\beta z)}\left[k^2+\frac{ak^2(2b-a)}{(a-b)\sqrt{a^2-b^2}}+\frac{a(1-y_0)^2+2kb^2(1-y_0)-ba^2k^2}{(a^2-b^2)^{\frac{3}{2}}}\right]\right\}\end{aligned} \tag{A.6}$$

where $\epsilon = h\nu_0/(\gamma m_e c^2)$, $k = \gamma m_e c^2/(h\nu_1)$, $a = 1-\beta z-(1-\gamma_0)/k$, $b = \delta/k$ and

$$y_0 = \frac{(\epsilon+\beta z)(\rho+\epsilon\rho-1+\beta z)}{\rho(\beta^2+\epsilon^2+2\beta\epsilon z)}, \tag{A.7}$$

$$\delta = \frac{\beta\sqrt{(a-z^2)[\rho^2\beta^2+2\rho\epsilon(1-p)(1-\beta z)-(\rho-1+\beta z)^2]}}{\rho(\beta^2+\epsilon^2+2\beta\epsilon z)} \tag{A.8}$$

and $\rho = \nu_1/\nu_0$. ν_0 and ν_1 are the frequency of the photon before and after scattering respectively. The integration limits are

$$z_{\pm} = max[\pm 1, \frac{1-\rho(d \mp \sqrt{d^2 - 1/\gamma^2})}{\beta}], \tag{A.9}$$

where $d = 1 + \epsilon - \epsilon\rho$.

Case 2 uses the treatment of Enßlin & Kaiser (2000) in the situation where mildly relativistic electrons ($\gamma < 10$) interact with low energy photons ($k \leq 10^{-2}$),

$$\begin{aligned} xF_C(x) &= \frac{3\sigma_T}{8p^5}\left\{-\frac{|1-\rho|}{4p}\left[1+\rho(10+8p^2+4p^4)+\rho^2\right]+\right. \\ &\left.\rho(1+\rho)\left[\frac{3+3p^2+p^4}{\gamma} - \frac{3+2p^2}{2p}(2\ln(p+\gamma) - |\ln(\rho)|)\right]\right\} \end{aligned} \tag{A.10}$$

where ρ is as in case 1 and $p = \sqrt{\gamma^2 - 1}$.

Case 3 is for ultra-relativistic electrons ($\gamma \geq 10$) (Jones, 1968),

$$xF_C(x) = 3\sigma_T x\left\{2q\ln(q) + (1-q)\left[(1+2q) + \frac{\left(4\gamma q\frac{h\nu_0}{m_e c^2}\right)^2}{2\left(1+4\gamma q\frac{h\nu_0}{m_e c^2}\right)}\right]\right\} \tag{A.11}$$

where $q = x/\left(1 - \frac{h\nu_1}{\gamma m_e c^2}\right)$, the frequency gain $\rho = \nu_1/\nu_0$ and p is the electron momentum.

A.3 Time estimate

In an optically thin corona, photons leaving through surface cells represent the model output after only a few timesteps. Since most photons traverse the corona without any interaction with the coronal plasma, the model output will not change significantly after R_{cor}/R_{cell} timesteps, where R_{cell} is the size of a single cell and R_{cor} is the diameter of the entire corona.

If the corona is optically thick, significantly more timesteps may be needed before

the model output 'settles down' to a steady state. Consider the case of an optically thick corona in which only inverse Compton scattering off a thermal electron population is important. If the temperature of the electrons is T_e, then the typical maximum energy to which photons can be boosted by Comptonisation is $3kT_e$. The energy gain per scattering event is $\Delta\nu/\nu \approx kT_e/(m_e c^2)$, and so after N scattering events the energy of a photon with initial energy $h\nu_0$ is

$$h\nu \approx \left(1 + \frac{kT_e}{m_e c^2}\right)^N h\nu_0. \tag{A.12}$$

The number of scattering events required for a photon of initial energy $h\nu_0$ to reach energy $h\nu$ is

$$N \approx \frac{\log \frac{h\nu}{h\nu_0}}{\log\left(1 + \frac{kT_e}{m_e c^2}\right)}. \tag{A.13}$$

Scatterings become less efficient at transferring energy to the photon as $h\nu \sim kT_e$, so this is a lower limit for the required number of scattering events.

After N scattering events a photon with the maximum energy must escape from the corona to be observable. For a spherical corona of radius R_{cor} and total optical depth τ we can write $N = (\tau/R_{cor})ct$, where t is the escape time for the photons with the maximum energy. In HEART there are $N_c = R_{cor}/R_{cell}$ cells along the radius of the corona. During a single timestep a photon travels through one cell, i.e. $\Delta t = R_{cell}/c = R_{cor}/N_c c$. So, for the photons with the maximum energy to escape from the corona after N scattering events, we require $t/\Delta t = N_c N/\tau$ timesteps. This provides us with a rough estimate for the minimum number of timesteps we need to model in HEART before we can expect to observe photons with the maximum energy attainable to escape the corona. Note here that this estimate only applies for situations where we want to model a static disc/corona system with a steady-state spectrum. HEART is designed to simulate evolving situations and for these the calculation of a minimum number of timesteps to reach a steady state is irrelevant.

Bibliography

Beloborodov A. M., 1999, Mon. Not. R. Astron. Soc., 305, 181

Blasi P., 2000, The Astrophysical Journal, 535, L9

Blumenthal G. R., Gould R. J., 1970, Reviews of modern Physics, 42, 237

Chang J. S., Cooper G., 1970, Journal of Computational Physics, 6, 1

Collins R. S., 2004, PhD thesis, School of Engineering Sciences, Faculty of Engineering, University of Southampton

Coppi P. S., 1992, Mon. Not. R. Astron. Soc., 258, 657

Coppi P. S., Blanford R. D., 1990, Mon. Not. R. Astron. Soc., 245, 453

DiSalvo T., Done C., Życki P. T., Burderi L., Robba N. R., 2001, Mon. Not. R. Astron. Soc., 547, 1024

Done C., Gierliński M., 2003, Mon. Not. R. Astron. Soc., 342, 1041

Done C., Gierliński M., 2005, Astrophysics and Space Science, 300, 167

Done C., Gierliński M., Kubota A., 2007, The Astronomy and Astrophysics Review, 15, 1

Done C., Nayakshin S., 2001, Mon. Not. R. Astron. Soc., 328, 616

Done C., Nayakshin S., 2005, Astrophysics and Space Science, 300, 167

Enßlin T. A., Kaiser C. R., 2000, Astron. & Astrophys., 360, 417

Esin A. A., McClintock J. E., Narayan R., 1997, The Astrophysical Journal, 489, 865

Esin A. A., Narayan R., Cui W., Grove J. E., Zhang S., 1997, The Astrophysical Journal, 489, 865

Falcke H., Körding E., Markoff S., 2004, Astron. & Astrophys., 414, 895

Fender R. P., 2001, Mon. Not. R. Astron. Soc., 322, 31

Fender R. P., Belloni T. M., Gallo E., 2004, Mon. Not. R. Astron. Soc., 355, 1105

Fender R. P., Corbel S., Tzioumis T., McIntyre V., Campbell-Wilson D., Nowak M., Sood R., Hunstead R., Harmon A., Durouchoux P., Heindl W., 1999, The Astrophysical Journal, 519, L165

Frank J., King A. R., Raine D. J., 1992, Accretion Power in Astrophysics, 2nd edn. Cambridge University Press

Frontera R., Palazzi E., Zdziarski A. A., Haardt F., Perola G. C., Chiappetti L., Cusumano G., Fiume D. D., Sordo S. D., Orlandini M., Parmar A. N., Piro L., Santangelo A., Segreto A., Treves A., Trifoglio M., 2001, The Astrophysical Journal, 546, 1027

George I. M., Fabian A. C., 1991, Mon. Not. R. Astron. Soc., 249, 352

Ghisellini G., Guilbert P. W., Svensson R., 1988, The Astrophysical Journal, 334, 5

Gilfanov M., Churazov E., Sunyaev R., Khavenson N., Novikov B., Dyachkov A., Tserenin I., Sukhanov K., Denis L. B. M., Schmitz-Fraysse M. C., Mandrou P., Paul J., Cordier B., Goldwurm A., Lebrun F., 1994, Astrophysical Journal Supplement Series, 92, 411

Gould R. J., 1980, The Astrophysical Journal, 238, 1026

Guilbert P. W., Rees M. J., 1988, Mon. Not. R. Astron. Soc., 233, 475

Haardt F., 1993, The Astrophysical Journal, 413, 680

Haardt F., Maraschi L., 1991, The Astrophysical Journal, 380, L51

Haardt F., Maraschi L., 1993, The Astrophysical Journal, 413, 507

Haardt F., Matt G., 1993, Mon. Not. R. Astron. Soc., 261, 346

Herrero A., Kudritzki R. P., Gabler R., Vilchez J. M., A G., 1995, Astron. & Astrophys., 297, 556

Ho L. C., 2005, Astrophysics and Space Science, 300, 219

Hua X.-M., Titarchuk L. G., 1995, The Astrophysical Journal, 449, 188

Jester S., Körding E., Fender R., 2006, Proceedings of the VI Microquasar Workshop: Microquasars and Beyond. September 18-22, 2006, Como, Italy., p.26.1

Jones F. C., 1968, Phys. Rev., 167, 1159

Körding E., Jester S., Fender R., 2006, Mon. Not. R. Astron. Soc., 372, 1366

Lei F., Dean A. J., Hills G. L., 1997, Space Science Reviews, 82, 309

Lewin W. H. G., van Paradijs J., Taam R. E., 1993, Space Science Reviews, 62, 223

Lightman A. P., White T. R., 1988, The Astrophysical Journal, 335, 57

Longair M. S., 2004, High Energy Astrophysics Volume 1: Particles, Photons and Their Detection, 2nd edn. Cambridge University Press

Maccarone T. J., 2003, Astron. & Astrophys., 409, 697

Maccarone T. J., Coppi P. S., 2003, Astron. & Astrophys., 399, 1151

Maccarone T. J., Gallo E., Fender R., 2003, Mon. Not. R. Astron. Soc., 345, L19

McClintock J. E., Remillard R. A., 2004, Compact Stellar X-ray Sources. Cambridge University Press

McHardy I. M., Körding E., Knigge C., Uttley P., Fender R. P., 2006, Nature, 444, 730

Magdziarz P., Zdziarski A. A., 1995, Mon. Not. R. Astron. Soc., 273, 837

Malzac J., Beloborodov A. M., Poutanen J., 2001, Mon. Not. R. Astron. Soc., 326, 417

Malzac J., Dumont A. M., Mouchet M., 2005, Astron. & Astrophys., 430, 761

Malzac J., Jourdain E., 2005, Astron. & Astrophys., 359, 843

Markoff S., Falcke H., Fender R., 2001, Astron. & Astrophys., 372, 25

Matt G., Perola G. C., Piro L., 1991, Astron. & Astrophys., 247, 25

Merloni A., Heinz S., Matteo T. D., 2003, Mon. Not. R. Astron. Soc., 345, 1057

Merloni A., Malzac J., Fabian A. C., Ross R. R., 2006, Mon. Not. R. Astron. Soc., 370, 1699

Morrison R., McCammon D., 1983, The Astrophysical Journal, 270, 119

Narayan R., McClintock J. E., Yi I., 1996, The Astrophysical Journal, 457, 821

Narayan R., Yi I., 1994, The Astrophysical Journal, 428, L13

Narayan R., Yi I., 1995, The Astrophysical Journal, 444, 231

Narayan R., Yi I., Mahadevan R., 1995, Nature, 374, 623

Nayakshin S., Melia F., 1998, Astrophysical Journal Supplement Series, 114, 269

Park B. T., Petrosian V., 1996, Astrophysical Journal Supplement Series, 103, 255

Petrucci P. O., Merloni A., Fabian A., Haardt F., Gallo E., 2001, Mon. Not. R. Astron. Soc., 328, 501

Pounds K. A., Done C., Osborne J. P., 1995, Mon. Not. R. Astron. Soc., 277, L5

Pounds K. A., Nandra K., Stewart G. C., George I. M., Fabian A. C., 1990, Nature, 344, 132

Poutanen J., Svensson R., 1996, The Astrophysical Journal, 470, 249

Pozdnyakov L. A., Sobol I. M., Sunyaev R. A., 1983, Soviet Scientific Reviews, Astrophysics and Space Physics, ed. R. A. Suntaev, Harwood Academic Publishers: New York, Vol II, 2, 189

Quataert E., Narayan R., 1999, The Astrophysical Journal, 520, 298

Rybicki G. B., Lightman A. P., 1979, Radiative Processes in Astrophysics. Wiley-Interscience

Shakura N. I., Sunyaev R. A., 1973, Astron. & Astrophys., 24, 337

Skibo J. G., Dermer C. D., 1995, The Astrophysical Journal, 446, 86

Smith D. M., Leventhal M., Cavallo R., Gehrels N., Tueller J., Fishman G., 1995, American Astronomical Society, 187, 4601

Stern B. E., Begelman M. C., Sikora M., Svensson R., 1995a, Mon. Not. R. Astron. Soc., 272, 291

Stern B. E., Poutanen J., Svensson R., Sikora M., Begelman M. C., 1995b, The Astrophysical Journal, 449, L13

Sunyaev R., Churazov E., Gilfanov M., Dyachkov A., Khavenson N., Grebenev S., Kremnev R., Sukhanov K., Goldwurm A., Ballet J., Cordier B., Paul J., Denis M., Vedrenne G., Niel M., Jourdain E., 1992, The Astrophysical Journal, 389, L75

Sunyaev R. A., Titarchuk L. G., 1980, Astron. & Astrophys., 86, 121

Sunyaev R. A., Titarchuk L. G., 1985, Astron. & Astrophys., 143, 374

Synge J. L., 1957, The Relativistic Gas. North-Holland, Amsterdam

Titarchuk L. G., 1994, The Astrophysical Journal, 434, 570

van der Klis M., 1994, Astrophysical Journal Supplement Series, 92, 511

van der Klis M., 2004, astro-ph, 0410551

Weisstein E. W., , 2008, "Solid Angle." From MathWorld–A Wolfram Web Resource. http://mathworld.wolfram.com/SolidAngle.html

White T. R., Lightman A. P., Zdziarski A. A., 1988, The Astrophysical Journal, 331, 939

Zdziarski A. A., 1985, The Astrophysical Journal, 289, 514

Zdziarski A. A., 1986, The Astrophysical Journal, 303, 94

Zdziarski A. A., Coppi P. S., Lamb D. Q., 1990, The Astrophysical Journal, 357, 149

Zdziarski A. A., Gierliński M., 2004, Progress of Theoretical Physics, 155, 99